

INSTABILITY AND ENERGETICS

IN A BAROCLINIC OCEAN

by

Kuh Kim

S.B., Seoul National University
(1968)

M.S., Seoul National University
(1970)

SUBMITTED IN PARTIAL FULFILLMENT OF THE
REQUIREMENTS FOR THE DEGREE OF
DOCTOR OF PHILOSOPHY

at the

MASSACHUSETTS INSTITUTE OF TECHNOLOGY

and the

WOODS HOLE OCEANOGRAPHIC INSTITUTION

August, 1975

Signature of Author.....
Joint Program in Oceanography, Massachu-
setts Institute of Technology - Woods Hole
Oceanographic Institution, and Department
of Earth and Planetary Sciences, and
Department of Meteorology, Massachusetts
Institute of Technology, August 1975

Certified by..... Thesis Supervisor

Accepted by.....
Chairman, Joint Oceanography Committee in
the Earth Sciences, Massachusetts Institute
of Technology - Woods Hole Oceanographic
Institution

Lindgren
~~WITHDRAWN~~
FROM 2 1976
MIT LIBRARIES

INSTABILITY AND ENERGETICS
IN A BAROCLINIC OCEAN

by

Kuh Kim

Submitted to the Massachusetts Institute of Technology-Woods Hole Oceanographic Institution Joint Program in Oceanography on August 11, 1975, in partial fulfillment of the requirements for the degree of Doctor of Philosophy.

ABSTRACT

This thesis is made of two separate, but interrelated parts.

In Part I the instability of a baroclinic Rossby wave in a two-layer ocean of inviscid fluid without topography, is investigated and its results are applied in the ocean. The velocity field of the basic state (the wave) is characterized by significant horizontal and vertical shears, non-zonal currents, and unsteadiness due to its westward propagation. This configuration is more relevant to the ocean than are the steady, zonal 'meteorological' flows, which dominate the literature of baroclinic instability. Truncated Fourier series are used in perturbation analyses.

The wave is found to be unstable for a wide range of the wavelength; growing perturbations draw their energy from kinetic or potential energy of the wave depending upon whether the wavelength, $2\pi L$, is much smaller or larger than $2\pi L_\rho$, respectively, where L_ρ is the internal radius of deformation. When the shears are comparable dynamically, $L \sim L_\rho$, the balance between the two energy transfer processes is very sensitive to the ratios L/L_ρ and U/C as well, where U is a typical current speed, and C a typical phase speed of the wave. For $L = L_\rho$ they are augmenting if $U < C$, yet they detract from each other if $U > C$.

The beta-effect tends to stabilize the flow, but perturbations dominated by a zonal velocity can grow irrespective of the beta-effect.

It is necessary that growing perturbations are comprised of both barotropic and baroclinic modes vertically. The scale of the fastest growing perturbation is significantly larger than L for barotropically controlled flows ($L < L_\rho$), reduces to the wave scale L for a mixed kind ($L \sim L_\rho$) and is fixed slightly larger than L_ρ for baroclinically controlled flows ($L > L_\rho$).

Increasing supply of potential energy causes the normalized growth rate, $\alpha L/U$, to increase monotonically as $L \rightarrow L_\rho$ from below. As L increases further beyond L_ρ , the growth rate $\alpha L_\rho/U$ shows a slight increase, but soon approaches an asymptotic value.

In a geophysical eddy field like the ocean this model shows possible pumping of energy into the radius of deformation (~ 40 km rational scale, or 250 km wavelength) from both smaller and larger scales through nonlinear interactions, which occur without interference from the beta-effect. The e-folding time scale is about 24 days if $U = 5$ cm/sec and $L = 90$ km. Also it is strongly suggested that, given the observed distribution of energy versus length scale, eddy-eddy interactions are more vigorous than eddy-mean interaction, away from intense currents like the Gulf Stream. The flux of energy toward the deformation scale, and the interaction of barotropic and baroclinic modes, occur also in fully turbulent 'computer' oceans, and these calculations provide a theoretical basis for source of these experimental cascades.

In Part II an available potential energy (APE) is defined in terms appropriate to a limited area synoptic density map (e.g., the 'MODE-I' data) and then in terms appropriate to time-series of hydrographic station at a single geographic location (e.g., the 'Panulirus' data).

Instantaneously the APE shows highly variable spatial structure, horizontally as well as vertically, but the vertical profile of the average APE from 19 stations resembles the profile of vertical gradient of the reference stratification. The eddy APE takes values very similar to those of the average kinetic energy density at 500 m, 1500 m and 3000 m depth in the MODE area.

In and above the thermocline the APE has roughly the same level in the MODE area (centered at 28°N , $69^\circ 40'\text{W}$) as at the Panulirus station ($32^\circ 10'\text{N}$, $64^\circ 30'\text{W}$), yet in the deep water there is significantly more APE at the Panulirus station. This may in part indicate an island effect near Bermuda.

Thesis Supervisor: Peter B. Rhines
Title: Senior Scientist, Department of Physical Oceanography,
Woods Hole Oceanographic Institution.

ACKNOWLEDGMENTS

The author wishes to express sincere thanks to Dr. Peter Rhines for providing a unique opportunity to work under his supervision. From the initial motivation to the completion of this thesis, Dr. Rhines has been a constant source of encouragement and physical insight. Thanks are also expressed to Professor Jule Charney and Professor John Hart at M.I.T. for the constructive comments which were very important in expanding the scope of the research. Professor Carl Wunsch also at M.I.T. kindly provided the edited Panulirus data. Ms. Elizabeth Schroeder at the Woods Hole Oceanographic Institution made available the current unpublished results of the Panulirus data, which have been a great help. A special word of thanks must be extended to Ms. Audrey Williams and Ms. Doris Haight for their superb help in typing this thesis.

This research has been supported by the National Science Foundation grant IDO 73-09737, formerly GX-36342. The support is gratefully acknowledged.

TABLE OF CONTENTS

	Page
ABSTRACT	2
ACKNOWLEDGMENTS	4
LIST OF FIGURES	7
LIST OF TABLES	13
PART I	14
I. INTRODUCTION	15
II. BASIC FORMULATION	35
II-1 Basic Equations in a Two-layer Ocean . . .	35
II-2 Energy Conservation	43
II-3 Exact Solutions of the Basic Equations and Their Stability	45
III. PERTURBATION EQUATIONS	49
III-1 Linearized Perturbation Equations	49
III-2 Energy Equation for the Perturbation . . .	52
III-3 Integral Properties of Perturbation . . .	54
IV. PERTURBATION ANALYSIS	60
IV-1 Solutions in Fourier Series	60
IV-2 Characteristics in 3-mode Truncation . . .	68
IV-2-1 Marginal Stability Curves	68
IV-2-2 Growth Rate for Unstable Perturbation . .	71
IV-3 Higher-mode Analysis	80
IV-3-1 Analysis with 7 Modes	81
IV-3-2 Baroclinic Interaction vs. Barotropic Interaction	92
V. DISCUSSIONS AND GEOPHYSICAL APPLICATIONS	96
VI. CONCLUSIONS	114
PART II	117
I. INTRODUCTION	118
II. DEFINITION OF AVAILABLE POTENTIAL ENERGY	124

	Page
III. APPLICATION OF THE AVAILABLE POTENTIAL ENERGY .	134
III-1 Available Potential energy in the MODE Area	134
III-1-1 Mean Density Field	136
III-1-2 Eddy Available Potential Energy	139
III-2 Available Potential Energy from the Panulirus Data	149
III-2-1 Anomaly of Potential Energy	150
III-2-2 Eddy Available Potential Energy	156
IV. DISCUSSION AND CONCLUSIONS	164
BIBLIOGRAPHY	169
BIOGRAPHY	175

LIST OF FIGURES

Figure	Page
Part I	
1.1	18
<p>From Crease(1962). Trajectories of five series of floats. Figures at ends of trajectory are starting and finishing dates. Figures beside trajectory are average speeds. Currents are very energetic with an apparent period of 50 to 100 days(Swallow,1971) and an estimated wavelength of 300 to 400 km(Phillips,1966).</p>	
1.2	19
<p>From Schroeder and Stommel(1969). Temperature anomalies at the Panulirus station in 1960. Units: hundreds of a degree centigrade. Vertical scale changes at 200 m. Closed contours in the thermocline show a strong temporal variation. Anomaly of 1°C roughly corresponds to a vertical excursion of 50 m in the thermocline.</p>	
1.3	20
<p>From Wunsch(1972a). Spectrum of temperature near Bermuda near the depth of the main thermocline, plotted so that the area under the curve is proportional to the variance of temperature. Most of the energy lies in periods of 40-200 days, indicating a strong low frequency variation.</p>	
1.4	21
<p>Depth of 10°C isotherm from the data in Fuglister(1960). Sampling is sparse, but the presence of multiple scales is apparent at two separate sections.</p>	
1.5	23
<p>From Katz(1973). Depth of isopycnals, $\sigma_t = 26.91$ for Tow 300 and $\sigma_t = 26.87$ for Tow 400. These profiles confirm the presence of an <u>intermediate</u> scale. The distance between a peak and a valley is 180 km from Tow 400 and 360 km from Tow 300 at least.</p>	
1.6	24
<p>Profile of mean speed and mean velocity plotted from Koshlyakov and Grachov(1973). A large-scale anti-cyclonic eddy was observed during the Polygon experiment and its mean speed is overwhelmingly larger than mean velocity for all depth. The main thermocline is located at about 250 m.</p>	

Figure	Page
1.7	26
<p>From Sanford(1975). Velocity profiles show a strong shear concentrated in the main thermocline, suggesting the dominance of grave baroclinic mode.</p>	
1.8	29
<p>From Veronis and Stommel(1956). The dispersion relations of barotropic and baroclinic Rossby waves in a two-layer ocean. Thicknesses of upper and lower layers are 500 m and 3500 m, respectively. $f=10^{-4} \text{ sec}^{-1}$, $\beta=2 \times 10^{-13} \text{ cm}^{-13} \text{ sec}^{-1}$. The radius of deformation based upon the upper layer thickness is 31 km. Note that the minimum period of the baroclinic Rossby wave is about one year.</p>	
2.1	36
<p>The stratification of the ocean is idealized by two homogeneous layers of densities, ρ_1 and ρ_2, where $\rho_1 < \rho_2$. Thickness of the upper layer is h_1 and h_2 is a height of the interface.</p>	
3.1	50
<p>The velocity structure of the basic wave is characterized by the presence of horizontal shear as well as vertical shear, associated with kinetic and potential energies respectively, which are partitioned by $(L_\rho/L)^2$, where L_ρ is the internal radius of deformation.</p>	
4.1	69
<p>Branch I: The regime above marginal stability curves is unstable and one below the curves is stable. Note short wavelength limit of unstable perturbations in the meridional scale of perturbation(L_p) for large scale basic flow, $L > L_\rho$. There exist unstable modes irrespective of the current strength U. Branch II: The unstable region is both upper and lower bounded in L_p/L_ρ. As in Branch I, unstable perturbation exists for $\frac{U}{C} < 1$.</p>	
4.2a	72
<p>The beta-effect(β) is relatively strong and the baroclinic and barotropic instability regimes are distinct for very large and small value of L/L_ρ, respectively. The restoring effect of β clearly acts to stabilize modes near the center of the figure.</p>	

Figure	Page
4.2b	73
<p>As the basic flow strengthens (or with a weak beta-effect), the baroclinic and barotropic instability regimes merge into a smooth growth-surface. Short wavelength limit in the baroclinic regime is shown clearly,</p>	
4.2c	74
<p>Same as Fig. 4.2b except for a stronger current case. The meridional scale of the fastest growing perturbation is fixed at a scale slightly larger than the radius of deformation in the baroclinic regime and decreases in proportional to the zonal scale of the basic flow in the barotropic regime.</p>	
4.3	76
<p>Growth rate $\alpha L/U$, renormalized for the range $L \leq L_\rho$, where the barotropic interaction is important. The scale at the maximum growth rate is the same as that of the basic flow for $\frac{U}{C} = \infty$ and $\frac{L}{L_\rho} = 1$ and the basic flow generates a larger scale as its scale and strength decrease.</p>	
4.4	77
<p>Recapitulation of Fig. 4.3. Figures beside the curves are values of U/C and L_p/L at the maximum growth rate. Note an increase of the growth rate as $L \rightarrow L_\rho$, which is possible because of an increasing supply of potential energy.</p>	
4.5	82
<p>These curves correspond to vertical cuts in Fig. 4.2b(3-mode). Growth rate shows basically the same behavior as found from the 3-mode analysis; short wavelength limit and maximum growth rate at $L_p \simeq L_\rho$ in baroclinically controlled flows, and generation of larger scale in a barotropically controlled flow.</p>	
4.6	84
<p>For region $L < L_\rho$ this figure is very similar to Fig. 4.4 from the 3-mode analysis, indicating truncation errors are small. For $L > L_\rho$, a slight decrease of normalized growth rate as $L \rightarrow L_\rho$ from above is notable. This may be due to a feedback of energy into the basic wave via the interaction of Reynold stresses with the mean horizontal shear.</p>	

- | Figure | Page |
|---|------|
| <p>4.7 From Simmons(1974). The dependence of maximum growth rate on channel width for a steady, zonal current with profile $u = 1 - 4\delta \left(\frac{y}{y_0} - \frac{1}{2} \right)^2$, where meridional walls are at $y = 0, y_0$. Lower layer is at rest initially and the radius of deformation is 1,225 km. Note a reduction of growth rate due to a non-uniformity ($\delta \neq 0$) compared with the case $\delta = 0$. As the channel becomes narrower (a horizontal shear increases effectively), the growth rate decreases further, meanwhile the horizontal shear is intensified.</p> | 86 |
| <p>4.8a Fast convergence of series for $U < C$ and $L < L_\rho$</p> <p>answers why the results from the 3-mode analysis are so close to those from the 7-mode one. Convergence becomes slower as L increases from L_ρ and U from C. However, a calculation with 9 modes show very little further change in the growth rate.</p> | 88 |
| <p>4.8b A tendency to generate a strong barotropic component of growing perturbation can be more easily seen in Branch II. Odd modes, $n = \pm 1, \pm 3, \dots$, are barotropic vertically.</p> | 89 |
| <p>4.9 Relative perturbation kinetic energy plotted as a scalar wavenumber spectrum. Wavenumber unity corresponds to the deformation radius and the wavenumber of the basic wave is underlined. Irrespective of U/C and L/L_ρ, mode $n = 0$, the lowest wavenumber representing the zonal component of the perturbation, contributes the highest peak. It is interesting to produce a quasi-continuous spectrum from a single mode.</p> | 91 |
| <p>4.10 The balance between the two distinct energy transfer processes is very sensitive to the ratios L/L_ρ and U/C as well. Potential energy of the wave is always available for growing perturbations, yet kinetic energy of the wave is not. Note a feedback of energy toward the wave for a strong current, $\frac{U}{C} = 2.5$.</p> | 94 |

Figure	Page
5.1 Rhines' (1975a) numerical experiment shows that a large-scale baroclinic Rossby wave with $L \cong 4 \times L_{\rho}$ is unstable and 'noise' develops into eddy field. Slow westward propagation of stream lines are visible along left and right edges. At $t = 1.0$ (about 23 days later) organized eddy field can be identifiable and further amplification is very clear at $t = 1.5$.	105
5.2 Perturbation energy grows exponentially as predicted in the theory during the instability shown in Fig. 5.1.	106
5.3 Energy transfer during the instability shown in Fig. 5.1 is dominated by the baroclinic process. Barotropic interaction removes kinetic energy from wavenumber 6, but the net kinetic energy increases via the conversion from the potential energy at the same wavenumber supplied from wavenumber 2 by the instability.	108
5.4 Initially energy spectrum has two peaks, one at $k = 1$ and the other around $k = 6$. Subsequent energy transfers toward higher wavenumbers ($k = 8$ corresponds to the radius of deformation) are concentrated around $k = 6$ with very little change at $k = 1$. This development is consistent with the theoretical prediction.	109
 Part II	
2.1 An available potential energy (APE) is defined as work done by a local mean buoyancy force $\frac{1}{2}g\rho'$ for a displacement of $z - z_p$, where ρ' is approximated by $-\bar{\rho}_z(z-z_p)$. Note that the APE is <u>positive definite</u> . Accordingly each fluid particle has its own reference level in the definition of the APE.	129
3.1a Comparison of 5 <u>Chain</u> station data with 5 <u>Researcher</u> station data on the circle of 200 km in radius in March, 1973. Statistical test shows that the difference in the average potential density is not significant for a 95% confidence interval.	140

Figure	Page
3.1b Same as Fig. 3.1a, except that salinity and temperature are intercompared. The results of statistical tests are the same as that for the potential density.	141
3.2 The APE varies very significantly in space, horizontally as well as vertically.	142
3.3 Profile of an average APE in space from 19 stations shows remarkably simple vertical structure, which resembles the profile of vertical gradient of the reference stratification. This energy level is very similar to the average kinetic energy density at 500 m, 1500 m and 3000 m depth.	144
3.4 Estimates of r.m.s. vertical excursion reveal large vertical movements below the thermocline, suggesting a strong baroclinicity, which seems to contradict the simplified picture sometimes given, that the deep water is dominated by the barotropic mode.	145
3.5a Variation of the APE over a scale of 100 km suggests that an advection of the APE could be very important in a local energetics.	146
3.5b Same as Fig. 3.5a, but in June.	147
3.6 Monthly variation of the mean anomaly of potential energy.	152
3.7 Time-series of fluctuating part(χ') of the anomaly of potential energy. The fluctuations are strongly coupled between the two layers. Over all the lower layer has a smaller amplitude of variation than the upper layer, yet they are of the same order of 10^8 ergs/cm ² .	153
3.8 Monthly variation of the mean potential density minus the average over 7 years.	155
3.9 Time-series of the APE shows again the coupling between the water in and below the thermocline. Note that a typical magnitude of the APE is smaller than that of the fluctuation in Fig. 3.7 by an order of magnitude at least.	158

Figure		Page
3.10	Out of 151 stations the APE is less than the mean for 71% of them and higher for 29%. Irregular burst of high energy contributes the 29%.	162

LIST OF TABLES

Table		Page
Part II		
1	Anomaly of potential energy at Site D.	121
2a	List of CTD and STD stations in March.	137
2b	List of CTD and STD stations in June.	138
3	Comparison of the available potential energy with the kinetic energy in the MODE area.	148

PART I

I. INTRODUCTION

Prior to this decade currents in the ocean interior were modelled as a sum of linear Sverdrup flow (Sverdrup, 1947) and linear waves (Veronis and Stommel, 1956). In regions of intense boundary currents nonlinearity was added later (Charney, 1955), and the instability of these currents was examined numerically (Bryan, 1963). However, discoveries of intense space- and time-dependent mid-ocean 'eddies', begun with the Aries measurements in 1959-60, led to growing uncertainty about the linear dynamics of either the mean circulation or the fluctuations.

Some recent theories emphasize a new physics, in which the eddies rapidly alter their horizontal and vertical structures (in the inertial time-scale of a few weeks to a few months). At the same time vestiges of linear wave theory, persistent westward propagation found in numerical experiments and observations, still apply so that there is a dual nature to such eddies.

To capture some of this dual nature we examine the stability of one of the fundamental linear waves, the baroclinic Rossby wave. Intense instability is found in which 'noise' added to the simple wave grows. The resulting transfer of energy to new scales forms a tractable analog of energy cascades in the turbulent numerical models. (The theory was motivated by an experimental demonstration

of the instability by Rhines (1975a)).

In one extreme (large length scale of the basic wave) the instability feeds upon the potential energy of the wave. Classical calculations of baroclinic instability emphasize steady, zonal flows as basic states, which is appropriate to the atmosphere, whereas here we show the effect of an 'oceanic' basic state that is neither steady nor zonal nor infinite in scale.

In another extreme (small initial length scale) the instability feeds on the kinetic energy of the horizontal shear. This limit gives, as a special case, the purely barotropic instability found by Lorenz (1972) and Gill (1974).

At the important intermediate scale (the internal deformation scale ~ 50 km), the instability is of a mixed kind, the two energy sources sometimes augmenting, sometimes detracting from one another.

The application to the ocean suggests (as do the computer experiments) that a given 'eddy' may receive energy from a variety of scales of other eddies as well as from some time-mean flow, and that these 'eddy-eddy' interactions are probably more vigorous than the eddy-mean flow interaction, except in regions of intense currents. The growth-rates of the instability theory are reasonably close to the spectral transfer rates found in turbulence, and the structural similarity of theory and experiments is revealing.

Background

The unexpected discovery of energetic, highly variable currents from the research vessel Aries in the deep western North Atlantic Ocean (Crease, 1962) opened a new chapter in the dynamics of ocean circulation (see Fig. 1.1): the float trajectories revealed relatively high speeds at nominal depths of 2 and 4 km, of the order of 5 to 10 cm/sec, with an apparent period of 50 to 100 days (Swallow, 1971) and an estimated wavelength of 300 to 400 km (Phillips, 1966).

The hydrographic data from the Panulirus station near Bermuda show a very distinct month to month variation of temperature in the main thermocline as shown in Fig. 1.2 (Schroeder and Stommel 1969). The temperature spectrum constructed by Wunsch (1972a) from these data reveals that most of the variance in the main thermocline is located between the periods of 40 to 200 days as shown in Fig. 1.3. This band of periods is certainly in the same range as estimated from the Aries measurements.

In the sections of temperature and salinity from Fuglister (1960) various length scales can be picked by eye. Upon the basin-wide variation is superimposed wiggly structures with scales of hundreds of kilometers. The zonal variations of the 10°C isotherm depth at 24°S and 24°N are shown in Fig. 1.4. Counting the rise and fall of

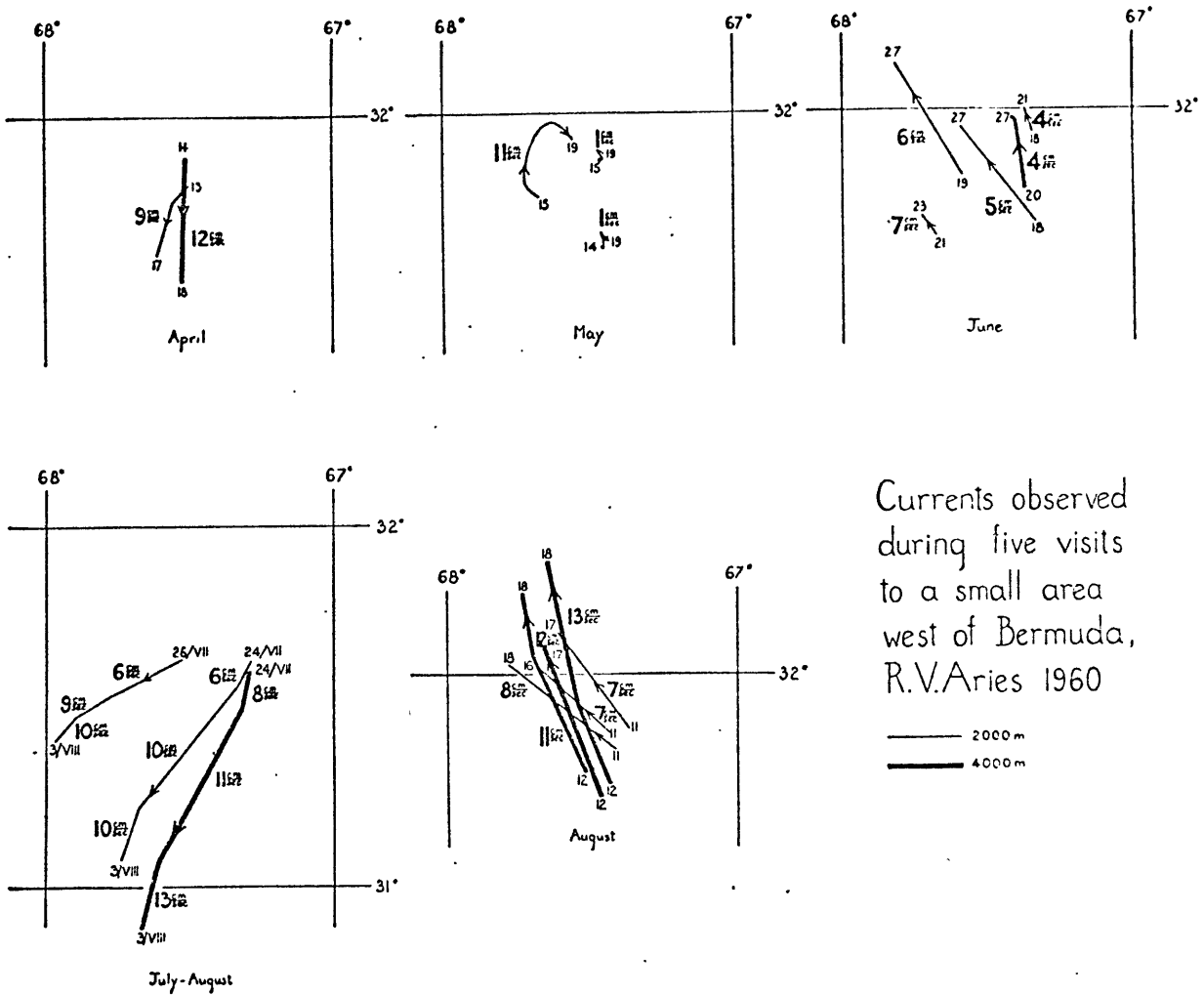


Fig. 1.1 From Crease(1962). Trajectories of five series of floats. Figures at ends of trajectory are starting and finishing dates. Figures beside trajectory are average speeds. Currents are very energetic with an apparent period of 50 to 100 days(Swallow,1971) and an estimated wave-length of 300 to 400 km(Phillips,1966). Current unit is cm/sec.

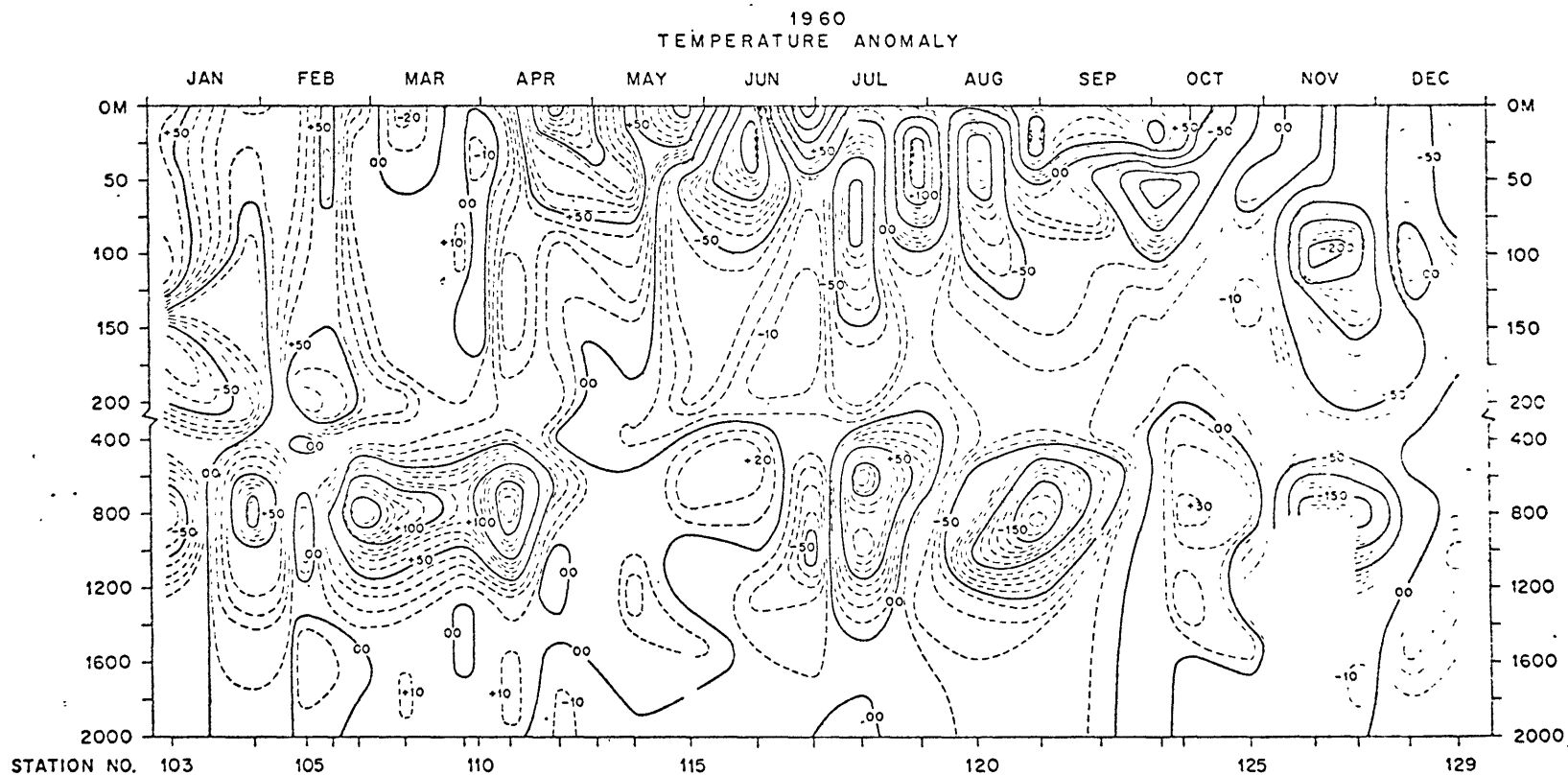


Fig. 1.2 From Schroeder and Stommel (1969). Temperature anomalies at the Panulirus station in 1960. Units: hundreds of a degree centigrade. Vertical scale changes at 200 m. Closed contours in the thermocline show a strong temporal variation. Anomaly of 1°C roughly corresponds to a vertical excursion of 50 m in the thermocline.

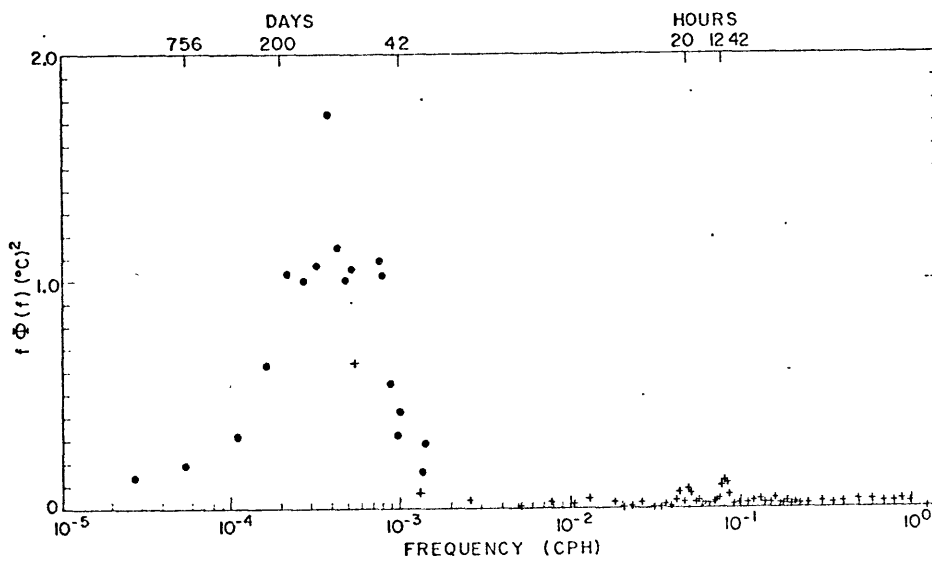


Fig. 1.3 From Wunsch(1972). Spectrum of temperature near Bermuda near the depth of the main thermocline, plotted so that the area under the curve is proportional to the variance of temperature. Most of the energy lies in periods of 40-200 days, indication a strong low frequency variation.

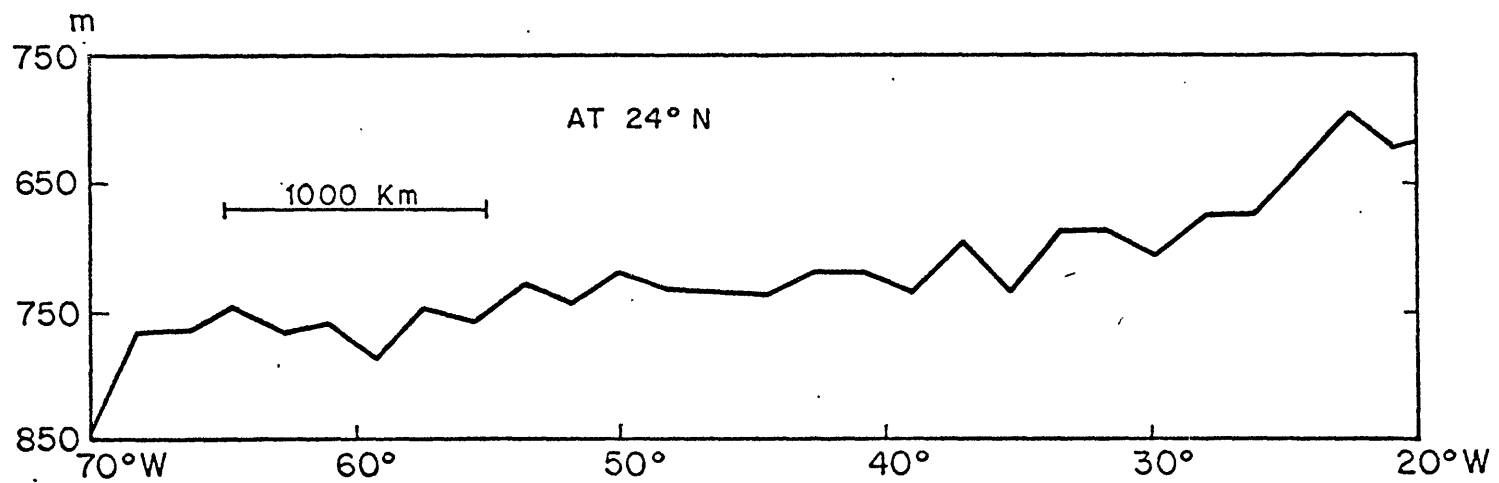
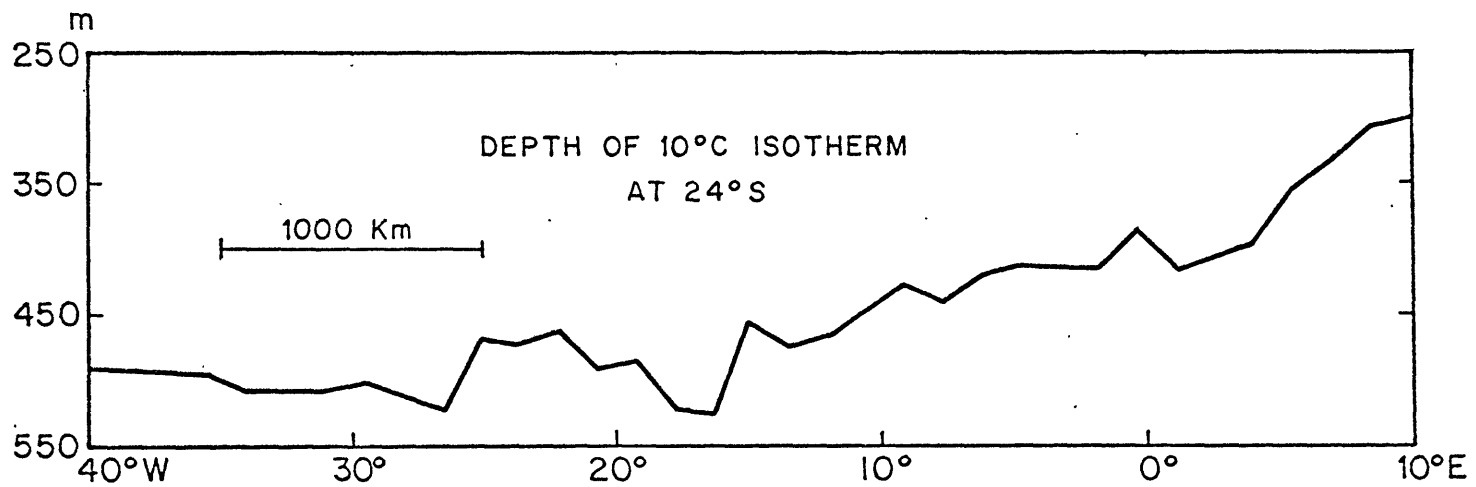


Fig. 1.4 Depth of 10°C isotherm from the data in Fuglister(1960). Sampling is sparse, but the presence of multiple scales is apparent at two separate sections.

the isotherm depth greater than 20 m between consecutive samplings, there are four minima at 24°S and six at 24°N over 5077 km. The distance between the minima varies from about 600 to 1000 km at 24°S and from about 450 to 1100 km at 24°N. Because of sparse sampling the horizontal resolution is inadequate to show the kind of variation corresponding to the Aries measurements. Nevertheless these comparisons are suggestive in implying the presence of multiple scales at two separated sections.

Katz's (1973) experiments have confirmed the presence of an intermediate scale in the open ocean in Fig. 1.5. The east-west distance between a peak and a valley is 180 km and the north-south is 360 km at least. The corresponding wavelengths will be 360 and 720 km respectively, which are somewhat larger than those estimated from the Aries observations. At the same time Katz's (1973) profiles suggest that small scales may have slightly (± 10 km) contaminated Fuglister's (1960) sections. It is very interesting to notice that the strong gradient in tow 300 in Fig. 1.5 along 64° 50'W approximately is not found in the nearest section at 66°W, indicating that Katz's profiles as well as the wiggles in Fuglister's sections are not permanent.

During the U.S.S.R. POLYGON experiment in the tropical North Atlantic a large-scale anti-cyclonic velocity disturbance was observed and Fig. 1.6 shows the average speed

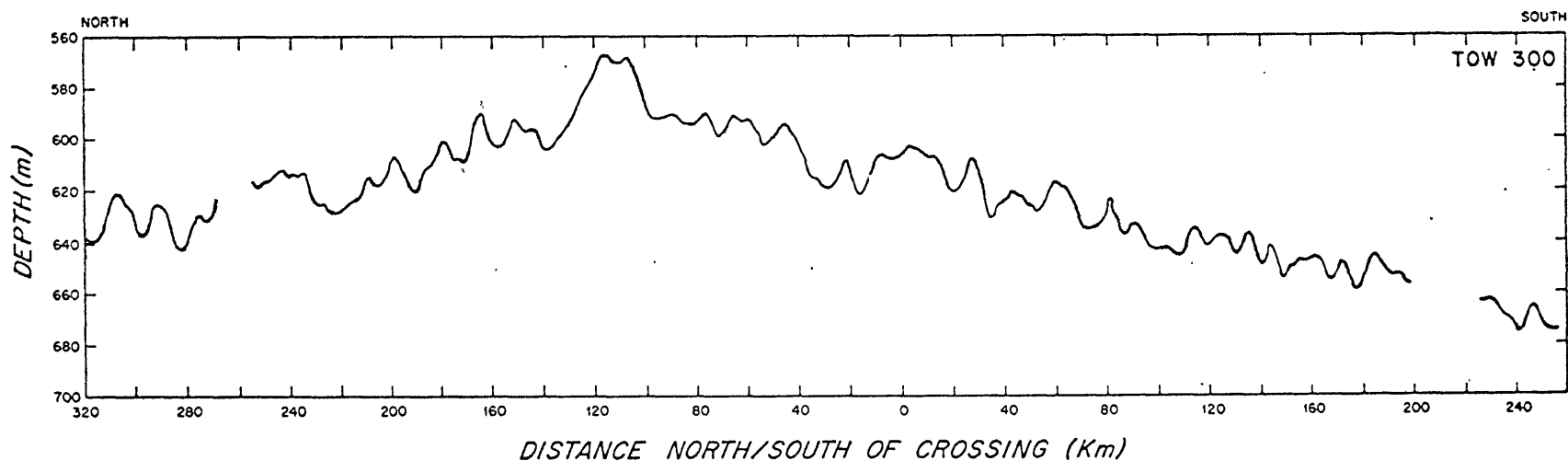
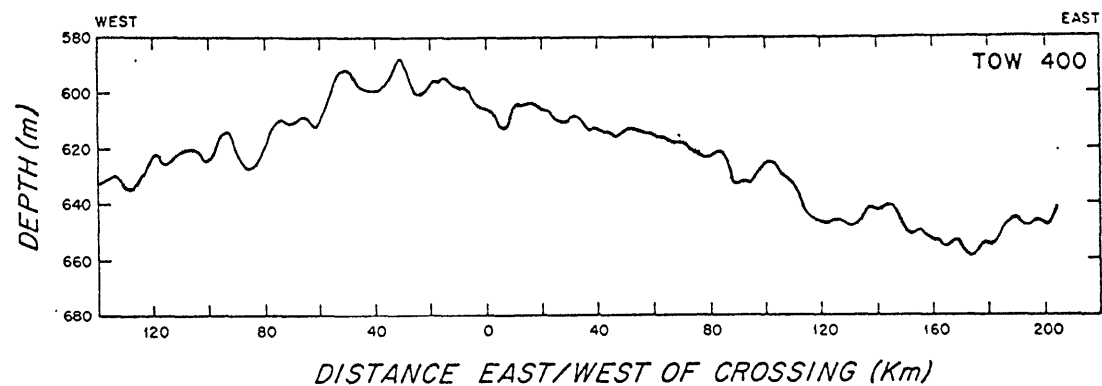


Fig. 1.5 From Katz (1973). Depth of isopycnals, $\sigma_t = 26.91$ for Tow 300 and $\sigma_t = 26.87$ for Tow 400. These profiles confirm the presence of an intermediate scale. The distance between a peak and a valley is 180 km from Tow 400 and 360 km from Tow 300 at least.

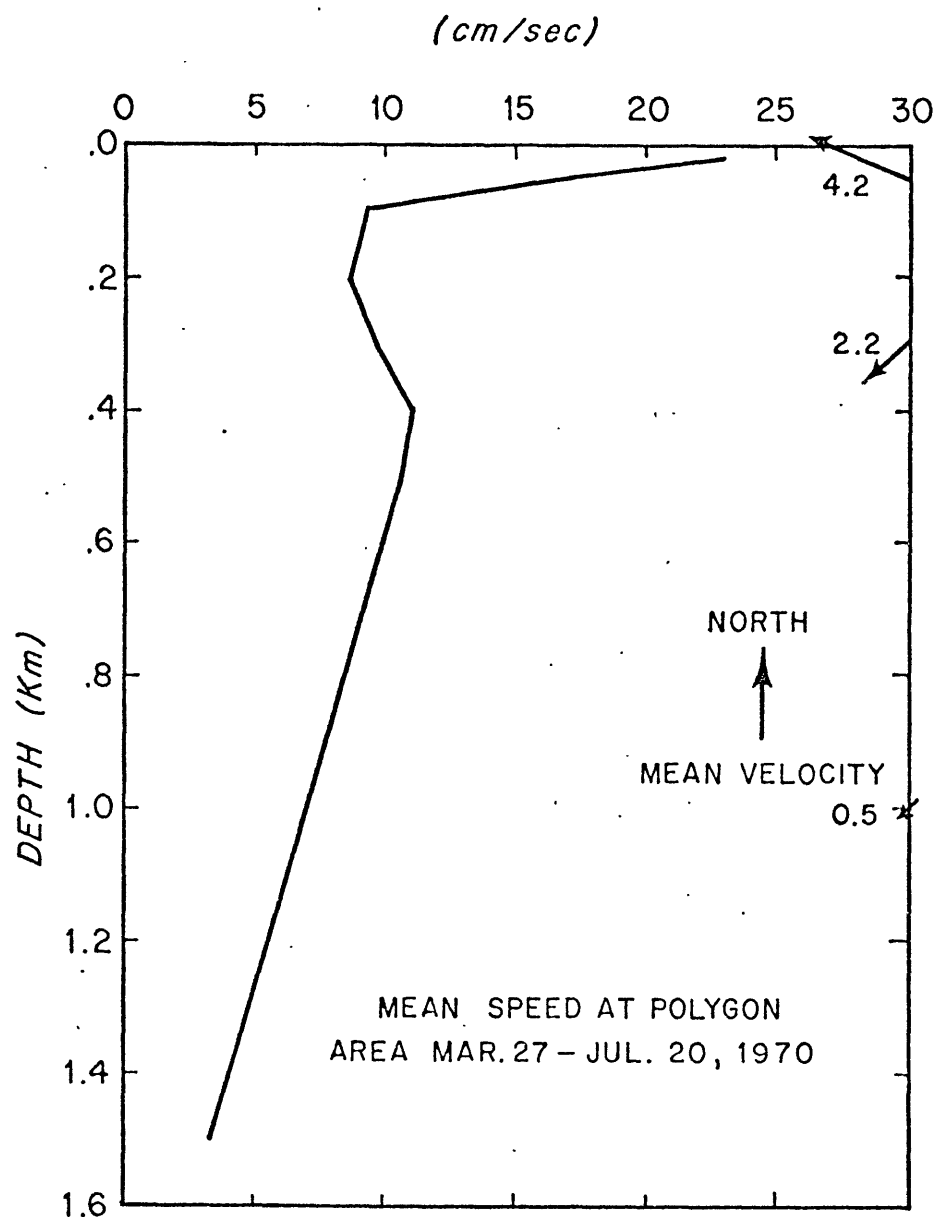


Fig. 1.6 Profile of mean speed and mean velocity plotted from Koshlyakov and Grachov (1973). A large-scale anti-cyclonic eddy was observed during the Polygon experiment and its mean speed is overwhelmingly larger than mean velocity for all depth. The main thermocline is located at about 250 m.

overwhelmingly larger than the average velocity from the surface to 1500 m depth. This is another important disclosure because the thermocline in the Polygon area is located at about 250 m, compared with about 800 m in the Sargasso Sea and the mean horizontal density gradient is much weaker by an order of magnitude.

Gould, Schmitz and Wunsch (1974) have suggested from estimates of vertical coherence of currents that the low frequency currents are usually dominated by the barotropic and first few baroclinic modes. The vertical profile of current in Fig. 1.7 from Sanford (1975) shows a very strong shear in the main thermocline which tends to justify the use of a simplified vertical structure in the present theory (two-layer ocean).

Bernstein and White (1974) reported oceanic subsurface perturbations in the central North Pacific and argued that these fluctuations are the manifestation of non-dispersive baroclinic planetary waves.

In summary, the last two decades' observations in the mid-ocean have consistently revealed the presence of energetic eddies with time scales of tens of days, length scales of tens to hundreds of kilometers and a strong vertical variation, irrespective of where and when the data were taken. The description of eddies is very subjective and indefinite because most experiments were in-

VELOCITY PROFILES 224U & 226U

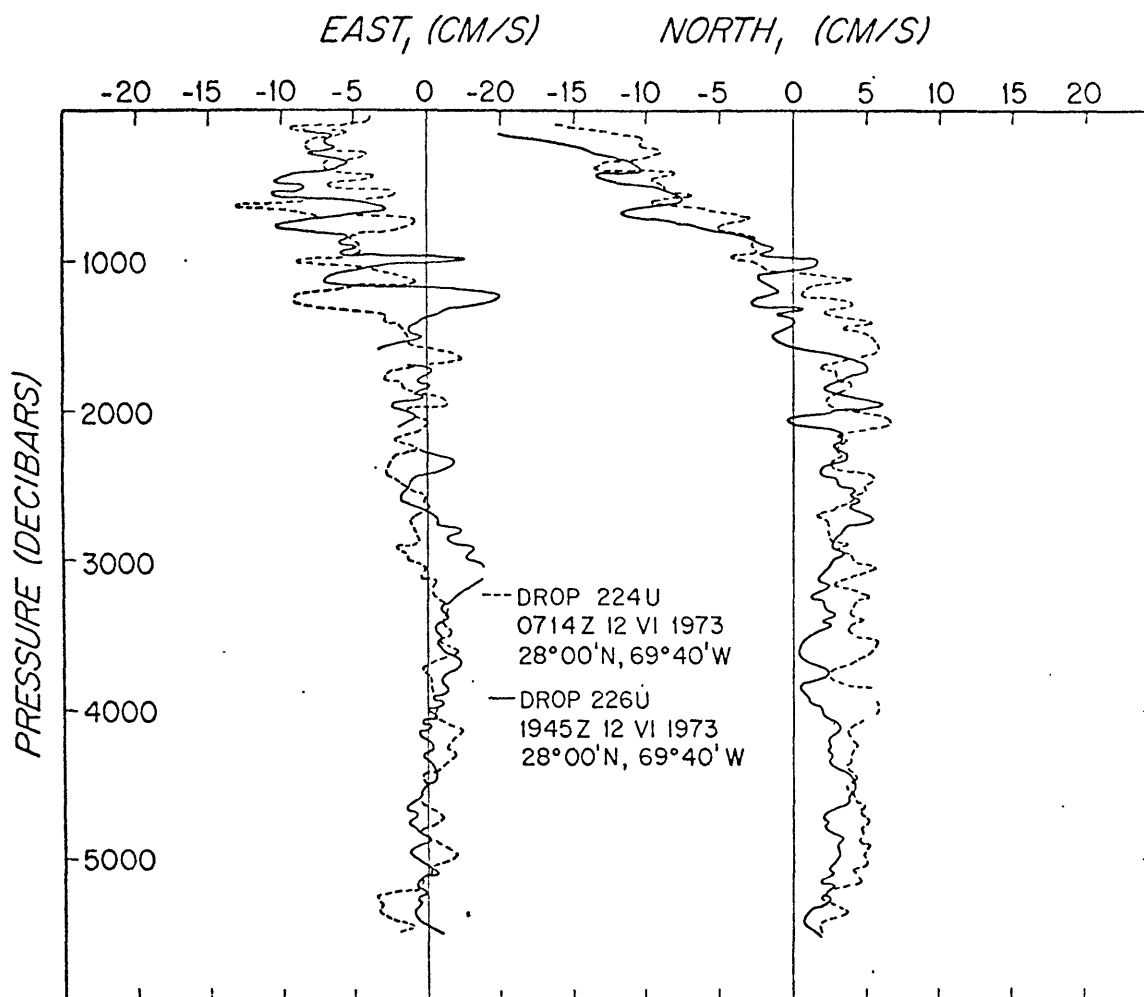


Fig. 1.7 From Sanford(1975). Velocity profiles show a strong shear concentrated in the main thermocline, suggesting the dominance of grave baroclinic mode.

sufficiently extensive in time and space to resolve the significant variations of eddies themselves. Also the description of eddies requires data in space and time simultaneously so that the Panulirus data are useful, for example, but their implication is very limited.

Previous theoretical models

What are the theoretical models for the observed eddies concerning their generation and evolution in the mid-ocean? There are two extreme lines of synthesizing the observations: the eddies may be a collection of unique events, each one from a different origin and in a different dynamic balance, or they are all from the same origin and in the same dynamic balance except for the fact that they happened to be observed at a different place and time. Neither of these ideas has been justified and it is believed to be premature to draw any conclusion regarding this subtle question at present because the available data are very limited compared with the complexity of dynamics involving the eddies.

However, in theory eddies can be represented by a few important parameters and possible eddy dynamics can be explored by investigating the nonlinear interactions in a parameter space, as done in this study. Some of previous theoretical models are examined here, first linear then nonlinear models, in order to show where the present

theory stands.

Considering the scales involved, it is apparent that the basic momentum balance is geostrophic, which is substantiated by Swallow (1971), Koshlyakov and Grachev (1973) and Bryden (1975). Veronis and Stommel (1956) have found two kinds of geostrophically-balanced waves in their study on the response of a two-layer ocean to a transient wind system. One of these is a barotropic Rossby wave for which fluid moves as a column, as if homogeneous, and the other is a baroclinic Rossby wave for which the two layers move in opposite directions. It is important to understand that the perturbations in the density field are attributed solely to the baroclinic mode. The dispersion relations of these waves in Fig. 1.8 show that the wavelengths and periods of the waves are not compatible with the observed scales. Nevertheless, these kinds of waves have been used extensively in interpreting short-term data by various authors. Notably Longuet-Higgins (1965a, b) and Phillips (1966) suggested that the Aries observation may be a sort of wind-generated barotropic and/or baroclinic Rossby wave. McWilliams and Flierl (1975) have succeeded in some rough aspects, in approximating a fit of MODE data. These kinds of simple description of the eddies as a superposition of linear, quasi-geostrophic waves seem to be successful over short times, but tend to produce a dynamically inconsis-

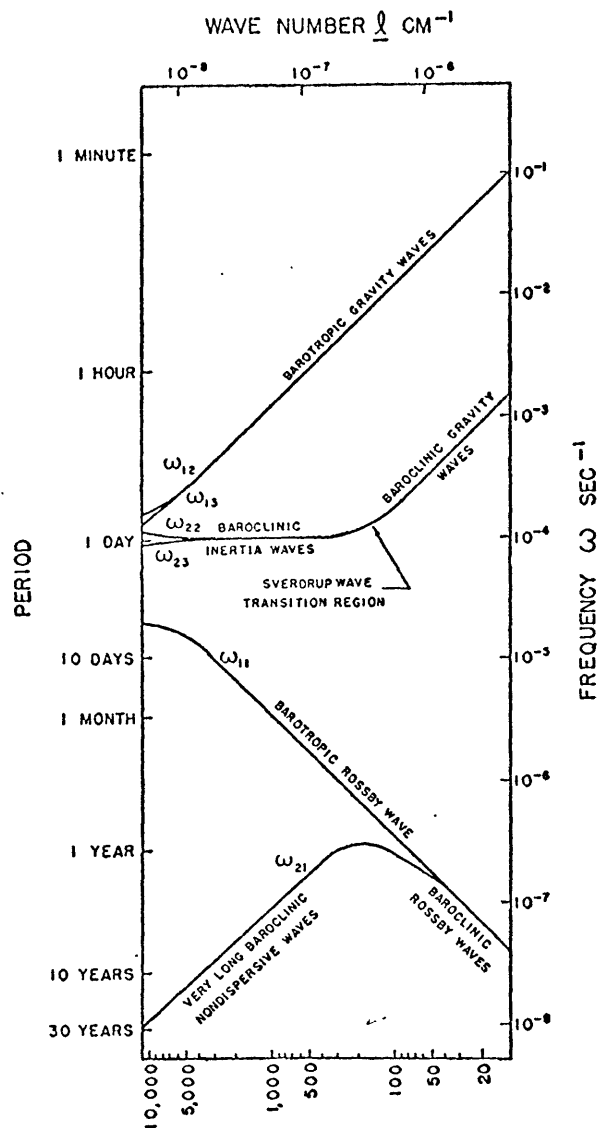


Fig. 1.8

From Veronis and Stommel (1956). The dispersion relations of barotropic and baroclinic Rossby waves in a two-layer ocean. Thicknesses of upper and lower layers are 500 m and 3500 m, respectively. $f=10^{-4}$ sec⁻¹, $\beta=2 \times 10^{-13}$ cm⁻¹³ sec⁻¹. The radius of deformation based upon the upper layer thickness is 31 km. Note that the minimum period of the baroclinic Rossby wave is about one year.

tent model, in which neglected nonlinear terms are large.

Rhines (1971) took a different dynamic balance where the stratification plays a major role in a vortex stretching over a sloping bottom, but pointed out the fact that nonlinearity is of order unity.

An estimate of nonlinearity for a thermocline eddy is typically

$$\frac{UT}{L} = \frac{10 \text{ cm/sec} \times 40 \text{ days}}{50 \text{ km}} \sim 6.9$$

where U is the characteristic velocity scale, T the time scale and L the length scale (scale being one cycle/ 2π). This may be smaller, but greater than unity, in the deep water, and gives a primary objection against applying linear models to eddies.

Recognizing the huge available potential energy embedded in the deep thermocline in the North Atlantic Ocean (Stommel, 1966) most of nonlinear models have been concerned with the baroclinic instability. The idea was tested by Schulman (1967), who found that a slow meridional current is baroclinically unstable in a manner similar to its atmospheric counterpart examined by Eady (1949). The e-folding time-scale is of the order of one year with a vertical shear of 1 cm/sec across the thermocline, which is a reasonable estimate of the basin-wide shear as can be seen in Fuglister's (1960) sections.

Recently more refined theories are suggested by Robinson and McWilliams (1974), and Gill, Green and Simmons (1974), in both cases a steady, zonal and horizontally uniform current being assumed as an unperturbed state. Robinson and McWilliams (1974) include the beta-effect, bottom topography and mean vertical shear in a two-layer model and obtain an e-folding time of two months for 5 cm/sec vertical shear. In a continuously stratified model Gill, Green and Simmons (1974) conclude that the energy conversion confined in the upper 400 m may be very important in eddy-generation.

In short, the baroclinic instability process has been referred to frequently as a generating mechanism of eddies in the mid-ocean, and within the boundary currents, because the theory predicts the scale of the most unstable perturbation consistent with the observations. The e-folding time scale can be as short as 60 to 80 days if the vertical shear across the main thermocline is as large as 5 cm/sec uniformly over a scale larger than the radius of deformation by an order of magnitude. If the shear is reduced by half, then the e-folding time scale is doubled. In reality, the uniform vertical shear in the mid-ocean may be a few cm/sec, substantially smaller than 5 cm/sec, which means an e-folding time scale close to one year as from Schulman (1967). Therefore it is doubtful that this process is a major

generating process of eddies. On the other hand it is clearly possible that the eddies themselves are more unstable than the weak mean circulation, since the growth rates are proportional to the baroclinic velocities. The stability of currents in which there is horizontal shear as well as vertical shear has been a controversy and in limited cases some numerical experiments (Brown 1969, Song 1971) and theoretical works (Stone, 1969; McIntyre, 1970; Simmons, 1974) have been carried out for a zonal current. These models are useful, but not enough, to access the properties of instabilities for a wide range of length and time scales.

Other shortcomings in the previous models are that the current in the basic state is strictly steady and zonal, which may be quite suitable in the atmosphere, but rather remote from an oceanic state.

Rhines (1975b) took the other interesting limit of nonlinear interaction in which the stratification is neglected. Here the migration of two-dimensional turbulence in a homogeneous fluid to larger scales ceases at a particular wavenumber $k_{\beta} = (\beta/2U)^{1/2}$, where β is the northward gradient of the Coriolis parameter. The inferred scale for the ocean is 70 km. This model does reproduce some of the properties of observed eddies, that is, the dual nature of nonlinear eddies, where both turbulent migration and wave

propagation are active. A more complete picture comes from stratified turbulence models (e.g., Rhines, 1975a).

Having discussed linear and nonlinear models, some specific questions are raised:

- (1) Are the linear, quasi-geostrophic waves stable?

Lorentz (1972) and Gill (1974) found that the barotropic Rossby wave is unstable, but the stability of the baroclinic Rossby wave remains to be answered.

- (2) What are the instability characteristics of a baroclinic current with a finite horizontal length- and time-scale? More specifically, suppose that there are present two dominant length scales. Their energy transfer may involve two length scales around the radius of deformation, or involve one scale around the radius of deformation and another scale much larger than the radius of deformation, such as the scale of the mean circulation. Which of these will be stronger and dominate signals during an experiment over a limited period?

- (3) Is it possible to generate larger eddies from smaller, in a stratified fluid as it is in a homogeneous fluid?

It is very interesting that the stability analysis of the baroclinic Rossby wave does provide a unique opportunity to answer these questions simultaneously. It is particularly relevant because the duality of oceanic eddies

can be kept naturally in the analysis. In Chapter II, basic equations are derived and their properties are discussed. Linearized perturbation equations are derived in Chapter III and the perturbation energy equation is used to examine how the perturbations interact with the unperturbed field specified as the baroclinic Rossby wave. In Chapter IV the perturbation equations are analysed in Fourier series and characteristics are found in truncated series. The mathematical results are interpreted physically in detail and compared with the previous theoretical results in Chapter V. The applications of this model in the ocean are also discussed. Finally conclusions are made in Chapter VI.

II. BASIC FORMULATION

II-1 Basic Equations in a Two-layer Ocean

The stratification of the ocean is idealized by the two homogeneous layers of slightly different densities and the fluid of each layer is assumed to be incompressible and inviscid. In addition the ocean is assumed to extend infinite horizontally.

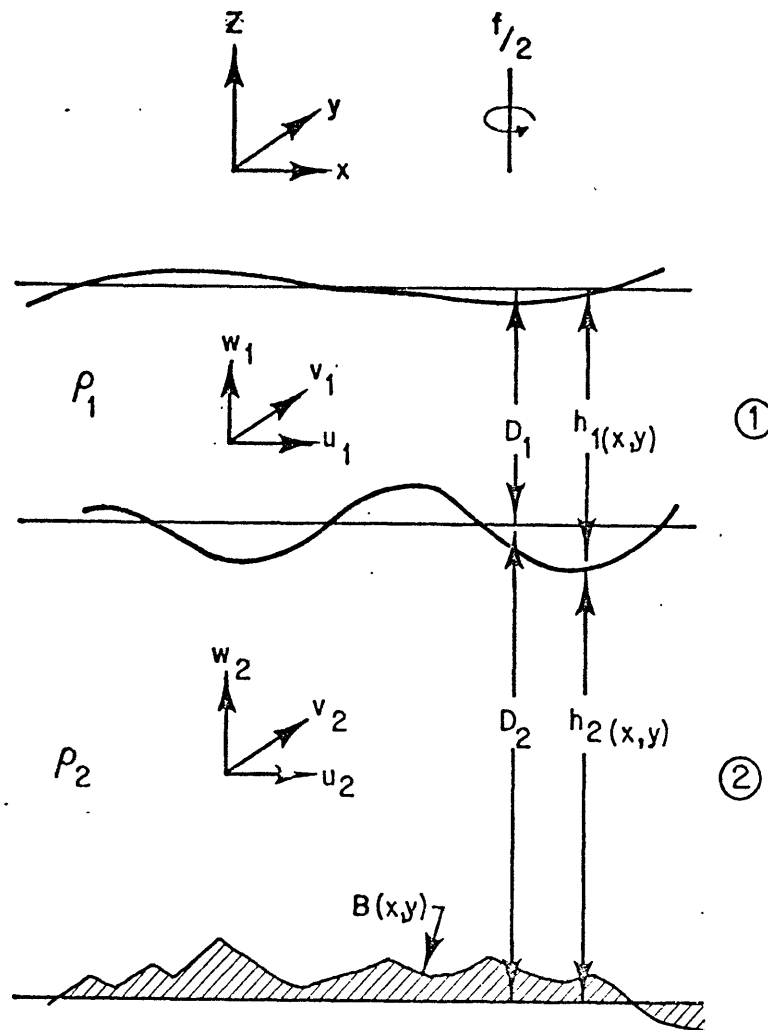
The dimensional equations of motion relative to the rotating earth are

$$\frac{\partial \vec{u}_\alpha}{\partial t} + (\vec{u}_\alpha \cdot \nabla) \vec{u}_\alpha + \vec{f} \times \vec{u}_\alpha = -\frac{1}{\rho_\alpha} \nabla p_\alpha - \vec{g}. \quad (2.1)$$

The continuity equation is

$$\nabla \cdot \vec{u}_\alpha = 0. \quad (2.2)$$

The subscripts $\alpha = (1,2)$ denote upper and lower layers respectively (see Fig. 2.1). The velocity vector \vec{u} has components (u,v,w) corresponding to positive eastward (x), northward (y) and upward (z) directions. The rotation vector \vec{f} is parallel to the axis of earth rotation and its magnitude is twice the earth's angular velocity. The density in the upper layer (ρ_1) is slightly lighter than that in the lower layer (ρ_2) and $\vec{g} = (0,0,g)$ is the effective



SCHÉMATIC CONFIGURATION OF A TWO-LAYER OCEAN

Fig. 2.1 The stratification of the ocean is idealized by two homogeneous layers of densities, ρ_1 and ρ_2 , where $\rho_1 < \rho_2$. Thickness of the upper layer is h_1 and h_2 is a height of the interface.

gravitational acceleration.

The boundary conditions are

$$\frac{\partial h}{\partial t} + (\vec{u}_1 \cdot \nabla) h = w_1 \quad \text{at } z = h \quad (h = h_1 + h_2) \quad (2.3a)$$

$$\frac{\partial h}{\partial t} + (\vec{u}_1 \cdot \nabla) h_2 = w_1 \quad \text{at } z = h_2 \quad (2.3b)$$

$$\frac{\partial h}{\partial t} + (\vec{u}_2 \cdot \nabla) h_2 = w_2 \quad \text{at } z = h_2 \quad (2.3c)$$

$$(\vec{u}_2 \cdot \nabla) B = w_2 \quad \text{at } z = B \quad (2.3d)$$

where $h_1(x,y)$, $h_2(x,y)$ and $B(x,y)$ represent the thickness of the upper layer, the height of the interface and the bottom configuration respectively. And there are two matching conditions at the interface: the vertical velocity and the pressure should be continuous.

Let the scales of the variables be

$$(x, y) = L(x', y')$$

$$z = Dz'$$

$$(u, v) = U(u', v')$$

$$w = U \delta R_0 w'$$

$$t = \frac{L}{U} t'$$

$$P_\alpha = \rho_\alpha f_0 UL$$

$$h = D(1 + R_0 F_e h')$$

$$h_1 = D_1 (1 + R_0 F_1 h_1')$$

$$h_2 = D_2 (1 + R_0 F_2 h_2')$$

with the relevant non-dimensional parameters

$$\delta = \frac{D}{L} \quad \text{aspect ratio}$$

$$R_0 = \frac{U}{f_0 L} \quad \text{Rossby number}$$

$$F_e = \frac{f_0^2 L^2}{gD} \quad \text{external Froude number}$$

$$F_i = \frac{f_0^2 L^2}{g'D} \quad \text{internal Froude number}$$

$$F_1 = \frac{f_0^2 L^2}{g'D_1} \quad \text{internal Froude number for the upper layer.}$$

$$F_2 = \frac{f_0^2 L^2}{g'D_2} \quad \text{internal Froude number for the lower layer}$$

where D_1 and D_2 are the mean thickness of layers,
 $D = D_1 + D_2$, $g' = \frac{\rho_2 - \rho_1}{\rho_2} g$ reduced gravitational acceleration and f_0 is the magnitude of the vertical component of \vec{f} at mid-latitude.

For the range of scales of interest the following can be shown.

- (i) The dynamic balance in the vertical direction is hydrostatic: $\delta \ll 1$.
- (ii) The horizontal motion is quasi-geostrophic: $R_0 < 1$.

- (iii) The beta-plane approximation is valid: the effect of the earth curvature is neglected except in the meridional variation of \vec{f} , $\frac{L}{a} \sim 0(R_0)$ where a is the mean radius of the earth.
- (iv) The horizontal component of the rotation vector \vec{f} is neglected. This is the "traditional" approximation appropriate to large horizontal scales, with strong stratification.
- (v) The displacement of the free surface is neglected compared with that of the interface.

From (iii) and (iv) the Coriolis parameter f can be written

$$f = f_0 \left(1 + \beta^* \frac{L}{a} y' \right).$$

For the upper layer the nondimensional forms of eqs. (2.1), (2.2), (2.3a) and (2.3b) with no primes on the nondimensional variables hereafter become

$$R_0 \left(\frac{\partial u}{\partial t} + u \frac{\partial u}{\partial x} + v \frac{\partial u}{\partial y} + R_0 w \frac{\partial u}{\partial z} \right) - (1 + \beta^* \frac{L}{a} y) v = - \frac{\partial p}{\partial x} \quad (2.4a)$$

$$R_0 \left(\frac{\partial v}{\partial t} + u \frac{\partial v}{\partial x} + v \frac{\partial v}{\partial y} + R_0 w \frac{\partial v}{\partial z} \right) + (1 + \beta^* \frac{L}{a} y) u = - \frac{\partial p}{\partial y} \quad (2.4b)$$

$$R_0 \delta^2 \left(\frac{\partial w}{\partial t} + u \frac{\partial w}{\partial x} + v \frac{\partial w}{\partial y} + R_0 w \frac{\partial w}{\partial z} \right) = - \frac{\partial p}{\partial z} \quad (2.4c)$$

with the hydrostatic pressure (P_s), which balances g

such as $0 = - \frac{1}{\rho_1} \frac{\partial P_s}{\partial z} - g.$

$$\frac{\partial u_1}{\partial x} + \frac{\partial v_1}{\partial y} + R_0 \frac{\partial w_1}{\partial z} = 0 \quad (2.5)$$

$$R_0 F_e \left(\frac{\partial h}{\partial t} + u_1 \frac{\partial h}{\partial x} + v_1 \frac{\partial h}{\partial y} \right) = R_0 w_1 \quad \text{at } z = 1 + R_0 F_e h \quad (2.6a)$$

$$R_0 F_i \left(\frac{\partial h}{\partial t} + u_1 \frac{\partial h}{\partial x} + v_1 \frac{\partial h}{\partial y} \right) = R_0 w_1 \quad \text{at } z = (1 + R_0 F_e h_2) \frac{D}{D} \quad (2.6b)$$

The nondimensional variables are formally expanded in a power series of R as $p_1 = \sum_{n=0}^{\infty} R_0^n p_1^{(n)}$. The equations of the zeroth order are

$$-v_1^{(0)} = -\frac{\partial p_1^{(0)}}{\partial x} \quad (2.7a)$$

$$u_1^{(0)} = -\frac{\partial p_1^{(0)}}{\partial y} \quad (2.7b)$$

$$0 = -\frac{\partial p_1^{(0)}}{\partial z} \quad (2.7c)$$

$$\frac{\partial u_1^{(0)}}{\partial x} + \frac{\partial v_1^{(0)}}{\partial y} = 0 \quad (2.8)$$

Eqs. (2.7a,b,c) show that the zeroth order flow is non-divergent and the pressure is the stream function of the flow, independent of z by eq. (2.7c).

The first order equations become

$$\frac{\partial u_1^{(0)}}{\partial t} + u_1^{(0)} \frac{\partial u_1^{(0)}}{\partial x} + v_1^{(0)} \frac{\partial u_1^{(0)}}{\partial y} - v_1^{(1)} - \beta y v_1^{(1)} = -\frac{\partial p_1^{(1)}}{\partial x} \quad (2.9a)$$

$$\frac{\partial v_1^{(0)}}{\partial t} + u_1^{(0)} \frac{\partial v_1^{(0)}}{\partial x} + v_1^{(0)} \frac{\partial v_1^{(0)}}{\partial y} + u_1^{(1)} \frac{\partial v_1^{(0)}}{\partial y} + \beta y u_1^{(0)} = -\frac{\partial p_1^{(1)}}{\partial y} \quad (2.9b)$$

$$0 = -\frac{\partial p_1^{(1)}}{\partial z} \quad (2.9c)$$

$$\frac{\partial u_1^{(1)}}{\partial x} + \frac{\partial v_1^{(1)}}{\partial y} + \frac{\partial w_1^{(0)}}{\partial z} = 0 \quad (2.10)$$

$$F_e \left(\frac{\partial h^{(0)}}{\partial t} + u_1^{(0)} \frac{\partial h^{(0)}}{\partial x} + v_1^{(0)} \frac{\partial h^{(0)}}{\partial y} \right) = w_1 \quad \text{at } z = 1 + R_0 F_e h^0 \quad (2.11a)$$

$$F_i \left(\frac{\partial h^{(0)}}{\partial t} + u_1^{(0)} \frac{\partial h^{(0)}}{\partial x} + v_1^{(0)} \frac{\partial h^{(0)}}{\partial y} \right) = w_1 \quad \text{at } z = (1 + R_0 F_2 h_2^0) \frac{D}{2} \quad (2.11b)$$

where $\beta = \frac{\beta^* L}{R_0 a}$, which is assumed to be of order unity by the assumption (iii). The cross-differentiation of eqs. (2.9a,b) yields

$$\left(\frac{\partial}{\partial t} + u_1^{(0)} \frac{\partial}{\partial x} + v_1^{(0)} \frac{\partial}{\partial y} \right) \left(\frac{\partial v_1^{(0)}}{\partial x} - \frac{\partial u_1^{(0)}}{\partial y} \right) + \frac{\partial u_1^{(1)}}{\partial x} + \frac{\partial v_1^{(1)}}{\partial y} + \beta v_1^{(0)} = 0. \quad (2.12)$$

Substituting eq. (2.10) for the horizontal divergence in eq. (2.12) and integrating eq. (2.12) vertically through the layer and applying the boundary conditions we obtain

$$\left(\frac{\partial}{\partial t} + u_1^{(0)} \frac{\partial}{\partial x} + v_1^{(0)} \frac{\partial}{\partial y}\right) \left(\frac{\partial v_1^{(0)}}{\partial x} - \frac{\partial u_1^{(0)}}{\partial y} + F_1 h_2^{(0)} + \beta y\right) = 0 \quad (2.13)$$

In this derivation the vertical velocity at the free surface is put to zero because $F_e \ll F_i$ by assumption (v). Eq. (2.13) is a vorticity equation for the upper layer, which states that the rate of change of relative plus planetary vorticity is due to the stretching of the column of the fluid via the vertical displacement of the interface.

For the lower layer the same procedure with boundary conditions at the interface and the bottom yields another vorticity equation.

$$\left(\frac{\partial}{\partial t} + u_2^{(0)} \frac{\partial}{\partial x} + v_2^{(0)} \frac{\partial}{\partial y}\right) \left(\frac{\partial v_2^{(0)}}{\partial x} - \frac{\partial u_2^{(0)}}{\partial y} - F_2 h_2^{(0)} + \beta y + \frac{\hat{B}}{DR_0} b\right) = 0 \quad (2.14)$$

where \hat{B} is the scale of amplitude of topographic variation and it is assumed that $\frac{\hat{B}}{DR_0} \leq 0(1)$.

The continuity of pressure at the interface requires $\rho_2 h_2^{(0)} = \rho_2 p_2^{(0)} - \rho_1 p_1^{(0)}$. Because $\rho_2 - \rho_1 \ll \rho_2$, we may approximate

$$h_2^{(0)} \approx p_2^{(0)} - p_1^{(0)}. \quad (2.15)$$

Eq. (2.15) satisfies the matching condition of vertical velocity automatically. Utilizing the pressure as a stream function, we may rewrite eqs. (2.13) and (2.14) with (2.15).

$$\left[\frac{\partial}{\partial t} + J(\psi_1, \cdot) \right] (\nabla^2 \psi_1 + F_1(\psi_2 - \psi_1) + \beta y) = 0 \quad (2.16)$$

$$\left[\frac{\partial}{\partial t} + J(\psi_2, \cdot) \right] (\nabla^2 \psi_2 + F_2(\psi_1 - \psi_2) + \beta y + \frac{\hat{B}}{R_0 D} b) = 0 \quad (2.17)$$

where $\psi_1 = p_1^{(0)}$, $\psi_2 = p_2^{(0)}$. And the Jacobian operators are used in the advection terms such as $J(\psi_1, \cdot) \equiv u \frac{\partial}{\partial x} + v \frac{\partial}{\partial y}$.

Large-scale dynamics controlled by the bottom have been investigated by many authors (Rhines (1970), McCartney (1975), Freeland, Rhines and Rossby (1975)) and its effect in the nonlinear processes may be very significant (Rhines, private communication), if typical values of $\hat{B}/R_0 D$ approach or exceed unity. However, in this study the efforts will be concentrated on understanding the dynamics which are controlled internally, neglecting the bottom effect.

II-2 Energy Conservation

For a flat bottom ocean the basic equations (2.16) and (2.17) are written in a tensor notation for convenience in deriving energy equations.

$$\left[\frac{\partial}{\partial t} + \epsilon_{\alpha\beta} \frac{\partial \psi_1}{\partial x_\alpha} \frac{\partial}{\partial x_\beta} \right] \left\{ \frac{\partial}{\partial x_i} \frac{\partial}{\partial x_i} \psi_1 + F_1(\psi_2 - \psi_1) + \beta y \right\} = 0 \quad (2.18a)$$

$$\left[\frac{\partial}{\partial t} + \epsilon_{\alpha\beta} \frac{\partial \psi_2}{\partial x_\alpha} \frac{\partial}{\partial x_\beta} \right] \left\{ \frac{\partial}{\partial x_i} \frac{\partial}{\partial x_i} \psi_2 + F_2(\psi_1 - \psi_2) + \beta y \right\} = 0 \quad (2.18b)$$

where $\epsilon_{\alpha\beta}$ is the permutation tensor of the second order and $i = (1,2)$. With an identity

$$\epsilon_{\alpha\beta} \frac{\partial \psi_1}{\partial x_\alpha} \frac{\partial}{\partial x_\beta} \frac{\partial}{\partial x_i} \frac{\partial}{\partial x_i} \psi_1 = \epsilon_{\alpha\beta} \frac{\partial}{\partial x_i} \left(\frac{\partial \psi_1}{\partial x_\alpha} \frac{\partial}{\partial x_\beta} \frac{\partial}{\partial x_i} \psi_1 \right)$$

multiplying eq. (2.18a) by ψ_1 , we obtain

$$\frac{d}{dt} \left(\frac{1}{2F_1} \frac{\partial \psi_1}{\partial x_i} \frac{\partial \psi_1}{\partial x_i} \right) + \psi_1 \frac{\partial}{\partial t} (\psi_1 - \psi_1) = \frac{\partial}{\partial x_i} \left(\frac{\psi_1}{F_1} \frac{d}{dt} \frac{\partial \psi_1}{\partial x_i} \right) + J \left(\frac{1}{2} \psi_1^2, \frac{1}{F_1} \beta y + \psi_2 - \psi_1 \right) \quad (2.19a)$$

where $\frac{d_i}{dt} \equiv \frac{\partial}{\partial t} + u_i \frac{\partial}{\partial x} + v_i \frac{\partial}{\partial y}$ ($i = 1,2$).

Similarly the equation for the lower layer takes the form of

$$\frac{d}{dt} \left(\frac{1}{2F_2} \frac{\partial \psi_2}{\partial x_i} \frac{\partial \psi_2}{\partial x_i} \right) + \psi_2 \frac{\partial}{\partial t} (\psi_2 - \psi_1) = \frac{\partial}{\partial x_i} \left(\frac{\psi_2}{F_2} \frac{d}{dt} \frac{\partial \psi_2}{\partial x_i} \right) + J \left(\frac{1}{2} \psi_2^2, \frac{1}{F_2} \beta y + \psi_1 - \psi_2 \right) \quad (2.19b)$$

The sum of eqs. (2.19a,b) yields the energy equation:

$$\frac{d}{dt} (KE_1 + PE_1) + \frac{d}{dt} (KE_2 + PE_2) = \nabla \cdot \left\{ \left(\frac{\psi_1}{F_1} \frac{d}{dt} \nabla \psi_1 + \frac{\psi_2}{F_2} \frac{d}{dt} \nabla \psi_2 \right) - \frac{1}{2} \left(\frac{1}{F_1} \psi_1^2 + \frac{1}{F_2} \psi_2^2 \right) \hat{k} \times \nabla (\beta y) \right\} \quad (2.20)$$

with the definitions of energy densities

$$KE_1 \equiv \frac{1}{2F_1} (\nabla\psi_1 \cdot \nabla\psi_1) \equiv \frac{1}{2F_1} (u_1^{(0)^2} + v_1^{(0)^2}) : \text{kinetic energy density in the upper layer,}$$

$$KE_2 \equiv \frac{1}{2F_2} (\nabla\psi_2 \cdot \nabla\psi_2) = \frac{1}{2F_2} (u_2^{(0)^2} + v_2^{(0)^2}) : \text{kinetic energy density in the lower layer,}$$

$$PE_1 = PE_2 \equiv \frac{1}{4} (\psi_2 - \psi_1)^2 = \frac{1}{4} (h_2^{(0)})^2 : \text{potential energy density, which is formally divided into two layers.}$$

It is possible to show that the terms in the right hand side of eq. (2.20) represents the pressure work.

For a closed basin with zero normal velocity on the boundary, the integration of eq. (2.20) gives

$$\frac{\partial}{\partial t} \iint \left\{ \frac{1}{2F_1} \nabla\psi_1 \cdot \nabla\psi_1 + \frac{1}{2F_2} \nabla\psi_2 \cdot \nabla\psi_2 + \frac{1}{2} (\psi_2 - \psi_1)^2 \right\} dx dy = 0 \quad (2.21)$$

Therefore the total energy of the closed basin is conserved.

II-3 Exact Solutions of the Basic Equations and Their Stability

It is well-known that the eqs. (2.16, 17) have exact solutions, holding for arbitrarily large amplitude.

(i) Barotropic Rossby wave: The stream functions are

$$\begin{pmatrix} \psi_1 \\ \psi_2 \end{pmatrix} = \begin{pmatrix} 1 \\ 1 \end{pmatrix} \psi_0 \sin (kx + \ell y - \omega_T t)$$

with the dispersion relation $\omega_T = \frac{-\beta k}{k^2 + \ell^2}$.

Correspondingly, $h_2^{(0)} \equiv 0$ and the horizontal motions in two layers are in phase vertically.

(ii) Baroclinic Rossby wave: The solutions are

$$\begin{pmatrix} \psi_1 \\ \psi_2 \end{pmatrix} = \begin{pmatrix} F_1 \\ -F_2 \end{pmatrix} \psi_0 \sin (kx + \ell y - \omega_C t)$$

with $\omega_C = \frac{-\beta k}{k^2 + \ell^2 + F_1 + F_2}$. The motions are out of

phase by 180° .

(iii) Steady zonal current: In the limit $k \rightarrow 0$, the frequencies of both waves go to zero. Therefore steady zonal currents exist as particular cases of barotropic and baroclinic Rossby waves. The current can be either barotropic or baroclinic.

In fact, the same dispersion relations have been derived in a linearized model by Veronis and Stommel (1956

), which are shown in Fig. 1.8 ; the dispersion relations are the same, because the wave-like solutions of the basic nonlinear equations are exact,

the advection terms cancelling each other identically. It is obvious that the superposition of many different waves does not satisfy the nonlinear equations.

The stability of the current configurations described by these exact solutions have been investigated extensively by various authors, except for the baroclinic Rossby wave. Some of these earlier studies are relevant here, for example:

- (i) Instability of the zonal current in a barotropic fluid: The existence of the absolute vorticity extreme is necessary for instability (Kuo, 1949).
- (ii) Instability of the baroclinic zonal current in a two-layer system: The potential vorticity gradient must be somewhere positive and somewhere negative for instability to occur. For a horizontally uniform current this condition requires a minimum vertical shear to overcome a stabilizing beta-effect (Pedlosky, 1964a). There exists a short wavelength limit of unstable perturbations and the constant phase lines of growing perturbation tilt opposite to the vertical shear (Bretherton, 1966). The Reynolds stresses incorporated with the weak horizontal shear intensify the shear (Simmons, 1974). Physical explanations of (i) and (ii) in terms of vorticity-induction have been given by Lin (1955, p. 57) and Bretherton (1966), respectively.

(iii) Instability of a barotropic Rossby wave: Lorenz (1972) and Gill (1974) have shown that a single wave can break down via a generalized kind of shear instability, either with large or small amplitude of the primary wave.

III. PERTURBATION EQUATIONS

III-1 Linearized Perturbation Equations

The subject of this study is the stability of the baroclinic Rossby wave. For a convenience of analysis it is assumed that the two layers are of equal depth H and the effect of different depth will be discussed in Chapter V. The wave considered propagates due west with a wavenumber vector $(k, 0)$. Therefore the unperturbed state is described by

$$\begin{pmatrix} \psi_1 \\ \psi_2 \end{pmatrix} = \begin{pmatrix} 1 \\ -1 \end{pmatrix} \frac{U}{k} \sin(k(x - Ct)) \quad (3.1)$$

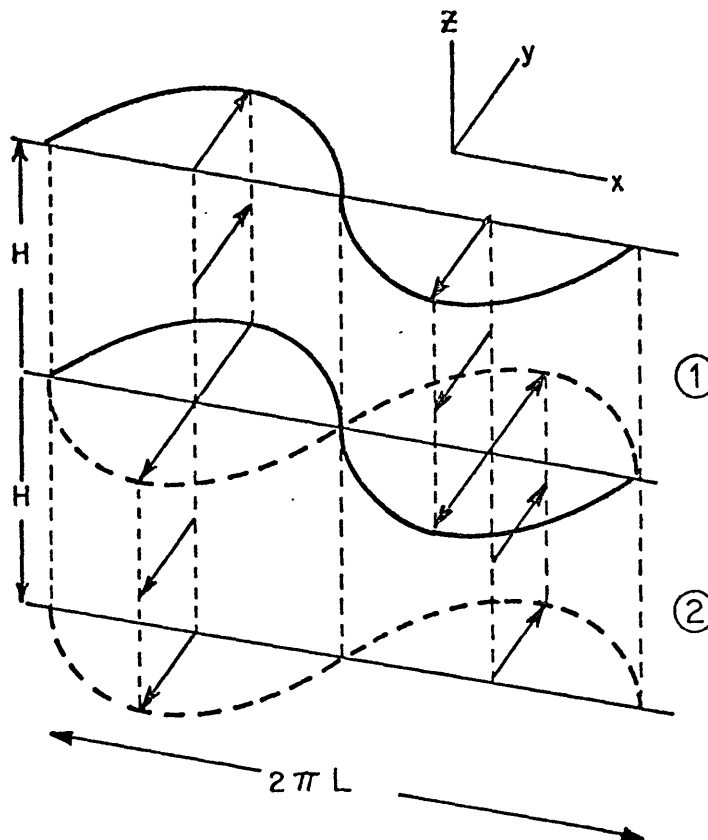
where the phase velocity C is determined by

$$C = \frac{-\beta}{k^2 + 2F} \quad (3.2)$$

with $F = \frac{f^2 L^2}{g^2 H}$. The corresponding velocities are

$(0, U \cos k(x-Ct))$ and $(0, -U \cos k(x-Ct))$ in the upper and lower layers, respectively. Fig. 3.1 shows schematically the velocity field, which is characterized by the sinusoidally varying horizontal structure and the vertical shear concentrated at the interface.

Assuming infinitesimal perturbation stream function ϕ_α ($\alpha = 1, 2$) such that $|\phi_\alpha| \ll |\psi_\alpha|$ superposed on the



$$V_1(x) = U \cos(k(x-Ct))$$

$$V_2(x) = -V_1(x)$$

VELOCITY STRUCTURE OF A BAROCLINIC ROSSBY WAVE

Fig. 3.1 The velocity structure of the basic wave is characterized by the presence of horizontal shear as well as vertical shear, associated with kinetic and potential energies respectively, which are partitioned by $(L_\rho/L)^2$, where L_ρ is the internal radius of deformation.

unperturbed state, we obtain the following linearized perturbation equations

$$\frac{\partial}{\partial t} \{ \nabla^2 \phi_1 + F(\phi_2 - \phi_1) \} + U \cos k(x-Ct) \frac{\partial}{\partial y} \{ \nabla^2 \phi_1 + (F+k^2) \phi_1 + F\phi_2 \} + \beta \frac{\partial \phi_1}{\partial x} = 0, \quad (3.3a)$$

$$\frac{\partial}{\partial t} \{ \nabla^2 \phi_2 + F(\phi_1 - \phi_2) \} - U \cos k(x-Ct) \frac{\partial}{\partial y} \{ \nabla^2 \phi_2 + (F+k^2) \phi_2 + F\phi_1 \} + \beta \frac{\partial \phi_2}{\partial x} = 0. \quad (3.3b)$$

Here the quadratic terms in ϕ_α from eq. (2.16, 2.17) are neglected, while the advections of the unperturbed potential vorticity by the perturbation velocity and of the perturbation potential vorticity by the unperturbed are included. Since the unperturbed state is propagating, it is convenient to analyze the stability in the coordinate frame moving with the phase speed C . The necessary transformations are

$$\begin{aligned} x_0 &= x - Ct \\ y_0 &= y \\ t_0 &= t. \end{aligned}$$

In the new frame eqs. (3.3a,b) become

$$\frac{\partial}{\partial t} \{ \nabla^2 \phi_1 + F(\phi_2 - \phi_1) \} - [C \frac{\partial}{\partial x} - U \cos kx] \frac{\partial}{\partial y} \{ \nabla^2 \phi_1 + (F+k^2) \phi_1 + F\phi_2 \} = 0 \quad (3.4a)$$

$$\frac{\partial}{\partial t} \{ \nabla^2 \phi_2 + F(\phi_1 - \phi_2) \} - [C \frac{\partial}{\partial x} + U \cos kx \frac{\partial}{\partial y}] \{ \nabla^2 \phi_2 + (F+k^2) \phi_2 + F \phi_1 \} = 0 \quad (3.4b)$$

where the subscripts on the new coordinates are omitted and the substitution $\beta = -C(k^2+2F)$ from eq. (3.2) is made for the last terms in eqs. (3.3a,b).

III-2 Energy Equation for the Perturbation

From eqs. (3.4a,b) it is possible to derive the equation of perturbation energy, which will serve as an important guideline in the perturbation analysis and its physical interpretation. After a similar manipulation done in deriving the energy equation in Section II-2 we get

$$\frac{\partial}{\partial t} \left\{ \frac{1}{2F} (\nabla \phi_1 \cdot \nabla \phi_1 + \nabla \phi_2 \cdot \nabla \phi_2) + \frac{1}{2} (\phi_2 - \phi_1)^2 \right\} = \nabla \cdot (\phi_1 \frac{\partial}{\partial t} \nabla \phi_1) + \nabla \cdot (\phi_2 \frac{\partial}{\partial t} \nabla \phi_2) \quad (3.5)$$

$$-\phi_1 [C \frac{\partial}{\partial x} - V_1(x) \frac{\partial}{\partial y}] \left\{ \frac{1}{F} \nabla^2 \phi_1 + \phi_1 + \phi_2 + \frac{k^2}{F} \phi_1 \right\}$$

$$-\phi_2 [C \frac{\partial}{\partial x} - V_2(x) \frac{\partial}{\partial y}] \left\{ \frac{1}{F} \nabla^2 \phi_2 + \phi_2 + \phi_1 + \frac{k^2}{F} \phi_2 \right\}$$

where $V_1(x) = U \cos kx$ and $V_2(x) = -V_1(x)$. It is assumed that the perturbation stream functions are periodic in space, i.e.

$$\phi_\alpha(x, y) = \phi_\alpha(x + \frac{2\pi}{k}, y) = \phi_\alpha(x, y + \frac{2\pi}{l})$$

where $\frac{2\pi}{k}$ is the wavelength of the unperturbed wave and $\frac{2\pi}{\ell}$ an undetermined meridional wavelength of the perturbation. Integration of eq. (3.5) over a cycle in space yields

$$\begin{aligned} \frac{\partial}{\partial t} \iint_{\text{cycle}} \left[\frac{1}{2F} (\nabla\phi_1 \cdot \nabla\phi_1 + \nabla\phi_2 \cdot \nabla\phi_2) + \frac{1}{2} (\phi_2 - \phi_1)^2 \right] dx dy = \\ \iint_{\text{cycle}} (V_1(x) - V_2(x)) \phi_1 \frac{\partial\phi}{\partial y} dx dy + \\ \iint_{\text{cycle}} \frac{1}{F} \left[\frac{dV}{dx} \frac{\partial\phi}{\partial x} \frac{\partial\phi}{\partial y} + \frac{dV}{dx} \frac{\partial\phi}{\partial x} \frac{\partial\phi}{\partial y} \right] dx dy. \end{aligned} \quad (3.6)$$

The integration of the terms multiplied by C in eq. (3.5) vanishes, because the perturbation is assumed to be periodic.

The definition of perturbation energies is very apparent in eq. (3.6): $\frac{1}{2F} \nabla\phi_1 \cdot \nabla\phi_1$ and $\frac{1}{2F} \nabla\phi_2 \cdot \nabla\phi_2$ are the kinetic energy densities in each layer and $\frac{1}{2} (\phi_2 - \phi_1)^2$ the potential energy density. The rate of change of the total perturbation energy is determined by the energy transfer via the interaction between the perturbation and the unperturbed flow specified on the right hand side of eq. (3.6). The interaction associated with the vertical shear of the unperturbed state representing an available potential energy, (the first RHS term) will be called the baroclinic interaction and that involving the horizontal shear (the

second RHS term) representing an available kinetic energy, is the barotropic interaction. The first term is the familiar product of the perturbation heat flux and the temperature gradient, while the second is the product of Reynolds stress and mean horizontal shear. For the scales under consideration the Richardson number is much greater than unity, $R_i \equiv \frac{1}{F R_0^2}$, that the effect of the kinetic energy with the vertical shear is negligible.

The intensity of the two interactions is scaled by $1/F$: the baroclinic interaction dominates the barotropic if $F \gg 1$ and vice versa if $F \ll 1$. Because of its critical role in determining the instability characteristics of the current it is very important to have a good understanding regarding the nondimensional parameter F : it is a measure of the vortex stretching against the relative vorticity in eqs. (2.16,17) and the potential energy compared with the kinetic energy in eq. (2.21). The parameter F can be understood as a ratio of two length scales, $F = L^2/L_\rho^2$ with the radius of deformation defined as $L_\rho^2 \equiv \frac{g'H}{f^2}$. The radius of deformation is fixed internally by the stratification, rotation and depth.

III-3 Integral Properties of Perturbation

Some important instability characteristics can be found by specifying the perturbation stream functions even

before detailed analysis. The perturbations take the form of

$$\begin{pmatrix} \phi_1 \\ \phi_2 \end{pmatrix} = R e^{\left(\begin{matrix} \chi_1(x) \\ \chi_2(x) \end{matrix} \right)} e^{i(\ell y + \alpha t)} \quad (3.7)$$

where χ_1 and χ_2 are complex in general and assumed to be periodic. Substituting eq. (3.7) into eqs. (2.16, 17) and multiplying by χ_1^* and χ_2^* , complex conjugates of χ_1 and χ_2 respectively, and adding two equations we get

$$\begin{aligned} & i\alpha \{ \chi_1^* \chi_1' + \chi_2^* \chi_2' - \ell^2 (\chi_1^2 + \chi_2^2) - F(\chi_2 - \chi_1)^2 \} \\ & - C \{ \chi_1^* \{ \chi_1' + (F+k^2 - \ell^2) \chi_1 + F \chi_2 \} + \chi_2^* \{ \chi_2' + (F+k^2 - \ell^2) \chi_2 + F \chi_1 \} \} \\ & + i\ell U \cos kx \{ \chi_1^* \{ \chi_1' + (F+k^2 - \ell^2) \chi_1 + F \chi_2 \} - \\ & \quad \chi_2^* \{ \chi_2' + (F+k^2 - \ell^2) \chi_2 + F \chi_1 \} \} = 0 \end{aligned} \quad (3.8)$$

where the notation $q^2 \equiv q^*q$ and $q' \equiv \frac{dq}{dx}$ are used. Under the condition that the derivatives of x are also periodic, the integration of eq. (3.8) over $(0, \frac{2\pi}{k})$ yields

$$-\alpha E + CR + \ell UI = 0 \quad (3.9)$$

where $E = \int \{ \chi_1'^2 + \chi_2'^2 + \ell^2 (\chi_1^2 + \chi_2^2) + F(\chi_1 - \chi_2)^2 \} dx$

$$R = 2\text{Im} \int \{ \chi_1^* \chi_1' + \chi_2^* \chi_2' + (F+k^2-\ell^2) (\chi_1^* \chi_1 + \chi_2^* \chi_2) + F \chi_2^* \chi_1 \} dx$$

$$I = \int [\cos kx \{ -\chi_1'^2 + \chi_2'^2 + (F+k^2-\ell^2) (\chi_1^2 - \chi_2^2) \} + F \cos kx (\chi_1^* \chi_2 - \chi_2^* \chi_1) + k \sin kx (\chi_1^* \chi_1' - \chi_2^* \chi_2')] dx.$$

The integral E is positive definite, representing the total perturbation energy as in eq. (3.6) and R is real.

The imaginary part of eq. (3.9) gives

$$\alpha_i E = \ell U \int \text{Im} \{ 2F(\cos kx) \chi_1^* \chi_2 + k \sin kx (\chi_1^* \chi_1' - \chi_2^* \chi_2') \} dx \quad (3.10)$$

where α_i is the imaginary part of α . It can be shown easily that eq. (3.10) is essentially the same perturbation energy equation as eq. (3.6). The perturbation with a positive value of α_i will damp out and that with a negative value will amplify its magnitude exponentially in time. If we write

$$\chi_\alpha(x) = |\chi_\alpha(x)| e^{i \text{Im} \alpha(x)},$$

eq. (3.10) takes the form of

$$\alpha_i = \frac{\ell U \left[\int |\chi_1| |\chi_2| \sin(\Theta_2 - \Theta_1) \cos kx \, dx + \frac{k}{2F} \int (|\chi_1|^2 \Theta_1' - |\chi_2|^2 \Theta_2') \sin kx \, dx \right]}{\int \left\{ \frac{1}{2F} (\chi_1'^2 + \chi_2'^2 + \ell^2 (\chi_1^2 + \chi_2^2)) + \frac{1}{2} (\chi_2 - \chi_1)^2 \right\} dx} \quad (3.11)$$

It is trivial that $\alpha_i \equiv 0$ if $\ell = 0$ and ℓ is assumed to be positive. The sign of α_i is determined by the numerator in eq. (3.11), in which the first integral corresponds to the baroclinic interaction defined in the previous section and the last the barotropic interaction. The structures of the integrals are revealing some consequences of the interactions and are worth examining in detail here.

(1) Baroclinic Interaction

The contribution of this interaction depends upon the correlation between the vertical phase difference in the perturbation $(\Theta_2 - \Theta_1)$ and the vertical shear represented by $\cos kx$.

If, (a), $\Theta_2 - \Theta_1 = 0$ or π , the perturbation stream functions in eq. (3.7) are vertically in phase on the plane $x = \text{const.}$ if $\Theta_2 - \Theta_1 = 0$ or out of phase if $\Theta_2 - \Theta_1 = \pi$, which means that the perturbation is either pure barotropic or baroclinic. In either case there is no baroclinic interaction.

If, (b), $0 < \Theta_2 - \Theta_1 < \pi$ with $\cos kx < 0$ or $-\pi < \Theta_2 - \Theta_1 < 0$ with $\cos kx > 0$, the interaction yields a negative value in α_i and the perturbation is unstable baroclinically. It can be seen that

the common feature is that the lines of constant phase are tilted opposite to the vertical shear. This is the same characteristic vertical structure as found in the unstable perturbations in zonal currents (Bretherton 1966).

$$\text{If, (c), } -\pi < \textcircled{H}_2 - \textcircled{H}_1 < 0 \text{ with } \cos kx > 0 \text{ or}$$

$$0 < \textcircled{H}_2 - \textcircled{H}_1 < \pi \text{ with } \cos kx > 0,$$

the relation between the phase lines and the vertical shear is opposite to that in (b) and the corresponding perturbation is stable.

(2) Barotropic Interaction

This interaction is determined in each layer separately, hence the name barotropic interaction. As far as this interaction is concerned, what is important is the horizontal shear, not vertical shear.

From these classifications two important features emerge. Firstly, the baroclinic process is concentrated around the maximum vertical shear, while the barotropic process is concentrated around the maximum horizontal shear. Secondly, each process requires a unique relation between the perturbation and the unperturbed flows. Generally the two maxima do not coincide and an unstable perturbation in one interaction may not have a right phase to be unstable in the other interaction. Therefore it may be possible that one interaction transfers energy from the unperturbed to the perturbation flow, and the other does the reverse.

The balance between the two interactions varies with L/L_ρ as discussed and is expected to be very subtle around $\frac{L}{L_\rho} \sim 1$, because the vertical and horizontal shears are comparable.

IV. PERTURBATION ANALYSIS

IV-1 Solutions in Fourier Series

Having found some important characteristics of the stability, we are going to look at the stability criteria in terms of the parameters and the structures of growing perturbations in detail, by solving the perturbation equations in Fourier series.

The perturbation stream functions are decomposed into the Fourier Series in space, discrete in x .

$$\begin{pmatrix} \phi_1 \\ \phi_2 \end{pmatrix} = \text{Re} \sum_{-\infty}^{\infty} \begin{pmatrix} \xi_n \\ \zeta_n \end{pmatrix} e^{i(nkx + ly + \alpha t)} \quad (4.1)$$

where the amplitudes (ξ_n, ζ_n) and the frequency α are complex in general and n will be called mode number. This solution, periodic in x with the periodicity of the unperturbed flow, is probably not the most general solution: as in Floquet's theorem for Mathieu's equation, we expect the general solution to contain an additional $e^{i\nu kx}$ factor where $0 < \nu \leq 1$. But the solutions sought here, analagous to the Mathieu functions, are likely to be representative of the total set. Substituting the Fourier series into eq. (3.4a,b) and making use of the orthogonality of the series we obtain the following equations relating the amplitudes of three consecutive modes centered at n .

$$\frac{2\Delta}{P^2}\{-(n^2K+P+1)\xi_n+\zeta_n\}-2n\left(\frac{SK}{P}\right)^{\frac{1}{2}}\{-(n^2K+P-1-K)\xi_n+\zeta_n\}$$

(4.2a)

$$-\{(n-1)^2K+P-1-K\}\xi_{n-1}+\zeta_{n-1}-\{(n+1)^2K+P-1-K\}\xi_{n+1}+\zeta_{n+1} = 0$$

$$\frac{2\Delta}{P^2}\{-(n^2K+P+1)\zeta_n+\xi_n\}-2n\left(\frac{SK}{P}\right)^{\frac{1}{2}}\{-(n^2K+P-1-K)\zeta_n+\xi_n\}$$

(4.2b)

$$+\{(n-1)^2K+P-1-K\}\zeta_{n-1}-\xi_{n-1}+\{(n+1)^2K+P-1-K\}\zeta_{n+1}-\xi_{n+1} = 0$$

where $\Delta = \frac{\alpha}{UF^{\frac{1}{2}}}$, $K = \frac{k^2}{F}$, $P = \frac{\ell^2}{F}$ and $S = \frac{C^2}{U^2}$. These nondimensional parameters can be better understood in terms of dimensional quantities, bracketed whenever necessary not to be confused with the nondimensional.

$\Delta = \frac{[\alpha]}{[U/L_\rho]}$: frequency and/or growth rate of perturbation normalized by $[U/L_\rho]$.

$S = \frac{[C]^2}{[U]^2}$: square of the ratio between the phase speed of the unperturbed and the maximum particle speed.

$K = \left[\frac{L}{L_\rho}\right]^2$: square of the ratio between the radius of deformation and the scale of the unperturbed field $L = 1/k$.

$P = \left[\frac{L}{L_p}\right]^2$: square of the ratio between the radius of deformation and the meridional scale of the perturbation $L_p = 1/\ell$.

Any length scale here is meant to be equal to the corresponding wavelength divided by 2π .

A set of particular combinations of amplitudes (ξ_n, ζ_n) is very useful in the analysis.

$$\sigma_n^+ = \xi_n + \zeta_n : \text{ barotropic part at } n.$$

$$\sigma_n^- = \xi_n - \zeta_n : \text{ baroclinic part at } n.$$

The definitions of (σ_n^+, σ_n^-) are clear in the inverse transformation as

$$\xi_n = \frac{1}{2}(\sigma_n^+ + \sigma_n^-), \quad (4.3a)$$

$$\zeta_n = \frac{1}{2}(\sigma_n^+ - \sigma_n^-). \quad (4.3b)$$

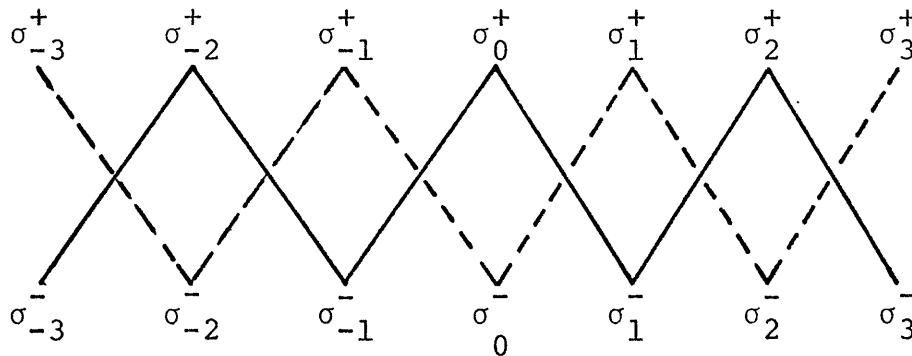
The sum of eqs. (4.2a,b) and the difference between them yield equations in terms of the barotropic and baroclinic parts as follows:

$$\begin{aligned} & \{2\Delta(n^2K+P) - 2(SK)^{\frac{1}{2}}n(n^2K+P-2-K)\}\sigma_n^+ \\ & + \{(n-1)^2K+P-K\}P^{\frac{1}{2}}\sigma_{n-1}^- + \{(n+1)^2K+P-K\}P^{\frac{1}{2}}\sigma_{n+1}^- = 0 \end{aligned} \quad (4.4a)$$

$$\{2\Delta(n^2K+P+2)-2(SK)^{\frac{1}{2}}n(n^2K+P-K)\}\sigma_n^- \quad (4.4b)$$

$$+\{(n-1)^2K+P-2-K\}P^{\frac{1}{2}}\sigma_{n-1}^+ + \{(n+1)^2K+P-2-K\}P^{\frac{1}{2}}\sigma_{n+1}^+ = 0.$$

These equations form homogeneous equations of infinite number, imposing an eigenvalue problem for Δ with eigenvectors (σ_n^+, σ_n^-) . It is very interesting to find selective coupling among the modes in their interactions. The barotropic part of mode n interacts with the baroclinic parts of neighboring modes $(n-1)$ and $(n+1)$ exclusively in eq. (4.4a). On the other hand, the baroclinic part of mode n interacts only with the barotropic parts of modes $(n-1)$ and $(n+1)$ in eq. (4.4b). The consequence of this selection is that the entire nonlinear interaction is divided into two chains of interaction, which are completely independent of each other as shown below.



The interactions connected by solid and dotted lines

are called Branch I and Branch II, respectively.

Because there is no overlap between two branches, the homogeneous equations from eqs. (4.3a,b) divide into two subsets of infinite equations, yielding two eigenvalue problems. In tensor form they are

$$A_{ij} X_j = -\Delta_I X_j \quad \text{for Branch I} \quad (4.5a)$$

$$B_{ij} Y_j = -\Delta_{II} Y_j \quad \text{for Branch II} \quad (4.5b)$$

where x_j and Y_j are

$$X_j = \begin{pmatrix} \cdot \\ \cdot \\ \sigma_{-2}^+ \\ - \\ \sigma_{-1}^- \\ \sigma_0^+ \\ - \\ \sigma_1^- \\ \sigma_2^+ \\ \cdot \\ \cdot \end{pmatrix} \quad \text{and } Y_j = \begin{pmatrix} \cdot \\ \cdot \\ \sigma_{-2}^- \\ \sigma_{-1}^+ \\ - \\ \sigma_0^- \\ \sigma_1^+ \\ \sigma_2^- \\ \cdot \\ \cdot \end{pmatrix}$$

The corresponding matrices A_{ij} and B_{ij} are made of the coefficients in eqs. (4.4a,b), shown on the following pages.

$$A_{ij} = \left(\begin{array}{cccccc}
& & & \vdots & & \\
2(SK)^{\frac{1}{2}} \frac{(3K+P-2)}{(4K+P)} & \frac{P^{3/2}}{2(4K+P)} & 0 & 0 & 0 & \\
\frac{(3K+P-2)P^{\frac{1}{2}}}{2(K+P+2)} & \boxed{(SK)^{\frac{1}{2}} \frac{P}{K+P+2}} & \boxed{\frac{(P-2-K)P^{\frac{1}{2}}}{2(K+P+2)}} & 0 & 0 & \\
\cdots 0 & \frac{1}{2}P^{\frac{1}{2}} & 0 & \frac{1}{2}P^{\frac{1}{2}} & 0 \cdots & \\
0 & 0 & \frac{(P-2-K)P^{\frac{1}{2}}}{2(K+P+2)} & -(SK)^{\frac{1}{2}} \frac{P}{K+P+2} & \frac{(3K+P-2)P^{\frac{1}{2}}}{2(K+P+2)} & \\
0 & 0 & 0 & \frac{P^{3/2}}{2(4K+P)} & -2(SK)^{\frac{1}{2}} \frac{(3K+P-2)}{(4K+P)} & \\
& & \vdots & & & \\
& & & \vdots & &
\end{array} \right) \tag{4.6a}$$

$B_{ij} =$

$$\begin{pmatrix}
 2(SK)^{\frac{1}{2}} \frac{(3K+P)}{(4K+P+2)} \frac{(P-2)P^{\frac{1}{2}}}{2(4K+P+2)} & 0 & 0 & 0 & 0 \\
 0 & \frac{(3K+P)P^{\frac{1}{2}}}{2(K+P)} & (SK)^{\frac{1}{2}} \frac{P-2}{(K+P)} \frac{(P-K)P^{\frac{1}{2}}}{2(K+P)} & 0 & 0 \\
 0 & 0 & \frac{(P-2)P^{\frac{1}{2}}}{2(P+2)} & 0 & \frac{(P-2)P^{\frac{1}{2}}}{2(P+2)} & 0 \\
 0 & 0 & 0 & \frac{(P-K)P^{\frac{1}{2}}}{2(K+P)} & -(SK)^{\frac{1}{2}} \frac{P-2}{(K+P)} & \frac{(3K+P)P^{\frac{1}{2}}}{2(K+P)} \\
 0 & 0 & 0 & 0 & \frac{(P-2)P^{\frac{1}{2}}}{2(4K+P+2)} & -2(SK)^{\frac{1}{2}} \frac{(3K+P)}{(4K+P+2)}
 \end{pmatrix}$$

(4.6b)

It is worthwhile to explore the possible solutions. For given values of parameters S , K and P the eigenvalues Δ_I and Δ_{II} will be different in general. Hence the eigenvector of Branch II corresponding to the eigenvalue of Branch I will be trivial and vice versa. However even the trivial solution in σ_n^+ or σ_n^- is necessary to determine (ξ_n, ζ_n) in eqs. (4.3a,b). Suppose Branch II has a trivial solution, that is

$$\sigma_0^- = \sigma_1^+ = \sigma_2^- = \sigma_3^+ = \dots = 0,$$

equivalently

$$\xi_0 = \zeta_0, \quad \xi_{\pm 1} = -\zeta_{\pm 1}, \quad \xi_{\pm 2} = \zeta_{\pm 2}, \quad \dots$$

Therefore the components with even mode number are barotropic and those with odd are baroclinic. This structure will be opposite for a trivial solution of Branch I.

Now let us examine the existence of a convergent series as a solution. For a sufficiently large $n > 0$ a possible balance in eq. (4.4a) should be either

$$(a) \left| \frac{\sigma_n^+}{\sigma_{n-1}^-} \right| \sim \frac{1}{2(SK)^{\frac{1}{2}n}} \quad \text{or} \quad (b) \left| \frac{\sigma_{n+1}^-}{\sigma_n^+} \right| \sim 2(SK)^{\frac{1}{2}n}, \quad \text{and in}$$

$$\text{eq. (4.4b) either} \quad (c) \left| \frac{\sigma_n^-}{\sigma_{n-1}^+} \right| \sim \frac{1}{2(SK)^{\frac{1}{2}n}} \quad \text{or} \quad (d) \left| \frac{\sigma_{n+1}^+}{\sigma_n^-} \right| \sim$$

$$2(SK)^{\frac{1}{2}n} \quad \text{with} \quad n > K^{-\frac{1}{2}}.$$

If an eigenvector satisfies (a) and (c), then the series converges absolutely by a ratio test (Whittaker and Watson, 1965). Otherwise the series may not converge.

IV-2 Characteristics in 3-mode truncation

It is assumed that the perturbation is dominated by three modes $n = (-1, 0, 1)$ neglecting the rest of modes compared with these three and the results from this truncation will be carefully re-examined in higher-mode analyses. In this approximation the matrices A_{ij} and B_{ij} become finite 3×3 square matrices, enclosed by a dotted line in eqs. (4.6a,b), and the eigenvalues are found easily by solving the determinants from eqs. (4.5a,b).

$$\Delta_I^2 = S \frac{KP^2}{(K+P+2)^2} + \frac{P}{2} \frac{\{P-(K+2)\}}{\{P+(K+2)\}} \text{ for Branch I} \quad (4.7a)$$

$$\Delta_{II}^2 = S \frac{K(P-2)^2}{(P+K)^2} + \frac{P(P-K)(P-2)}{2(P+K)(P+2)} \text{ for Branch II} \quad (4.7b)$$

IV-2-1 Marginal stability curves

It will be interesting to find out the regimes of different stability characteristics. Figure 4.1 shows two families of marginal stability curves in $(\frac{L}{L_\rho}, \frac{L_P}{L_\rho})$ for different values of U/C . Note that L_P is the meridional scale of the growing instability; the zonal scale is fixed by that of the unperturbed flow which varies over the

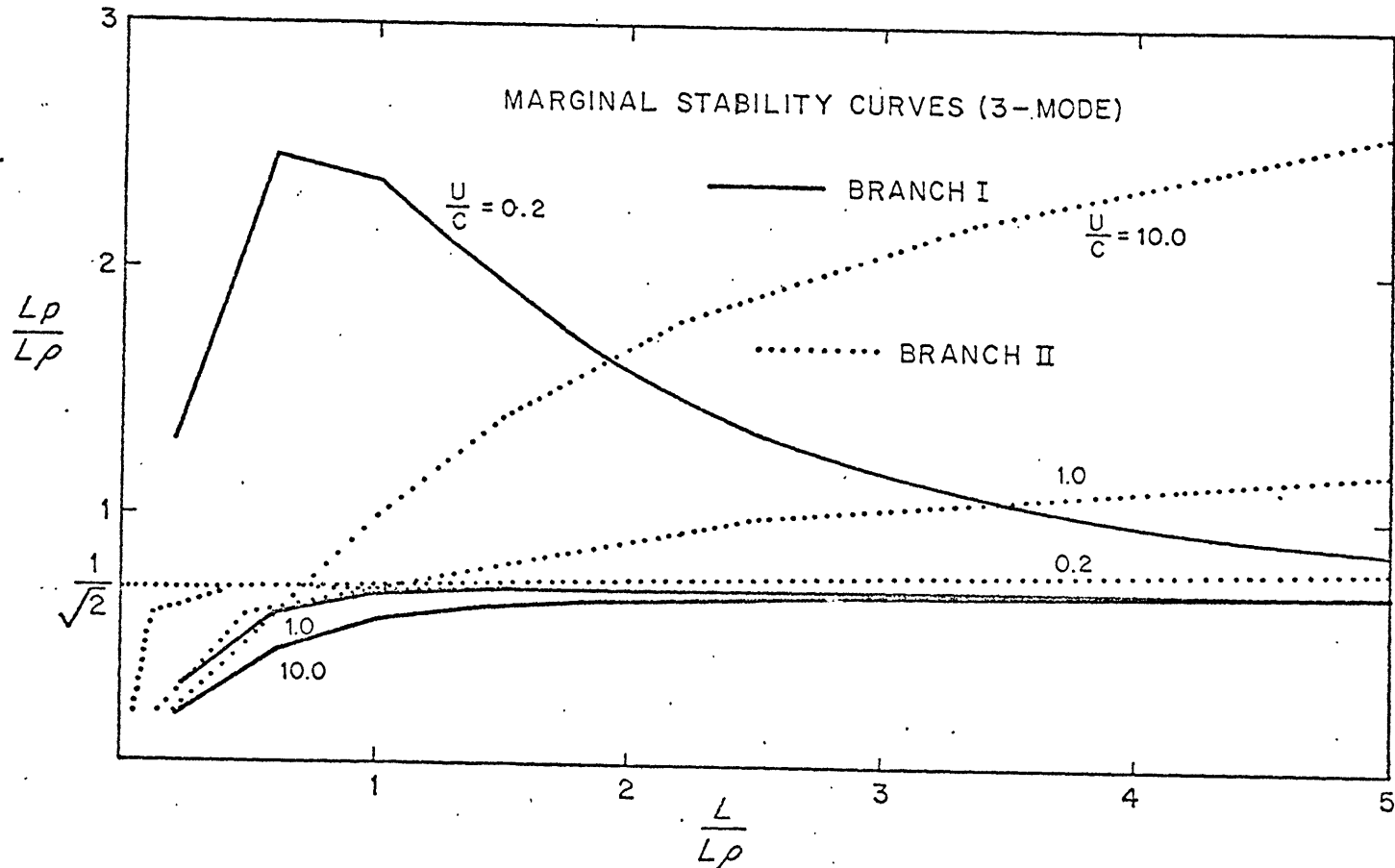


Fig. 4.1 Branch I: The region above marginal stability curves is unstable and one below the curves is stable. Note short wavelength limit of unstable perturbations in the meridional scale of perturbation for large scale basic flow, $L > L_p$. There exist unstable modes irrespective of the current strength. Branch II: The unstable region is both upper and lower bounded in L_p/L_rho . As in Branch I, unstable perturbation exists for $U < C$.

entire range $(0, \infty)$.

(1) Branch I: The curve is defined by

$$P + SK(S^2K^2 + (K + 2)^2)^{\frac{1}{2}} = 0,$$

which divides the parameter space into unstable and stable regions. For $\frac{L}{L_\rho} < \frac{\sqrt{2}}{2}$ the value of L_p/L_ρ increases monotonically with L/L_ρ . Near the origin L_p is proportional to L by $(S + \sqrt{S^2 + 1})^{\frac{1}{2}}$ and the presence of L_ρ is not relevant. For $\frac{L}{L_\rho} > \frac{1}{\sqrt{2}}$, L_p/L_ρ approaches to $\frac{\sqrt{2}}{2}$ asymptotically either from above if $\frac{U}{C} < 1$ or from below if $\frac{U}{C} \geq 1$. In any case the regime above the marginal stability curve is unstable and one below the curve is stable. The unstable regime widens towards smaller values of L_p/L_ρ as U/C increases. The short wavelength limit of unstable perturbation for $\frac{L}{L_\rho} > 1$ is very similar to the usual characteristics of the pure baroclinic instability in a two-layer model (Bretherton, 1966).

It is most important to note that there are always some unstable perturbations for any current U/C and any unperturbed scale L/L_ρ . Even a weak current with $\frac{U}{C} < 1$ is unstable with respect to some infinitesimal perturbations. This indicates that the beta-effect represented by C in eq. (3.2) may never be strong enough to stabilize the current in this study. With the parametrically increasing beta-effect the perturbation at certain scales no longer fall within the unstable regime. However, the perturbations with a sufficiently large scale are still unstable.

(2) Branch II: There are two equations defining the marginal stability curve of this branch;

$$P - 2 = 0,$$

$$P^3 + 2SKP^2 - K^2P - 8SK = 0.$$

The unstable regime is both upper and lower bounded in L_p/L_ρ with a band whose width increases with U/C . As in Branch I, unstable perturbation exists for $\frac{U}{C} < 1$.

IV-2-2 Growth rate for unstable perturbation

From eqs. (4.7a,b) it is found that the growth rate of Branch I is always larger than that of Branch II for given U/C and L/L_ρ . Therefore only the results of Branch I are presented here. For a weak current with $\frac{U}{C} = 0.2$ the contours of constant growth rate in $(\frac{L}{L_\rho}, \frac{L_p}{L_\rho})$ plane form two hills in Fig. 4.2a, one rising towards large $\frac{L}{L_\rho} > 1$ with L_p/L_ρ approaching to unity and the other continuously rising towards a smaller and smaller L_p/L_ρ as L/L_ρ decreases from unity. As a current becomes stronger as $\frac{U}{C} = 1.0$ and 1.8 in Fig. 4.2b and 4.2c, the hill at large L/L_ρ tends to disappear and the growth rate changes very little with L/L_ρ ; the maximum growth rate approaches 0.4 around $\frac{L_p}{L_\rho} = 1.2$. The restoring effect of β clearly acts to stabilize modes near the center of the figures, pushing the dominant instability toward small and large L/L_ρ ; with a strong β -effect the baroclinic and barotropic

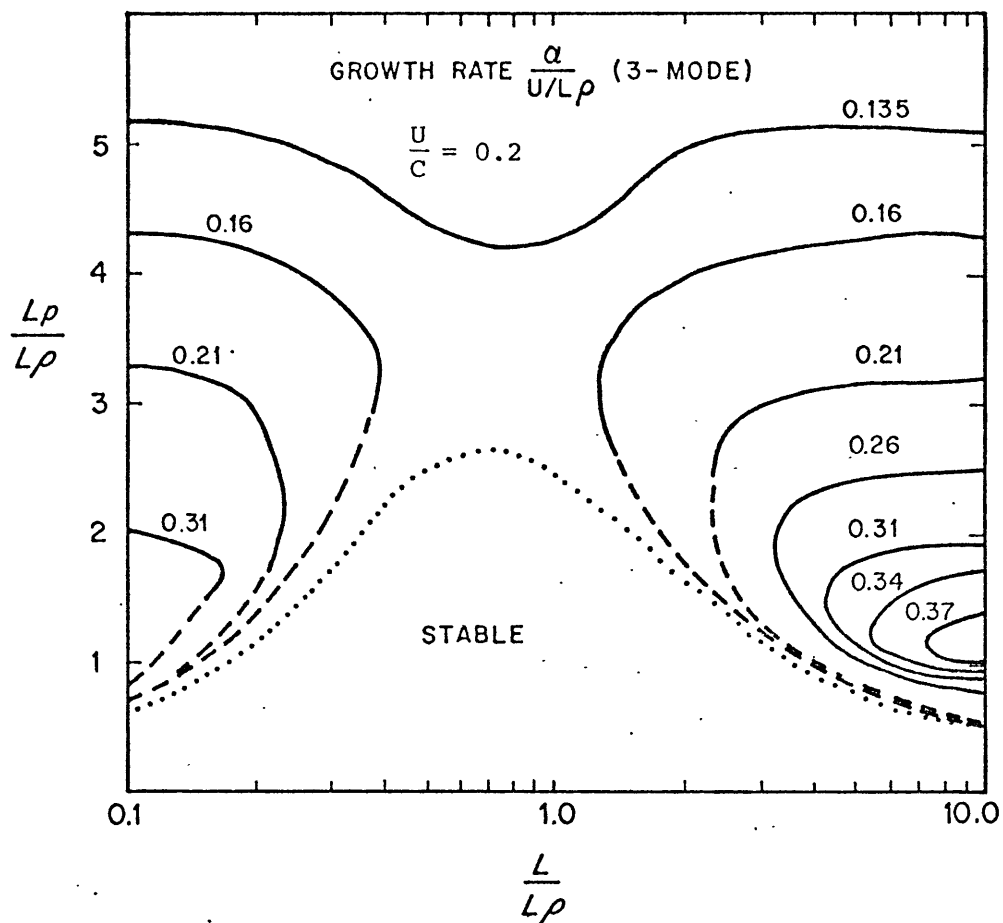


Fig. 4.2a The beta-effect(β) is relatively strong and the baroclinic and barotropic instability regimes are distinct for very large and small value of L/L_ρ , respectively. The restoring effect of β clearly acts to stabilize modes near the center of the figure.

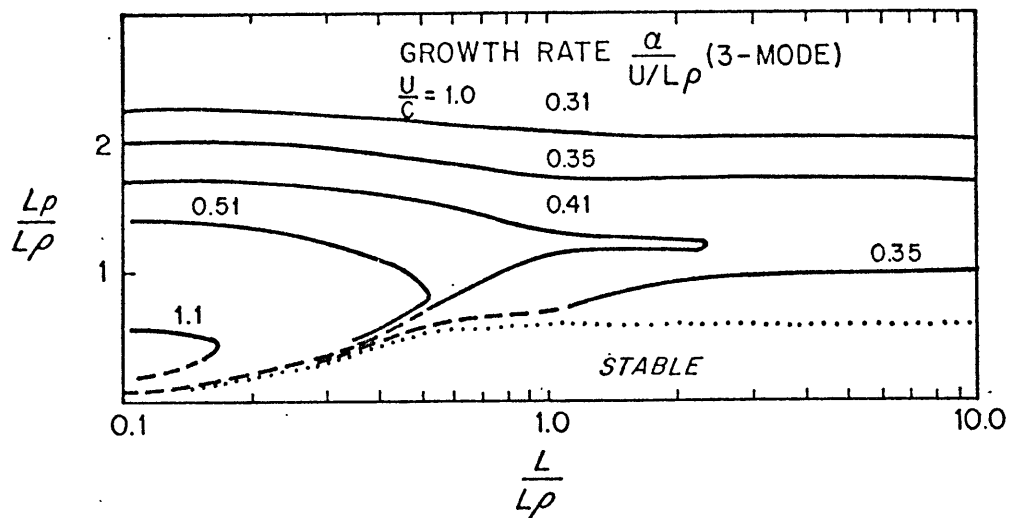


Fig. 4.2b As the basic flow strengthens (or with a weak beta-effect), the baroclinic and barotropic instability regimes merge into a smooth growth-surface. Short wavelength limit in the baroclinic regime is shown clearly,

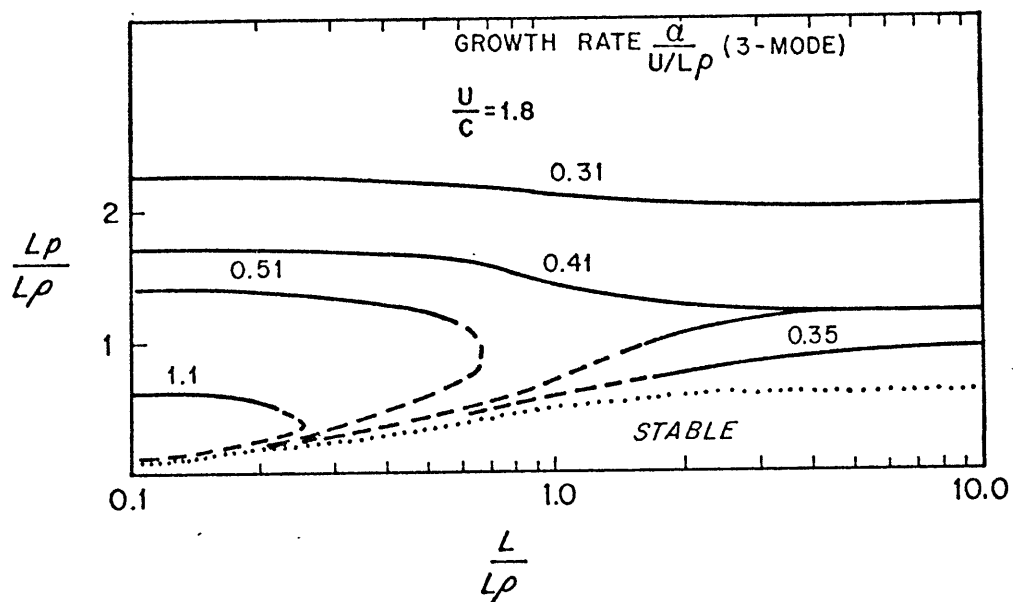


Fig. 4.2c Same as Fig. 4.2b except for a stronger current case. The meridional scale of the fastest growing perturbation is fixed at a scale slightly larger than the radius of deformation in the baroclinic regime and decreases in proportional to the zonal scale of the basic flow in the barotropic regime.

instability regimes are distinct, while with a weak β -effect, the regimes merge into a smooth growth-surface.

It should be recognized in Fig. (4.2b,c) that the presence of horizontal shear removes the short-wave cut-off of simple baroclinic instability, allowing a smooth transition to barotropic instability as one crosses $\frac{L}{L_\rho} = 1$.

In $\frac{L}{L_\rho} < 1$ the normalization of a growth rate by U/L_ρ is not appropriate, because the barotropic interaction is stronger than the baroclinic, and L_ρ is not a dynamically important scale. By renormalizing eq. (4.7a) it is possible to obtain

$$\left(\frac{\alpha}{U/L}\right)^2 = S \frac{1}{\left(\frac{K}{P}+1+\frac{2}{P}\right)^2} + \frac{1}{2\frac{K}{P}} \frac{1-\left(\frac{K}{P}+\frac{2}{P}\right)}{1+\frac{K}{P}+\frac{2}{P}}. \quad (4.8)$$

Figure 4.3 shows the renormalized growth rate $\frac{\alpha}{U/L}$ as a function of L_p/L in the range $\frac{L}{L_\rho} \leq 1$ and $0.1 < \frac{U}{C} < \infty$. The important results are recapitulated in Fig. 4.4, where the maximum growth rate is plotted. For a strong current with $\frac{U}{C} > 1$ the growth rate $\frac{\alpha}{U/L}$ depends very weakly on U/C ; the growth rate for $\frac{U}{C} = 2$ is slightly smaller than that for $\frac{U}{C} \rightarrow \infty$. However it decreases in proportion with U/C in the range $\frac{U}{C} < 1$. It is most remarkable to find that the renormalized growth rate increases rapidly with L/L_ρ . This phenomena may be explained in terms of available energies. As shown in section III-2 only the kinetic

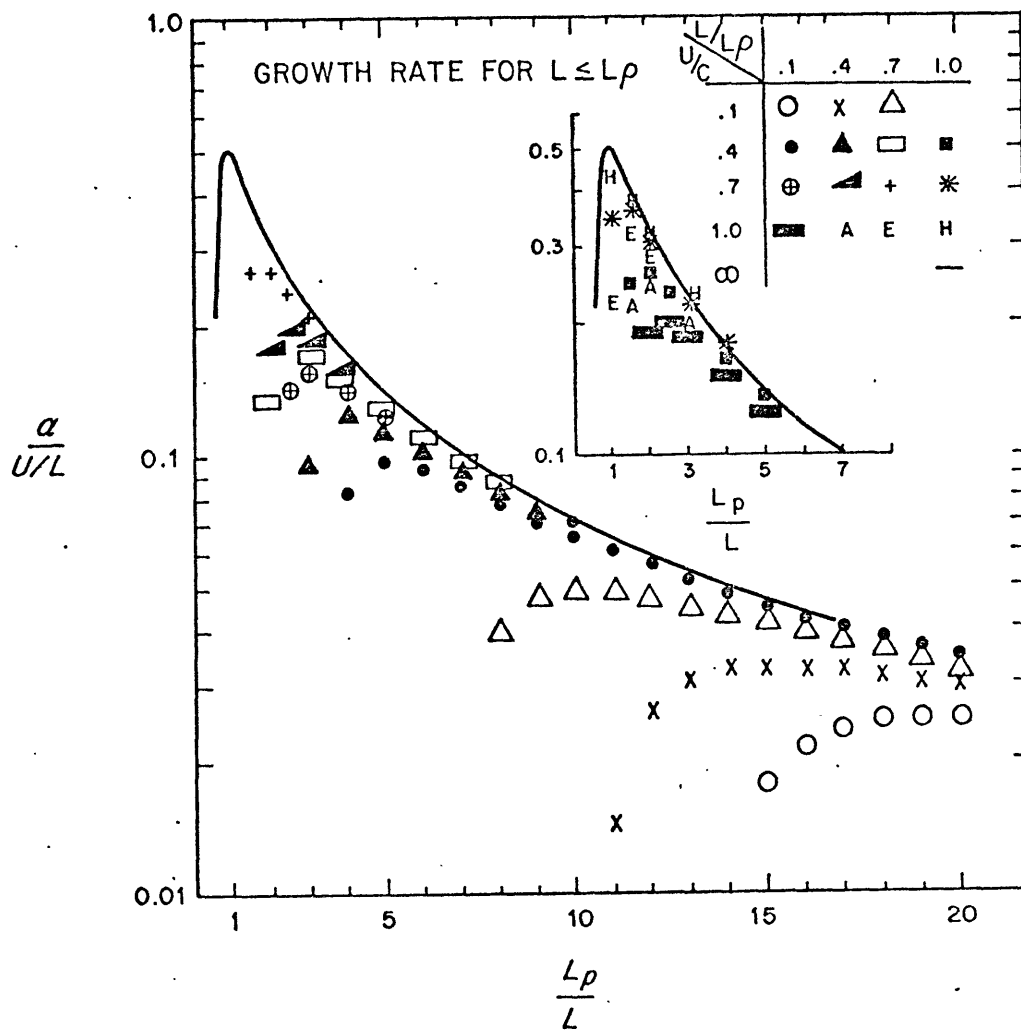


Fig. 4.3 Growth rate $\alpha L/U$, renormalized for the range $L \leq L_p$, where the barotropic interaction is important. The scale at the maximum growth rate is the same as that of the basic flow for $\frac{U}{C} = \infty$ and $\frac{L}{L_p} = 1$ and the basic flow generates a larger scale as its scale and strength decrease.

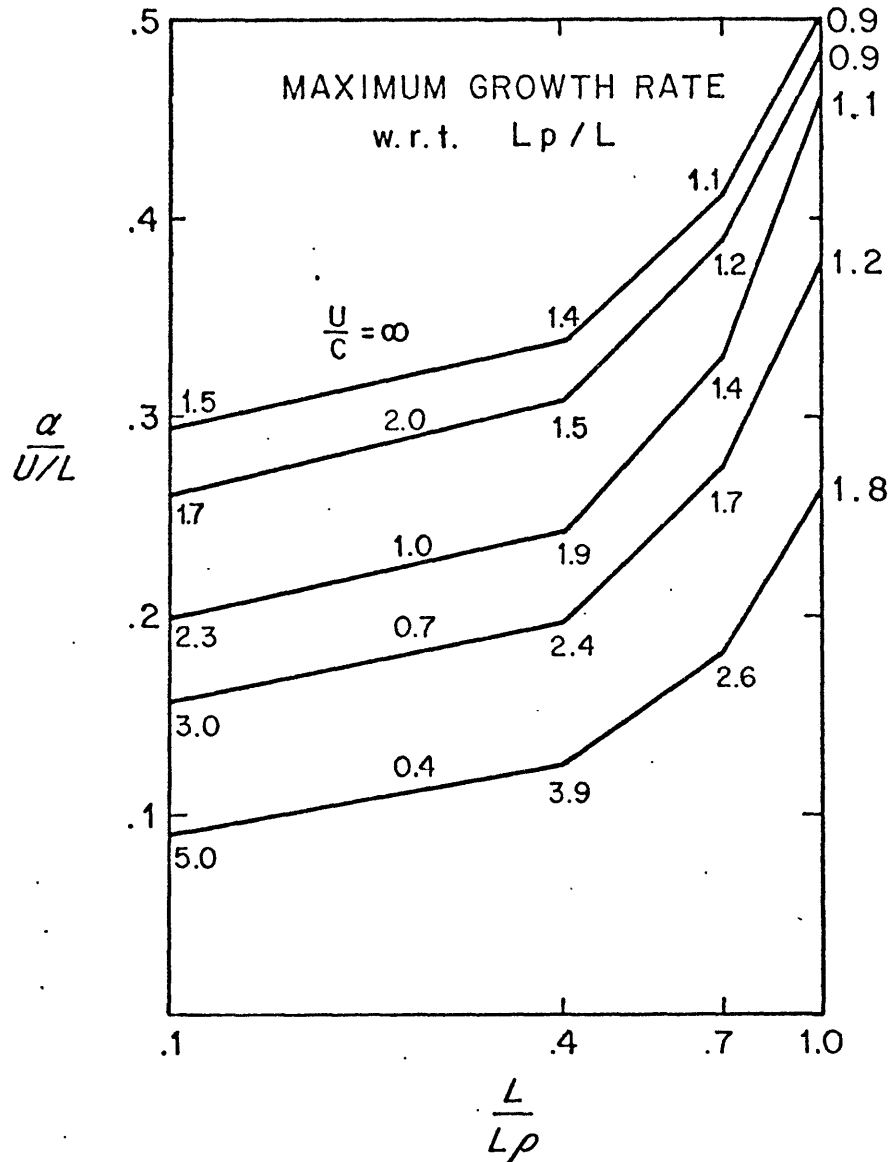


Fig. 4.4 Recapitulation of Fig. 4.3. Figures beside the curves are values of U/C and L_p/L at the maximum growth rate. Note an increase of the growth rate as $L \rightarrow L_p$, which is possible because of an increasing supply of potential energy.

energy is available for $\frac{L}{L_\rho} \ll 1$, but the potential energy is as available as the kinetic energy with $\frac{L}{L_\rho} \rightarrow 1$. Therefore this increase of the growth rate is most likely due to a positively accumulating effect of the barotropic and baroclinic interactions.

It is instructive to examine the growth rate for a very strong current. Taking $\frac{U}{C} \rightarrow \infty$ in eq. (4.7a) we find the maximum growth rate

$$[\alpha_i]_{\max} = (3 - 2\sqrt{2})^{\frac{1}{2}} [U] \left(\frac{1}{L_\rho^2} + \frac{1}{2L^2} \right)^{\frac{1}{2}}$$

with the scale

$$L_p = \left(\frac{\sqrt{2} + 1}{2 + \frac{L_\rho^2}{L^2}} \right)^{\frac{1}{2}} L_\rho.$$

In a limit $\frac{L}{L_\rho} \gg 1$

$$[\alpha_i]_{\max} \rightarrow 0.4142 \left[\frac{U}{L_\rho} \right] \text{ with } L_p \rightarrow 1.1 L_\rho, \quad (4.9)$$

while $\frac{L}{L_\rho} \ll 1$

$$[\alpha_i]_{\max} \rightarrow 0.29 \left[\frac{U}{L} \right] \text{ with } L_p \rightarrow 1.55 L. \quad (4.10)$$

It is interesting to see, here and in Fig. 4.2c and 4.3, that whereas any large-scale currents with $L \gg L_\rho$

generate the perturbation with the radius of deformation, small-scale currents generate the perturbation with scale larger than L .

The latter is reminiscent of the canonical result of two-dimensional turbulence, where it is proved that a spreading energy-wavenumber spectrum must move preferentially toward small wavenumber (in that the center-of-mass of the spectrum does so). It is enticing to imagine these instability calculations as models of the energy-transfer occurring in fields of geostrophic turbulence.

In these extreme limits it is expected physically that the growth rate be comparable with the values from simpler models. In fact, Simmons (1974, see Fig. 4) found the growth rate of 0.45 in the instability of a parabolic zonal current in a 10,000 km wide channel with the radius of deformation 1225 km, which may correspond to the case

$$\frac{L}{L_\rho} \gg 1.$$

The growth rate and the scale for $\frac{L}{L_\rho} \ll 1$ are identical with that which Gill (1974) found in the stability of barotropic Rossby waves. When $\frac{L}{L_\rho} \ll 1$ the two layers are dynamically independent (and the interface is effectively rigid), so that the barotropic instability problem is subsumed as a special case of the present theory.

IV-3 Higher-mode analyses

Although the results from the truncated series with three modes $n = (-1, 0, 1)$ look physically consistent in determining the stability criteria, the growth rate and the scale of the most unstable perturbation, it is necessary to investigate the stability characteristics using higher modes in order to check the reliability of the 3-mode results by estimating the possible truncation error. Therefore analyses have been carried out with five, seven and nine modes.

In each truncation first a polynomial in Δ is constructed by solving the determinant made from eqs. (4.5a,b), then the polynomial is solved for Δ analytically. By doing so, it is possible to get rid of an inevitable computation error in solving the determinant for Δ directly. The direct numerical computation of eigenvalue Δ from the determinant is found to be very unstable around the perturbation scale with the maximum growth rate.

In any case it is found that the growth rate from Branch I is always larger than that from Branch II as in the 3-mode truncation and the following analysis will be mostly concerned with the results from Branch I. The analysis in 5 modes does not show any significant departure from the 3-mode results and its results are included in the following section dealing with the 7-mode analysis.

IV-3-1 Analysis with 7 modes

For given values of parameters $(\frac{U}{C}, \frac{L}{L_\rho}, \frac{L_p}{L_\rho})$ there are seven eigenvalues and the current is classified to be unstable if any of them is complex with negative imaginary part. If there are more than one growth rate, the largest one is assigned as the growth rate. Figure 4.5 shows how the growth rate changes with L_p/L_ρ when $\frac{U}{C} = 1$. For $\frac{L}{L_\rho} > 1$, the behavior of the growth rate is the same as with the 3 modes, as far as the short wavelength limit of unstable perturbations and the maximum growth rate at $\frac{L_p}{L_\rho} \approx 1$ are concerned (compare Fig. 4.2b. Fig. 4.5 corresponds to vertical cuts in Fig. 4.2b).

For $\frac{L}{L_\rho} < 1$ the renormalized growth rate $\frac{\alpha}{U/L}$ has the maximum at a certain scale, L_p/L shown in the following table:

$\frac{L}{L_\rho} \backslash \frac{U}{C}$	0.5	1.0	2.5	10.0
.4	3.3(3.2)	1.75(1.9)	2.5(1.4)	1.75(1.4)
.7	2.1(2.2)	1.4(1.4)	1.4(1.2)	1.0(1.1)
1.0	1.5(1.5)	1.0(1.1)	1.0(1.0)	1.0(1.0)

Table: The perturbation scale normalized by the unperturbed scale, L_p/L , at the maximum growth rate. For

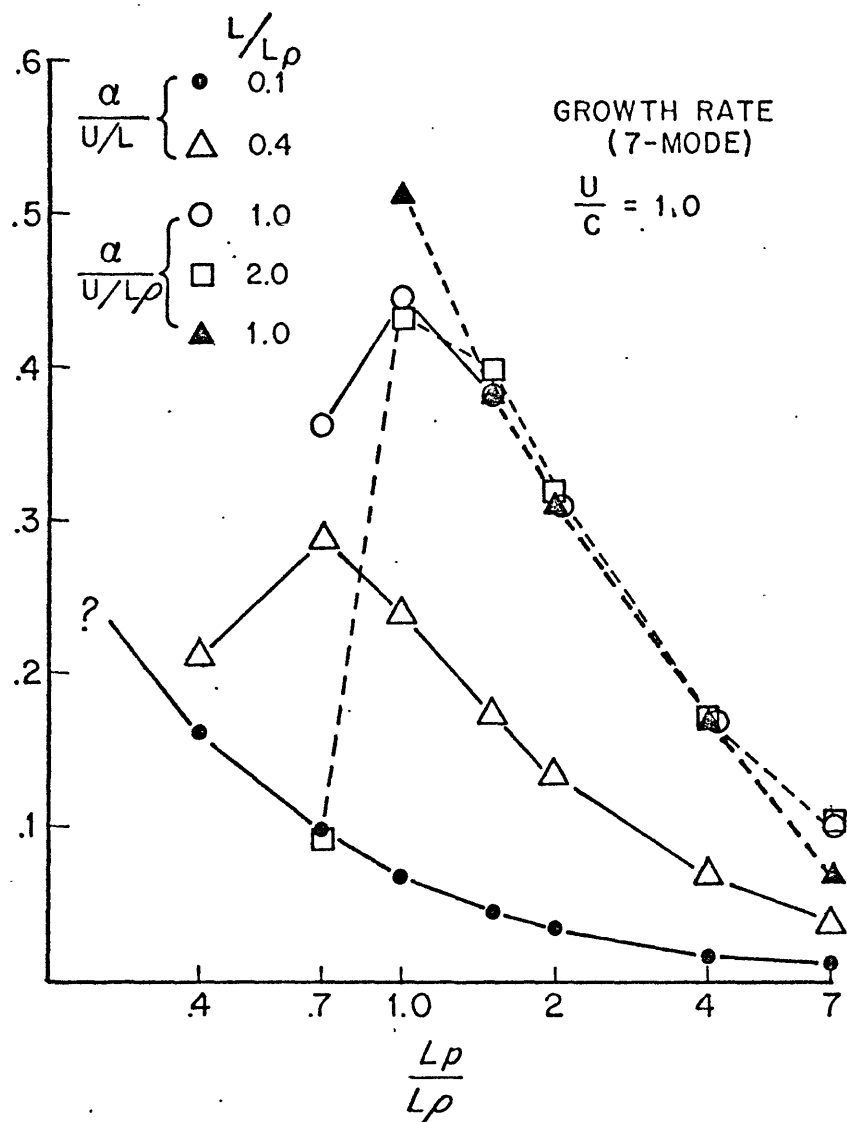


Fig. 4.5 These curves correspond to vertical cuts in Fig. 4.2b (3-mode). Growth rate shows basically the same behavior as found from the 3-mode analysis; short wavelength limit and maximum growth rate at $L_p \approx L_p$ in baroclinically controlled flows, and generation of larger scale in a barotropically controlled flow.

comparison the scales predicted from the 3-mode truncation are also presented in parentheses.

The most unstable scale is determined by comparing growth rates calculated for discrete values of $\frac{L_p}{L}$ so that there may be some uncertainty in pinpointing the scale and the growth rate. Nevertheless it is quite clear that the 7-mode results are over all in very good agreement with the 3-mode. It is very significant that the nonlinear interactions generate the perturbation with a scale larger than the unperturbed one for $L < L_\rho$ and the ratio between the two scales enlarges as $\frac{L}{L_\rho}$ decreases.

Figure 4.6 shows the variation of the maximum growth rate with respect to the perturbation scale as a function of $\frac{L}{L_\rho}$. In the range $\frac{L}{L_\rho} < 1$, the behavior is strikingly similar to the 3-mode variation (see Fig. 4.2b and 4.4); the series converges quickly in this range as shown in a later section. The extremum in the growth rate at $\frac{U}{C} = 1$, is not satisfactorily understood. Compared with the 3-mode analysis in Fig. 4.4, the 7-mode analysis shows about 15% increase in the growth rate.

In the range $\frac{L}{L_\rho} \geq 1$ there is very little change in the most unstable scale, but greater departure in the growth rate from the 3-mode results exists. The growth rate $\frac{\alpha}{U/L_\rho}$ increases continuously with L/L_ρ and appears

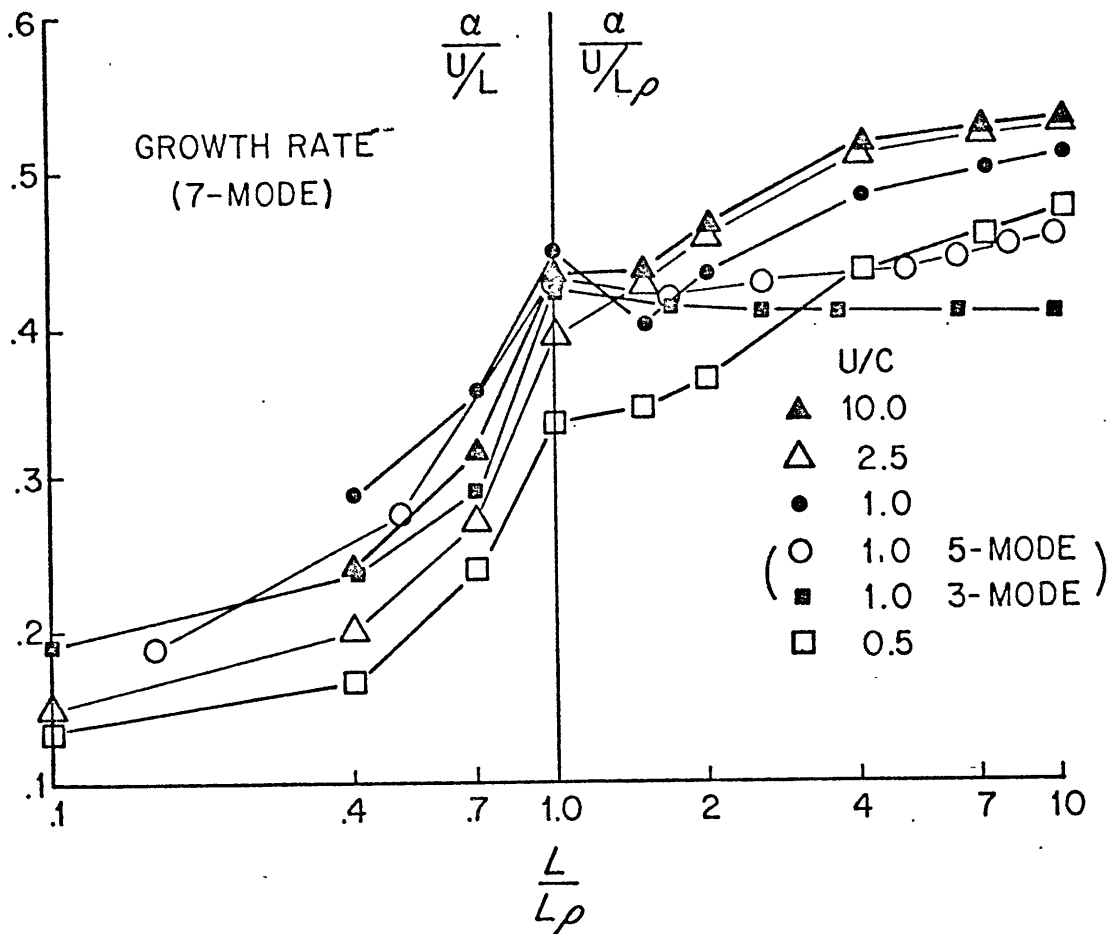


Fig. 4.6 For region $L < L_\rho$ this figure is very similar to Fig. 4.4 from the 3-mode analysis, indicating truncation errors are small. For $L > L_\rho$, a slight decrease of normalized growth rate as $L \rightarrow L_\rho$ from above is notable. This may be due to a feedback of energy into the basic wave via the interaction of Reynold stresses with the mean horizontal shear.

to approach an extreme value. A similar tendency has been found by Simmons (1974) from the stability analysis of a parabolic zonal current, which is reproduced in Fig. 4.7. In both cases the introduction of a weak horizontal shear (non-zero δ in Simmons' case, $\frac{L}{L_\rho} \gtrsim 1$ in our case), into the baroclinic current reduces the growth rate. The growth rate for the widest channel in Fig. 4.7 is 0.45 and just the same value is predicted in this study for a corresponding case with $\frac{U}{C} \approx 1$ and $\frac{L}{L_\rho} \approx 2.6$, the channel width being approximated as a half wavelength. However, the characteristics of the two models become widely different as L/L_ρ approaches unity and decreases further: Simmons' current is stable, while the meridional current in this study is still unstable. The horizontal structure in this study is closer to another zonal current from Simmons (1974), which is made of two sinusoidally varying currents (see eq. 5.1, Simmons) and found to be also unstable in a narrower channel.

To examine truncation error, the growth rates from the 3-mode and 5-mode analyses are plotted together in Fig. 4.6 for $\frac{U}{C} = 1$, which represents the rest as far as the comparison of the growth rate is concerned. There is no sign that the growth rate increases with L/L_ρ from the 3-mode analysis; the truncation error depends upon $\frac{L}{L_\rho}$. The error reaches about 20% at $\frac{L}{L_\rho} = 10$ based upon the

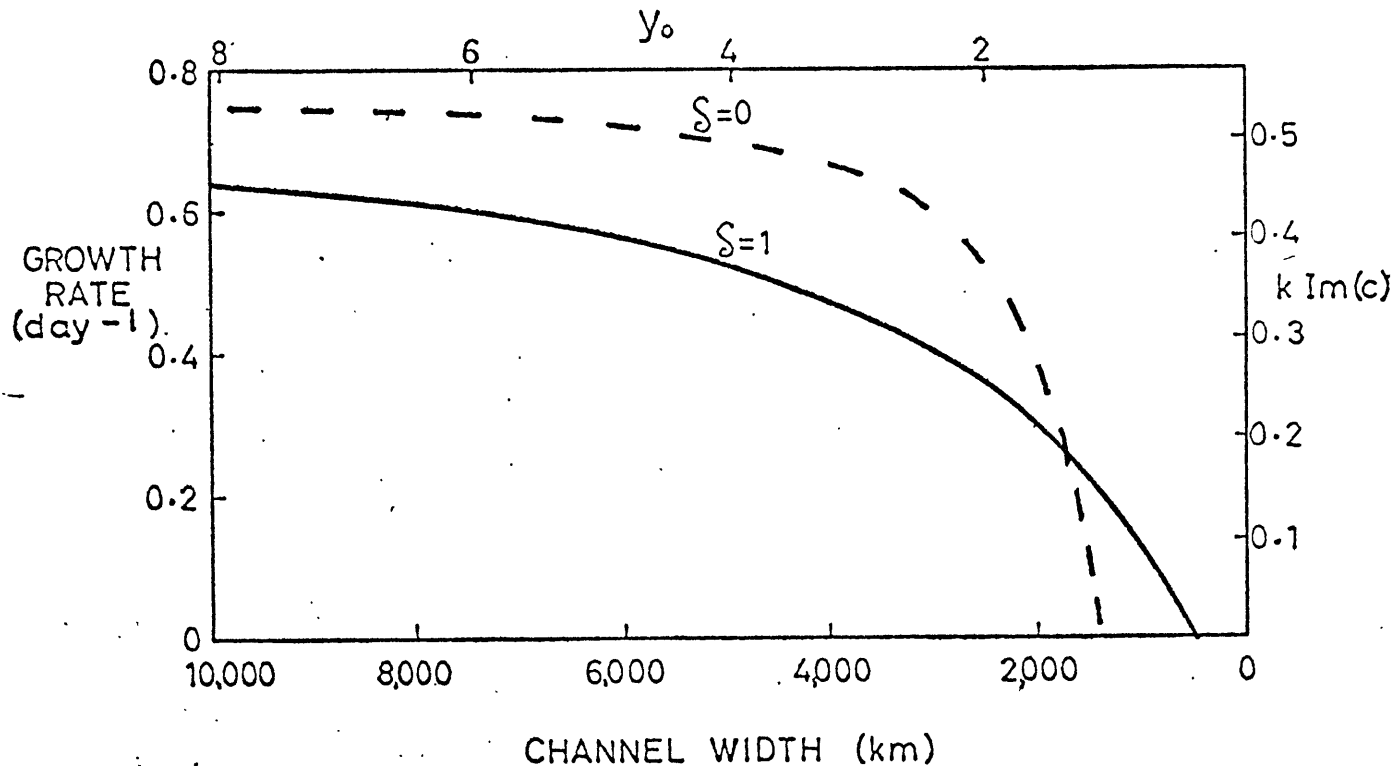


Fig. 4.7 From Simmons(1974). The dependence of maximum growth rate on channel width for a steady, zonal current with profile $u = 1 - 4\delta\left(\frac{y}{y_0} - \frac{1}{2}\right)^2$, where meridional walls are at $y = 0, y_0$. Lower layer is at rest initially and the radius of deformation is 1,225 km. Note a reduction of growth rate due to a non-uniformity ($\delta \neq 0$) compared with the case $\delta = 0$. As the channel becomes narrower (a horizontal shear increases effectively), the growth rate decreases further, meanwhile the horizontal shear is intensified.

7-mode growth rate. The 5-mode growth rate differs from the 7-mode one, but in fact a calculation with 9 modes shows very little further change. The growth rate from the 9-mode analysis is 0.5125 at $\frac{L}{L_\rho} = 10$, compared with 0.5114 from the 7-mode when $\frac{U}{C} = 1$ and 0.5428 compared with 0.5304 when $\frac{U}{C} = 5$. At this stage it was decided that the 7-mode analysis is accurate enough within the range of parameters considered here.

Figure 4.8a shows the distribution of relative magnitudes of amplitude at the maximum growth rate. Clearly the series converge very fast for small value of U/C and L/L_ρ and slower and slower as U/C and L/L_ρ become large. In four cases $(\frac{U}{C}, \frac{L}{L_\rho}) = (1.0, 1.5), (1.0, 1.), (2.5, 2)$ and $(10.0, 10.0)$ the amplitudes at $n = \pm 2$ are larger than those at $n = \pm 1$. This is believed to be some manifestation of the structure of the unstable perturbation when $\frac{L}{L_\rho} > 1$, which has larger barotropic components than baroclinic, recalling that all the even modes are barotropic in Branch I. The same kind of perturbation structures have been found in Branch II, now odd modes being barotropic, whose examples are shown in Fig. 4.8b. In all three cases the largest amplitudes are at $n = \pm 1$ and the amplitude at $n = 0$ takes the next. In one of them $n = \pm 3$ have larger amplitudes than $n = \pm 2$. It is speculated that this preferential partition, particularly

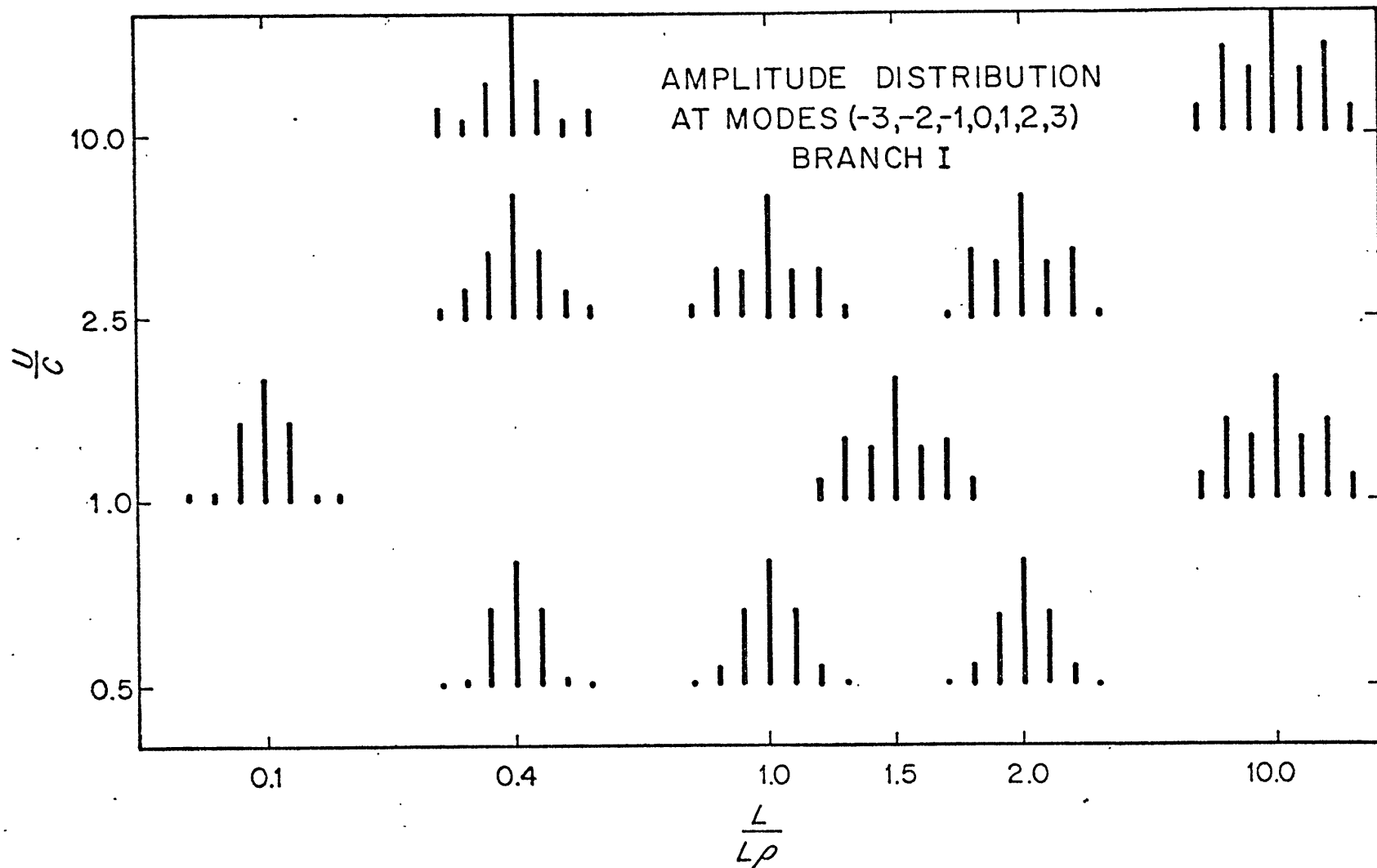


Fig. 4.8a Fast convergence of series for $U < C$ and $L < L_\rho$ shows why the results from the 3-mode analysis are so close ρ to those from the 7-mode one. Convergence becomes slower as L increases from L_ρ and U from C . However, a calculation with 9 modes shows ρ very little further change in the growth rate.

AMPLITUDE DISTRIBUTION
AT MODES (-3,-2,-1,0,1,2,3)
BRANCH II

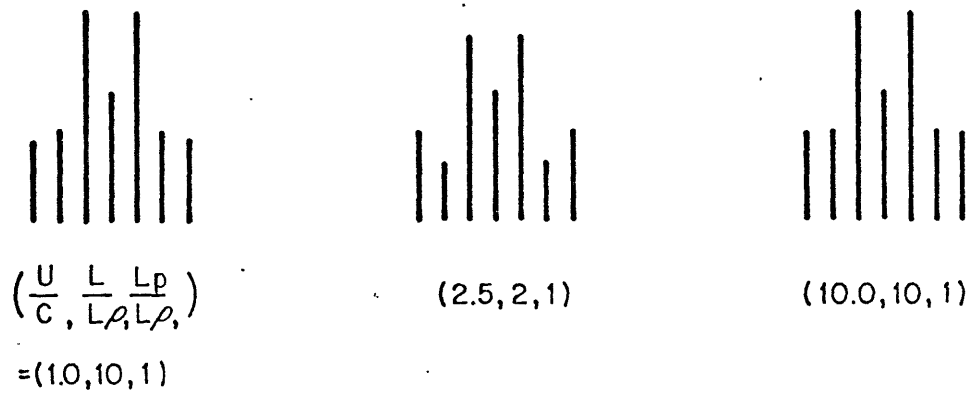


Fig. 4.8b A tendency to generate a strong barotropic component of growing perturbation can be more easily seen in Branch II. Odd modes, $n = \pm 1, \pm 3, \dots$, are barotropic vertically.

at $n = 0$, which represents a pure zonal component in the perturbation, may cause the growth rate of Branch II smaller than that of Branch I.

The fastest growing perturbation has a unique meridional scale and is comprised of four zonal scales in the 7-mode analysis; it is natural, therefore, to plot the perturbation kinetic energy as a developing (scalar) wavenumber spectrum, Fig. 4.9. Irrespective of U/C and L/L_ρ , mode $n = 0$, the lowest wavenumber representing the zonal component of the perturbation, contributes the highest peak, as suggested in Fig. 4.8a. Therefore the meridional scale serves as a good measure of the perturbation scale. The spectrum is relatively wide-spread for small L/L_ρ and declines toward high wavenumber very quickly as L/L_ρ increases from unity. The pattern of major energy transfer, to a larger scale if $L < L_\rho$ and to a smaller scale (the radius of deformation) if $L > L_\rho$, is basically the same as discussed already regarding Fig. 4.3 and 4.5. Thus we are able to produce with a single instability mode a quasi-continuous Fourier wavenumber spectrum. This contrasts the recent geostrophic turbulent theories, which describe observed sloping spectra as being a part of a turbulent cascade.

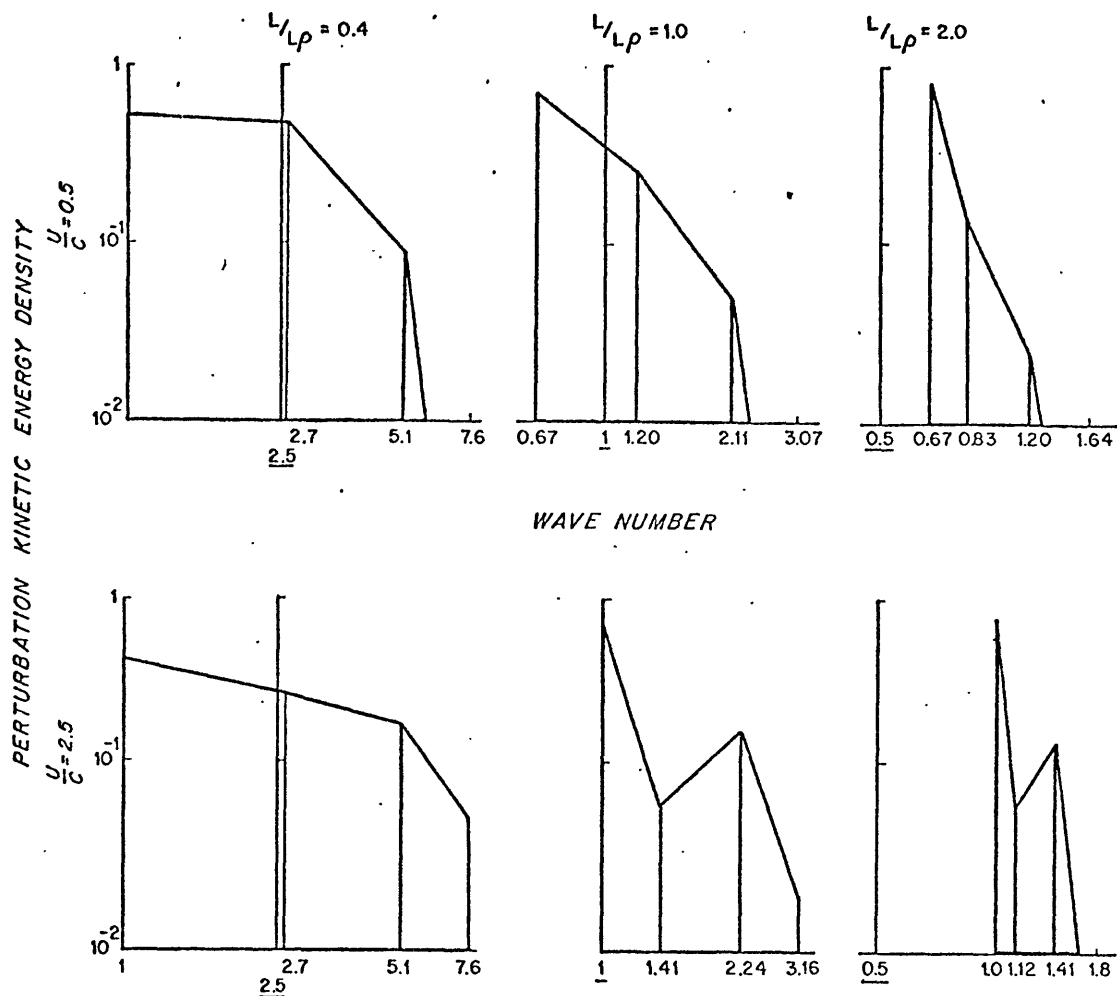


Fig. 4.9 Relative perturbation kinetic energy plotted as a scalar wavenumber spectrum. Wavenumber unity corresponds to the deformation radius and the wavenumber of the basic wave is underlined. Irrespective of U/C and L/L_p , mode $n = 0$, the lowest wavenumber representing the zonal component of the perturbation, contributes the highest peak. It is interesting to produce a quasi-continuous spectrum from a single mode.

IV-3-2 Baroclinic interaction vs. barotropic interaction

The growing perturbation draws its energy from the unperturbed field and two energy transfer processes called barotropic and baroclinic interactions are discussed in section III-2. Since these interactions occur at the same time and each interaction requires a unique relation between the perturbation configuration and the unperturbed field, the exact contribution of each process in the instability has been left to be answered until the structure of the perturbation is found in detail. From eq. (3.6) it is possible to derive the interactions in terms of eigenvectors.

$$\begin{aligned} \text{Baroclinic Interaction} = 2\pi k U F \{ & A_0 A_1 \sin(\theta_1 - \theta_0) - A_1 A_2 \\ & \sin(\theta_2 - \theta_1) + A_2 A_3 \sin(\theta_3 - \theta_2) - A_3 A_4 \sin(\theta_4 - \theta_3) + \dots \} \end{aligned} \quad (4.11)$$

$$\begin{aligned} \text{Barotropic Interaction} = -\pi k \ell U \{ & A_0 A_1 \sin(\theta_1 - \theta_0) + 3A_1 A_2 \\ & \sin(\theta_2 - \theta_1) + 5A_2 A_3 \sin(\theta_3 - \theta_2) + \dots \} \end{aligned} \quad (4.12)$$

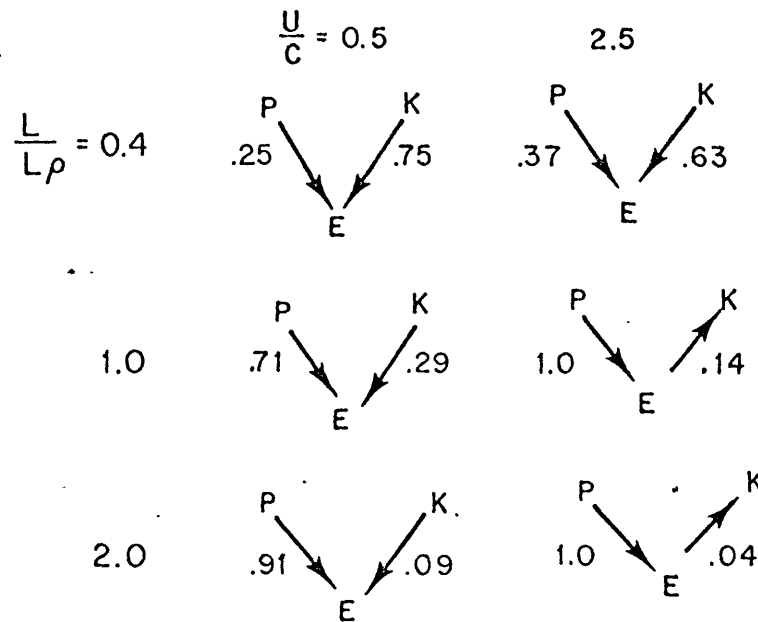
$$\text{where } A_q = |\sigma_{2q}^+|, \quad A_{2q-1} = |\sigma_{2q-1}^-| \quad (q = 1, 2 \dots)$$

$$\theta_{2q} = \text{phase}(\sigma_{2q}^+), \quad \theta_{2q-1} = \text{phase}(\sigma_{2q-1}^-)$$

with the reference $A_0 = 1$ and $\theta_0 = 0$.

In the extreme limits when $\frac{L}{L_\rho} \gg 1$ or $\frac{L}{L_\rho} \ll 1$, the energy transfer is dominated by the baroclinic or barotropic interaction respectively. The instability near $\frac{L}{L_\rho} = 1$ is of a mixed type, however, and the contributions to the energy transfer are of great interest. The interactions are calculated in three cases around $\frac{L}{L_\rho} = 1$ and shown in Fig. 4.10. A strong current case with $\frac{U}{C} = 2.5$ will be considered first. The baroclinic process always releases available potential energy towards the perturbation, but the barotropic process does not. When $\frac{L}{L_\rho} = 1.0$ and 2.0 , the flow is unstable baroclinically and a part of the perturbation energy feeds back to the unperturbed kinetic energy through the barotropic interactions, which are 14% and 4% of the baroclinic energy transfer, respectively.

The direction of the energy transfers resembles the results of classical baroclinic instability problem with a weak horizontal shear (Stone, 1969; McIntyre, 1970), but the horizontal shear in this case is not weak at all. For a reduced horizontal scale as $\frac{L}{L_\rho} = 0.4$, the barotropic interaction not only works in the opposite direction converting the available kinetic energy towards the perturbation, but overrides the baroclinic interaction by 0.63 to 0.37. This augmentation of the instability accounts for the rise in $\frac{\alpha}{U/L}$ near $\frac{L}{L_\rho} = 1$, in Fig. 4.4. A similar reversal in the kinetic energy transfer was also found in a channel flow by Simmons (1974). These two examples



P = POTENTIAL ENERGY OF WAVE
 K = KINETIC ENERGY OF WAVE
 E = TOTAL ENERGY OF PERTURBATION

BAROCLINIC INTERACTION VS. BAROTROPIC INTERACTION

Fig. 4.10 The balance between the two distinct energy transfer processes is very sensitive to the ratios L/L_ρ and U/C as well. Potential energy of the wave is always available for growing perturbations, yet kinetic energy of the wave is not. Note a feedback of energy toward the wave for a strong current, $\frac{U}{C} = 2.5$.

illustrate a dramatic change in the energy transfer for a relatively small change of length scale around the radius of deformation; from a baroclinically controlled flow into a barotropically controlled flow and from intensifying the horizontal shear into releasing the same shear.

For a two-layer cosine jet in the atmosphere Brown (1969) has found numerically a potential energy transfer to the jet, in ratio 1 to 0.06, at the largest growth rate (See Table 1, Brown).

In a weak current as $\frac{U}{C} = 0.5$ the effect of baroclinic interactions are similar to a strong current case, but the restoring β -effect stops the feedback of the kinetic energy to the unperturbed field at $\frac{L}{L_\rho} = 1.0$ and 2.0, in contrast with a strong current case. When $\frac{L}{L_\rho} = 1.0$ the baroclinic interaction accounts for 29% of the total energy transfer to the growing perturbation. For $\frac{L}{L_\rho} = 2.0$ it becomes 91%. This is a new result which has not been known until now and could be significant in a geophysical situation where the current is not strong.

V. DISCUSSIONS AND GEOPHYSICAL APPLICATIONS

The prime object of this study was to find the fastest-growing perturbation and its energetics in a wide variety of velocity and length scales, appropriate to the geophysical situation. Before going into the discussion of the properties of nonlinear interactions it may be worthwhile to seek the justification of the method employed in the analysis and its accuracy. The parameter ranges considered in this study are $0.1 < \frac{U}{C} < 10$ and $0.1 < \frac{L}{L_\rho} < 10$.

It was decided that the Fourier analysis is most suitable for the object of this study, because it is uniformly valid for a wide range of parameters as long as a convergent series exists. There are other methods such as WKBJ analysis (Stone, 1969; Gent, 1974) and perturbation formalism (McIntyre, 1970), but their usage is limited in a current with a weak horizontal shear, corresponding to $\frac{L}{L_\rho} \gg 1$. The accuracy of the truncation analysis depends upon how fast a series converges. The distribution of streamfunction amplitudes in Fig. 4.8a shows a very fast convergence for $\frac{U}{C} < 1$ and $\frac{L}{L_\rho} < 1$ and a rather slow convergence for $\frac{U}{C} > 1$ and $\frac{L}{L_\rho} > 1$. But no significant change in the characteristics is expected by including more modes than analyzed here because the amplitudes at $n = \pm 3$ which are the highest modes in 7-mode analysis, drop to 20% of the amplitude at $n = 0$ already and the 9-mode

growth rate is found to be different from the 7-mode one by only 2% at most. It is also encouraging to find that the growth rate from this study is almost identical with the value for the same parameters from Simmons (1974) which is claimed to be accurate to one part in a thousand.

Beta-effect

The most interesting result of this study is that the meridional current is apparently unstable irrespective of its strength and horizontal scale. The instability of a weak current will be discussed first. The existence of growing perturbations in a current with $\frac{[U]}{[C]} < 1$, $[U]$ being the amplitude of a meridional current and $[C]$ the phase speed of the baroclinic Rossby wave, is shown analytically in eqs. (4.7a) and (4.7b) from the 3-mode analysis and the same conclusion is drawn from the higher mode analyses. In other words, the beta-effect represented by the phase speed $[C]$ is not capable of stabilizing certain perturbations in the meridional current, however strong it may be. We must, however, admit an incompleteness in the analysis in the limit $\frac{U}{C} \rightarrow 0$. There, the choice of Fourier components will have the added constraint that the perturbations satisfy the free-wave dispersion relation. Such a resonant-wave instability requires special analysis. All indications are that the instability will continue to

be effective, while selecting from a narrower set of waves than in the present case.

This instability with a relatively strong beta-effect is in contrast with what is found in the instability of a zonal current. For a barotropic current Kuo (1949) found that an extremum of absolute vorticity is necessary for instability. For a baroclinic current with a horizontal shear in a two-layer model Pedlosky (1964a) showed that for the instability it is necessary

$$\int dy \sum_{\alpha=1}^2 H_{\alpha} \frac{\partial q_{\alpha}}{\partial y} \frac{|\phi_{\alpha}|^2}{|U_{\alpha}-C|^2} = 0$$

with the potential vorticity gradient defined as

$$\frac{\partial q_1}{\partial y} = \beta - u_{1yy} + F(u_1 - u_2) \quad \text{and} \quad \frac{\partial q_2}{\partial y} = \beta - u_{2yy} + F(u_2 - u_1).$$

This is a special case of the instability criteria derived by Charney and Stern (1962) for a continuously stratified fluid and includes Kuo's (1949) criteria naturally if $u_1 = u_2$. In either case whether the current is barotropic or baroclinic, it is very clear that a sufficiently strong beta-effect compared with the horizontal and vertical shears will always stabilize the zonal current.

Then what happens in a meridional current? The role of the beta-effect is to propagate disturbance by restoring a meridional component of the disturbance velocity. An

incipient perturbation motion in a zonal current is oriented meridionally and the motion feels the beta-effect as soon as fluid starts to move. Therefore the perturbation will simply propagate unless it has a sufficient momentum to overcome the restoring mechanism by the beta-effect. However the zonally oriented particle motion associated with perturbations in a meridional current is fully adjusted to the beta-effect already and this effect has no apparent control on such perturbations. It should be remembered that the basic state is propagating and the perturbations are analyzed in a moving frame with the phase speed of the basic wave.

The same kind of a dynamical consequence was once found by Schulman (1967) who concluded in an investigation of the instability of steady, uniform meridional current that the fact that the perturbation motion is on the beta-plane is irrelevant in so far as locating the absolute maximum growing wave. Recently Robinson and McWilliams (1974) have stated that the influences of both the beta-effect and topography diminish as their gradient directions become parallel to the shear direction, suggesting a similar dynamical situation without any specific consideration. It may be pointed out that most of basic flows considered by Robinson and McWilliams (1974) are not, themselves, steady solutions of the equations of motion, for they

cross geostrophic contours. The instability results for such flows should be reexamined. The present work is meant to improve upon the situation, for the basic (oscillating) state is a solution.

Instability of Current with $L < L_\rho$

The current in this study is characterized by the presence of a horizontal shear as well as vertical shear. The relative strength of the shears is measured by the parameter L/L_ρ and the stability analysis for various values of L/L_ρ makes it possible to examine the changing role of each shear in energy transfers. First we will consider the range $L < L_\rho$. In a limit $L/L_\rho \rightarrow 0$ the coupling between the two layers is negligible and each layer behaves more or less independently. In terms of energy there is very little available potential energy associated with the vertical shear compared with the available kinetic energy with the horizontal shear. Therefore it is expected the characteristics are close to those of barotropic instability. Indeed the growth rate in eq. (4.8) is found to be identical with what Gill (1974) found in a barotropic Rossby wave. The vertical structure of the growing perturbations, a mixture of barotropic and baroclinic parts, in this limit merely assures that two independent instabilities will occur simultaneously in the two layers.

It is interesting to compare the scales involved. The fastest-growing perturbation has a scale larger than the scale of the unperturbed state by about 50%. The difference is not very large, but it is persistent. As the unperturbed scale L approaches the radius of deformation L_ρ , the perturbation scale also approaches the radius of deformation. What distinguishes the perturbation from the unperturbed field is their vertical structures. The pure baroclinic field transforms into a mixture of baroclinic and barotropic. There is also a very significant change in the growth rate. The normalized growth rate $\frac{\alpha}{U/L}$ increases almost linearly with L as shown in Fig. 4.6. This must be due to the increasing importance of the vertical shear as $L \rightarrow L_\rho$: more potential energy is available for the perturbation and it can be released without interfering with the barotropic interaction. For $\frac{L}{L_\rho} = 0.4$ the baroclinic generation accounts for 25% of the total energy transfer when $\frac{U}{C} = 0.5$ and 37% when $\frac{U}{C} = 2.5$. This enhanced instability by the vertical shear is believed to be a novel result.

Instability of current with $L > L_\rho$

Compared with a wide range of possible unperturbed scales it is rather remarkable to find that the meridional scale of the most unstable perturbation is fixed at the

radius of deformation. Zonally the perturbation is expressed as a superposition of many modes and it is found that the purely zonal component with $n = 0$ has the largest amplitude. It should be pointed out that the higher mode with $|n| > 0$ does not introduce a scale larger than the meridional scale as can be seen in eq. (4.1). Therefore the meridional scale is the largest possible scale in the perturbation. The perturbation amplitudes at $n = \pm 1, \pm 2$ in Fig. 4.8a are substantial for $L \gg L_\rho$, with scales equal to

$L_p / (1 + n^2 \frac{L_p^2}{L^2})^{1/2}$. However, these do not change the scale very much because $L_p \approx L_\rho$ and $L \gg L_\rho$. In summary we conclude that any current with a scale larger than the radius of deformation is most unstable with respect to the perturbation with the radius of deformation.

The reduction in the growth rate $\frac{\alpha}{U/L_\rho}$ with a decreasing L/L_ρ is a most interesting feature in this range. It can be noticed that the rate of reduction increases as $L \rightarrow L_\rho$. In fact, this can be explained in terms of the individual energy transfers. From the scale it is obvious that the available potential energy is the main source of the growing perturbation. The question is what the barotropic interaction with the horizontal shear does during the instability process. In a strong current with $\frac{U}{C} = 2.5$ it is found in Fig. 4.10 that the barotropic interaction counteracts the baroclinic interaction and transfers

energy back to the unperturbed field. The stronger the horizontal shear is, the more feedback of energy. Therefore the effect of the horizontal shear, which is negligible when $L \gg L_\rho$, is to cause a reduction in the growth rate as $L \rightarrow L_\rho$. In fact this is not an entirely new finding and there have been numerous studies where the same tendency is found either analytically or numerically. But no systematic approach has been carried out so far because of the difficulty in mathematical analyses.

A new finding may be that the feedback does not occur in a weak current. As explained already the current with $\frac{U}{C} < 1$ is unstable and the barotropic interaction also extracts energy from the unperturbed flow for $\frac{L}{L_\rho} = 1.0$ and 2.0 when $\frac{U}{C} = 0.5$, as shown in Fig. 4.10 This indicates that the kinetic energy transfer in baroclinic flow depends not only on the scale, but on the current strength too. The reduction in the growth rate for a weak current may be an extension of the increasing growth rate in the range $L < L_\rho$, but the physical explanation requires further investigations.

Rhines' Numerical Experiments

Some of the numerical experiments carried out by Dr. Rhines at the Woods Hole Oceanographic Institution are closely related to this study. Two experiments are discussed here with Dr. Rhines' permission. In Rhines' model

the lower layer is thicker than the upper layer by a factor of 3.5 and fluid is viscous. The vorticity equations identical to eqs. (2.16,17) are solved first in a wavenumber space and the solutions are transformed into a physical space. The wavenumber corresponding to the radius of deformation is $k_\rho = 8$. Experiment I which originally motivated this study, is concerned with the instability of a large-scale baroclinic Rossby wave and Experiment II is useful in comparing instabilities associated with two very different length scales.

Experiment I: Instability of a baroclinic Rossby wave

$$\frac{U}{C} = 3.2, \quad \frac{L}{L_\rho} = 4.$$

Figure 5.1 shows the development of the instability in a series. The stream lines run in a meridional direction initially with very weak perturbations. At $t = 1.0$ ($t = 1$ is equivalent to about 23 days) the growing perturbations are easily visible and further amplification is very clear at $t = 1.5$. The slow westward propagation of the stream lines can be seen along the left and right edges. The wavenumber of the fastest-growing perturbation is $k_p = 6$, which suggests a scale larger than a predicted scale from the theory by 30%. This discrepancy may be due to the different vertical structure and initial noise at wavenumber 6 and 7. The variation of energies at $k = 6$ in time is shown in Fig. 5.2. The growing rate of the total energy is indeed almost exponential, which is 14%

INSTABILITY OF A BAROCLINIC ROSSBY WAVE

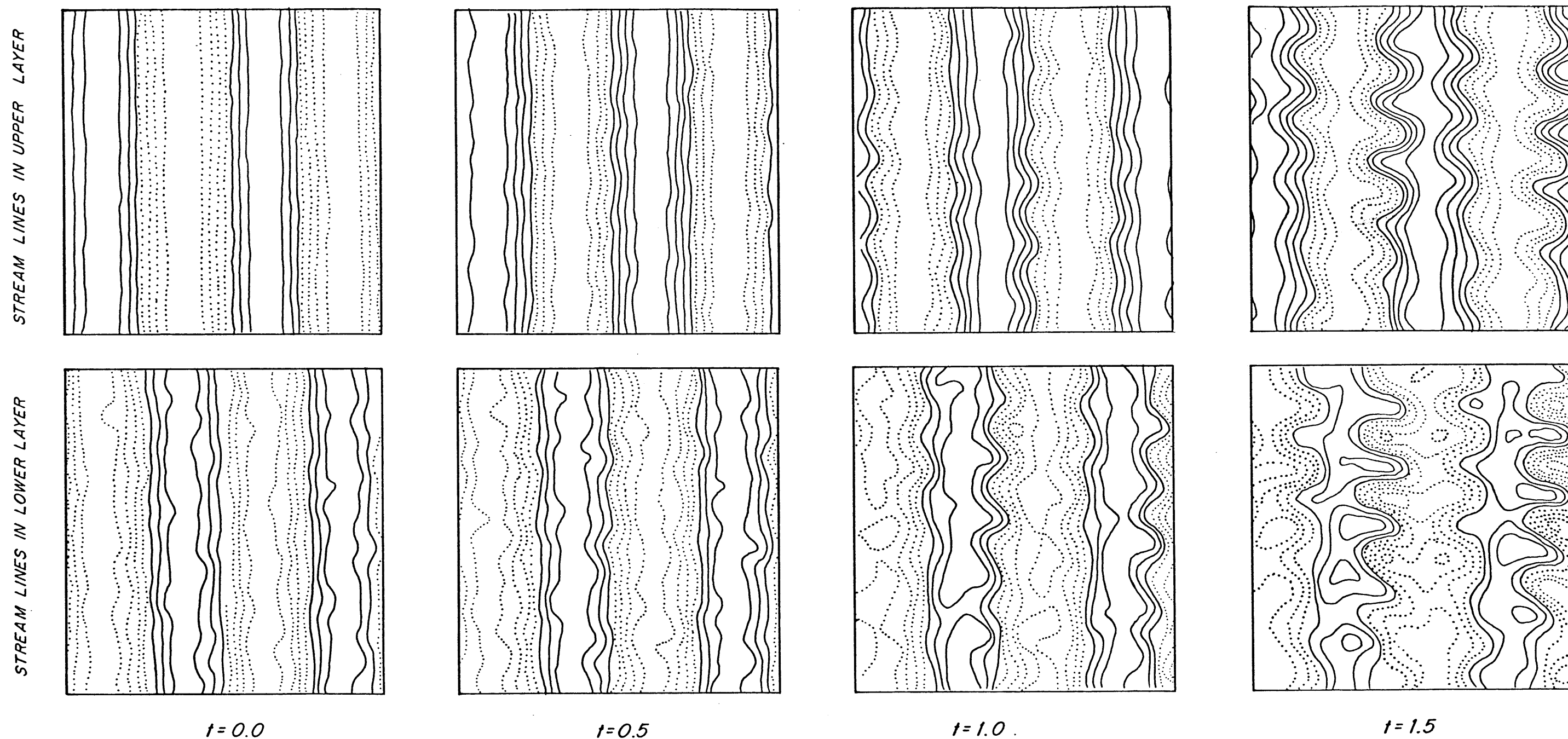
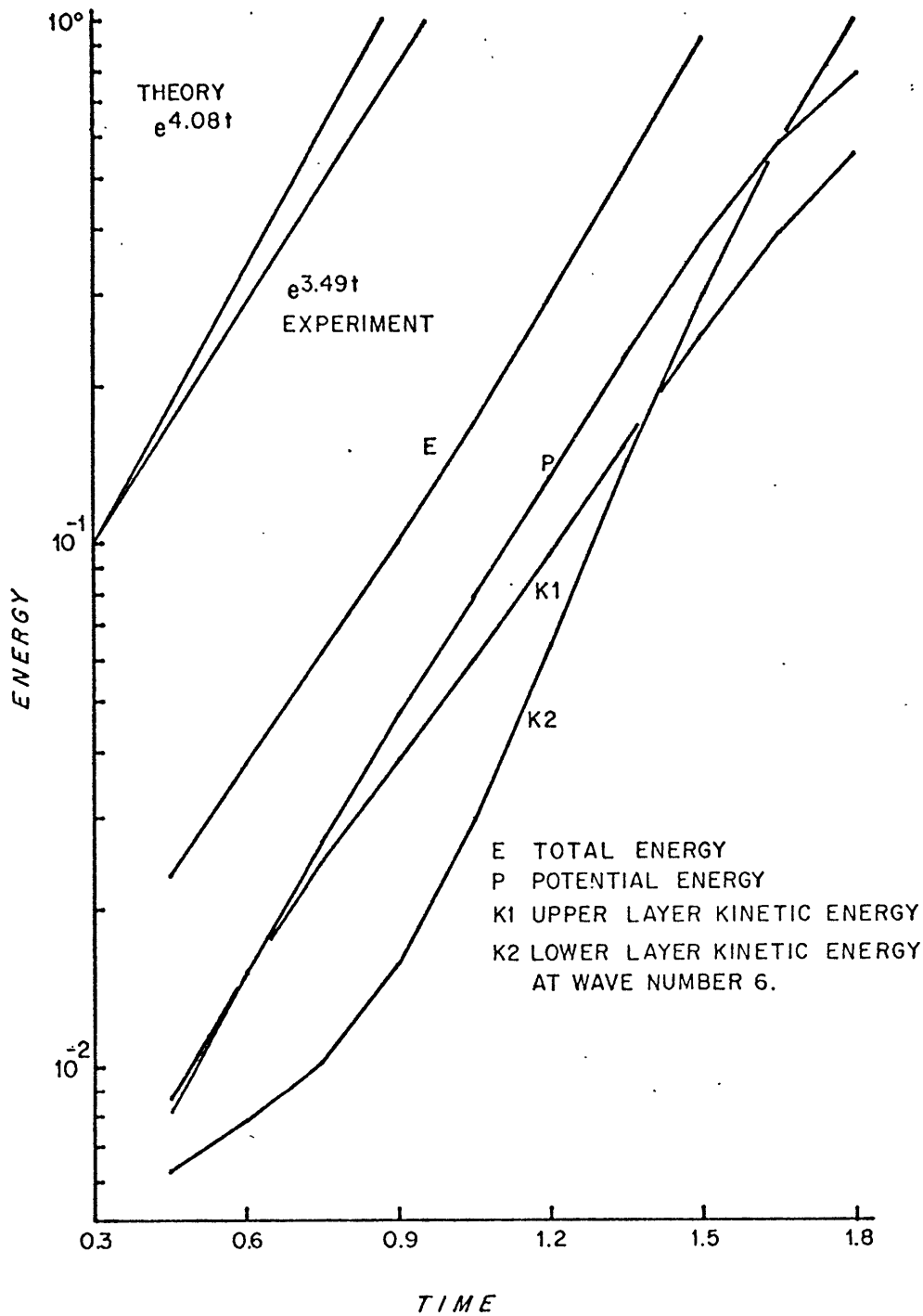


Fig. 5.1 Rhines' (1975a) numerical experiment shows that a large-scale baroclinic wave with $L \approx 4 L_p$ is unstable and 'noise' develops into eddy field. Small-scale propagation of stream lines are visible along left and right edges. (about 23 days later) organized eddy field can be identifiable and amplification is very clear at $t = 1.5$



INSTABILITY OF BAROCLINIC ROSSBY WAVE

Fig. 5.2 Perturbation energy grows exponentially as predicted in the theory during the instability shown in Fig. 5.1.

smaller than the predicted rate from the theory for the case $\frac{U}{C} = 2.5$ (3.2 in the numerical experiment) and $\frac{L}{L_\rho} = 4$. In Fig. 5.3 the energy transfer is dominated by the potential energy transfer from $k = 2$ to $k = 5, 6$ and 7 , which is consistent with the theory. There is a loss of the kinetic energy at $k = 6$, but the net kinetic energy increases via the conversion from the potential energy at the same wavenumber supplied by the instability. It is believed that the dissipation is so small it does not affect the energy transfer. This experiment occupies only one point in the parameter space, but it verifies the nature of the theoretical results.

Experiment II: Instability with Two Scales

At the beginning the lower layer is at rest and the energy spectrum has two peaks, one at $k = 1$ and the other at $k = 5, 6$ and 7 . The energies are prescribed as follows:

k	kinetic energy	potential energy
1	2.2512×10^{-2}	1.1256
5	3.7538×10^{-1}	7.0384×10^{-1}
6	6.5691×10^{-1}	9.3845×10^{-1}

The subsequent development is presented in terms of the energy transfers in Fig. 5.4. It is obvious that the interactions around $k = 6$ are of order of magnitude stronger

INSTABILITY OF BAROCLINIC ROSSBY WAVE

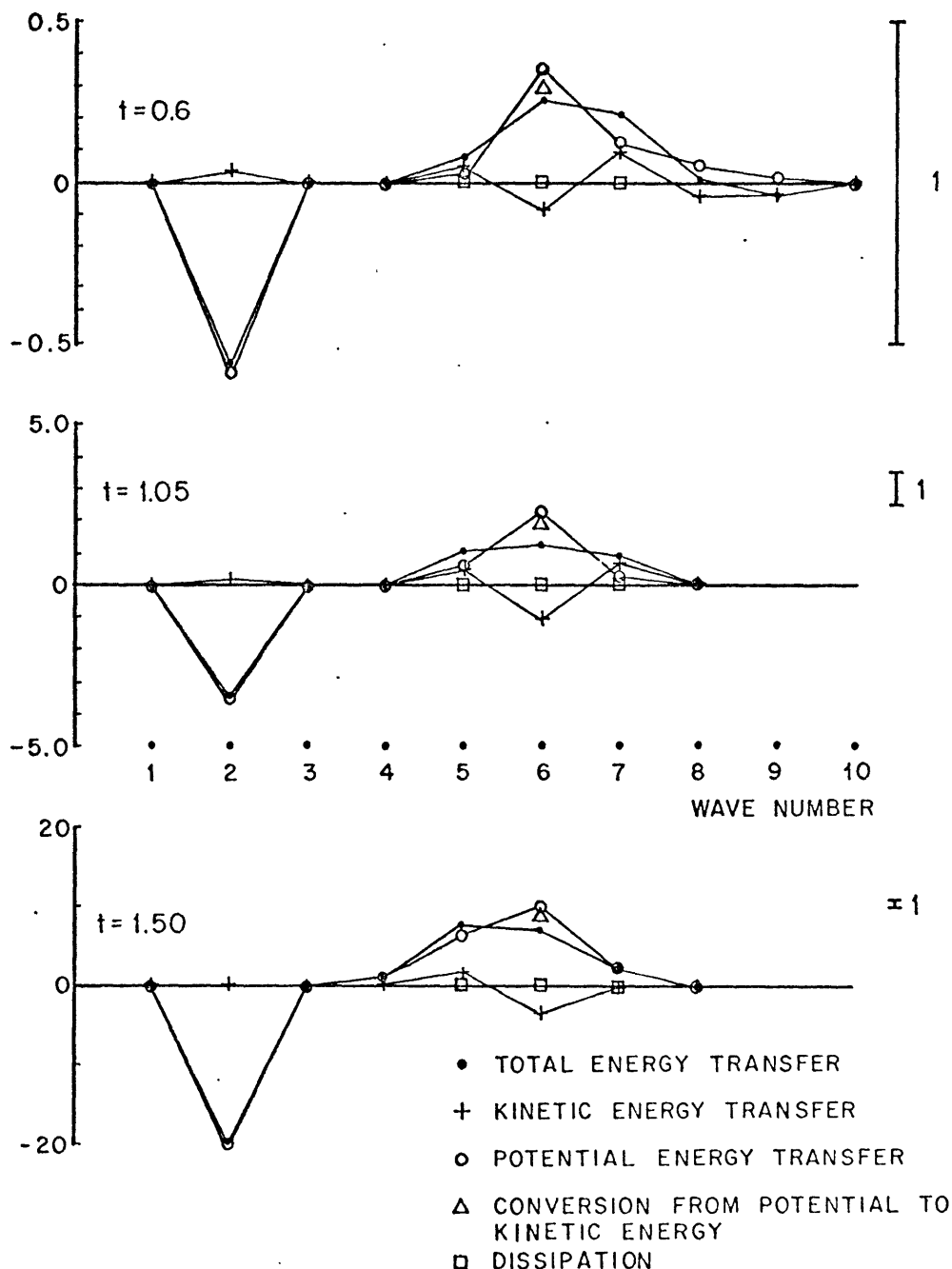


Fig. 5.3 Energy transfer during the instability shown in Fig. 5.1 is dominated by the baroclinic process. Barotropic interaction removes kinetic energy from wavenumber 6, but the net kinetic energy increases via the conversion from the potential energy at the same wavenumber supplied from wavenumber 2 by the instability.

INSTABILITY WITH TWO SCALES

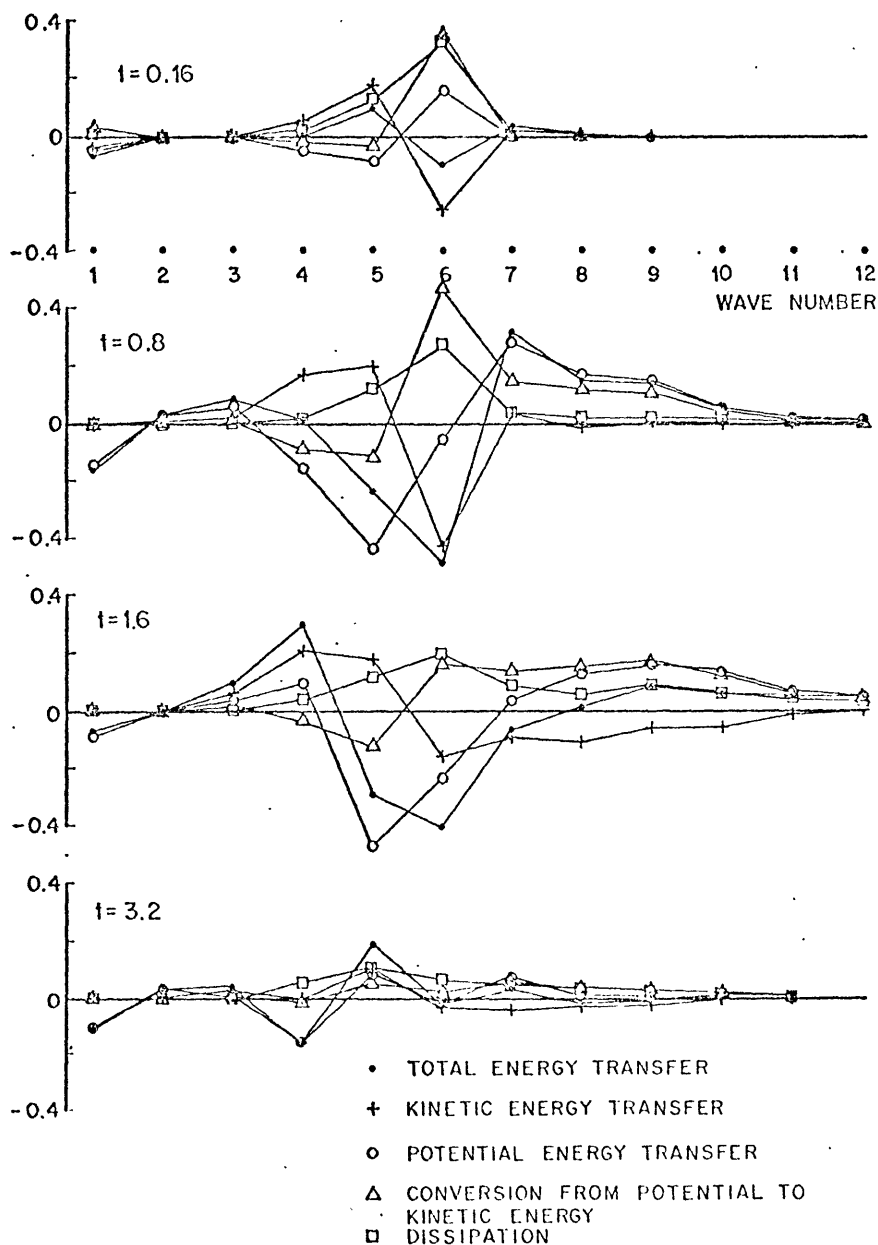


Fig. 5.4 Initially energy spectrum has two peaks, one at $k = 1$ and the other around $k = 6$. Subsequent energy transfers toward higher wavenumbers ($k = 8$ corresponds to the radius of deformation) are concentrated around $k = 6$ with very little change at $k = 1$. This development is consistent with the theoretical prediction.

than those at $k = 1$, although the potential energy at $k = 1$ is the largest initially. The high kinetic energy level at $k = 6$ makes the wavenumber six most unstable as predicted from the theory. It should be noted in the comparison that the current for $k = 1$ flows zonally in Rhines' experiment and it may be dynamically stable since C is slightly smaller than U . It is speculated that the strong dissipation of energy throughout the wavenumbers may tend to drain energy from the low wavenumber to high wavenumber as energies at high wavenumber increase.

Experiments I and II are also repeated when a realistic bottom topography is present. The results can be stated that the bottom does affect the lower layer motion by scattering energies toward the high wavenumbers, but it does not totally inhibit the instability process in any case.

Geophysical Application

What does this model imply in the ocean? Applying the theoretical results it is now possible to examine the stability of various currents of different strengths. So far the instability theories concerned with the oceanic process have been limited for a steady current with such a large scale that the current can be considered to be horizontally uniform (Robinson and McWilliams, 1974; Gill,

Green and Simmons, 1974). Although the predicted scale of the most unstable perturbation is similar to the scales of the observed eddies, the artificial assumption of steadiness and uniformity requires an artificially large vertical shear across the main thermocline greater than or equal to 5 cm/sec, as it is steady and uniform, to give an e-folding time scale of 60-80 days.

In reality the large vertical shear does exist, but it is associated with a finite scale, as found in the eddies themselves, and intermediate scales of Katz (1973), which means that the assumption of uniformity cannot be justified in reality. Nevertheless this argument does not exclude a possibility that the very large-scale density field is unstable. Its shear is weak in reality so that it will take such a long time as one year for its perturbation to grow. Measurement of this slow process is very doubtful. However, the geostrophic shear associated with Katz's (1973) profile is 2 cm/sec/100 m, which gives a shear of 4-5 cm/sec at least across the thermocline. The e-folding time scale from this model is

$$T_e = \frac{1}{\Gamma} \frac{L_\rho}{U}$$

where Γ is the nondimensional growth rate $\frac{\alpha}{U/L_\rho}$. As shown in Fig. 4.6, Γ varies about 20% as the scale of the unperturbed field changes from L_ρ to ten times L_ρ , but its

effect in T_e is minor compared with the change due to U . Taking $\Gamma = 0.45$, $L_\rho = 50$ km, $U = 5$ cm, we have $T \approx 30$ days. Larger shears than this one are often seen, and imply even faster growth of the instability.

This example shows clearly that nonlinear interactions between scales around the radius of deformation are much stronger than any other interaction in the geophysical situation. It should be emphasized that there is no unique mean current as far as the energetic eddies at the radius of deformation are concerned, since they receive energy from any scale. Upon separating currents into eddies and a time-mean flow, the present analysis may be described as a model of eddy-eddy interaction, which shows its vigor, compared with eddy-mean flow interactions in mid-ocean.

The instability of currents with scales smaller than the radius of deformation generates a scale which is closer to the radius of deformation. This suggests that all the energies will be eventually transferred to the radius of deformation through a series of similar instability if the system is left to interact freely. This feature is similar to what Rhines (1975b) found in a homogeneous fluid; expansion of scale is ceased at the radius of deformation in a stratified fluid here, whereas the beta-effect stops the migration of energy at a particular wavenumber $(\beta/2U)^{1/2}$ in Rhines' case.

Another aspect of interest is the change in vertical structure accompanying these instabilities; a purely baroclinic field generates a mixture of barotropic and baroclinic modes, and reduces its vertical shear. This is a theoretical indication of the strong changes of vertical structure found in geostrophic turbulence.

Some assumptions and simplification are made at the beginning of the analysis and deserve discussion in the application of this model. Hart (1974) shows a reduction of the growth rate for a two-layer ocean with an upper layer thinner than the lower layer by a ratio of $\delta < 1$. The growth rate decreases in proportion to $\delta^{1/2}$ approximately; it changes very gradually for $0.3 < \delta < 1$ and drops significantly for $\delta \sim 0.1$. To be realistic, it is necessary to take into account this change. The neglect of the bottom topography may be justified, based upon the Rhines' numerical experiments, which show that the realistic bottom does not interfere with the instability process until the perturbation reaches a finite magnitude. This model is not applicable for finite amplitude perturbations, because they are assumed to be infinitesimal.

Finally, it should be mentioned that there is a need to explore a further general solution, including subharmonic components, aperiodic part, and weak interaction limit as $\frac{U}{C} \rightarrow 0$.

VI. CONCLUSIONS

The stability analysis in a truncated Fourier series shows that any baroclinic Rossby wave propagating westward in a two-layer ocean with currents oriented meridionally is unstable with respect to an infinitesimal perturbation and barotropic and baroclinic perturbation currents are generated. This is consistent with the dual nature of non-linear eddies that currents propagate while changing their vertical and horizontal structures simultaneously, which has been found in observations as well as numerical experiments.

The beta-effect has no apparent stabilizing effect in the meridional current in contrast with its decisive role in the stability of a barotropic or baroclinic zonal current.

The velocity field described by a baroclinic Rossby wave contains both vertical and horizontal shears with potential and kinetic energies available for growing perturbations, which are partitioned by L^2/L_ρ^2 , L being a wavelength/ 2π and L_ρ the radius of deformation. This study provides an opportunity to examine the variation of instability characteristics with L/L_ρ especially around $L \approx L_\rho$, which covers the most neglected part in the classical theory.

For $\frac{L}{L_\rho} > 2$ the source of growing perturbation energy is a potential energy associated with the vertical shear

and the fastest-growing perturbation has the scale of L_ρ . There exists a short wavelength limit of unstable perturbations in a meridional direction. It is found that the nondimensional growth rate increases gradually and approaches an asymptotic value as L/L_ρ increases.

For $\frac{L}{L_\rho} \approx 0.4$ it is found that growing perturbations extract their energy from both kinetic and potential energies. In a region $L \ll L_\rho$, the functional relationship between the growth rate and the length scale is found to be the same as that in the instability of a barotropic Rossby wave shown by Gill (1974).

In the region $0.4 < \frac{L}{L_\rho} < 2$, this study shows a smooth transition in the growth rate, but an abrupt change in a kinetic energy transfer. The nondimensional growth rate, $\frac{\alpha}{U/L}$ if $\frac{L}{L_\rho} < 1$ or $\frac{\alpha}{U/L_\rho}$ if $\frac{L}{L_\rho} > 1$, increases with L/L_ρ . Although no specific criteria are established, it is argued that the change in the direction of a kinetic energy transfer is responsible for the asymmetry in the instability characteristics, that is, the horizontal shear in a baroclinic current reduces the growth rate, while an introduction of a vertical shear in a strong barotropic current enhances the instability substantially.

The results of this study are particularly relevant in looking at the nonlinear interactions in the mid-ocean which may be characterized by a continuous spectrum of length

scales and no preference in the current direction. A zonal vertical shear of a few cm/sec across the main thermocline is stable, but a meridional shear of the same magnitude is dynamically unstable according to this model. Furthermore the scale of a current is not necessarily much larger than the radius of deformation for instability to occur. Instead the current with a scale close to the radius of deformation is more unstable in a sense that it has a shorter e-folding time. It is believed that this kind of intense instability around the radius of deformation is observable in a time-scale of a few months in an eddy-rich region such as the Sargasso Sea.

This model also suggests an influx of energy toward a particular scale, the radius of deformation, from scales both larger and smaller than the radius of deformation which in turn explains why the most energetic eddies found in the ocean have scales close to the radius of deformation.

The vast difference between the size of the ocean basin and the radius of deformation makes a direct nonlinear interaction between the two scales less efficient than any other interaction around the radius of deformation, which suggests that the understanding of nonlinear interactions around the radius of deformation and the collective properties of eddies is crucial in constructing a model of the general circulation in the ocean which may possibly contain hundreds of eddies.

PART II

I. INTRODUCTION

The role of potential energy in the dynamics of ocean currents was not fully recognized until it was realized that it can be converted to kinetic energy via baroclinic instability. In Part I of this thesis the transfer of energy between scales has been further investigated, showing that potential energy is always available for a growing perturbation and the instability characteristics change significantly with the availability of potential energy. Also the results of recent large-scale experiments suggest that the meso-scale dynamics are highly nonlinear as discussed in the Introduction of Part I.

One way to grasp the dynamics of a nonlinear system is to look at the flow of energy. The understanding of energetics in the ocean will not tell us the exact dynamics, but it will show us how the ocean works as a mechanical system. This is a classical approach which has been successfully applied in understanding the general circulation in the atmosphere. In discussing energetics in the ocean it is natural to ask what is meant by potential energy and how big it is and how it changes, yet there is surprisingly little relevant information in the literature.

It is familiar that eddies of scales near the deformation radius, L_ρ , have roughly equal potential and kinetic

energies, but the exact amounts are crucial to the dynamics, and do not seem to have been evaluated. In part, this may be due to the difficulty in defining 'available potential energy.' The objects of Part II lie here. Firstly, so-called available potential energy will be defined analytically. Secondly, this definition will be applied in the MODE-I and the Panulirus density data in order to gauge the strength of the potential energy present in mid-ocean in comparison with the kinetic energy.

The primitive definition of potential energy for a fluid particle with density ρ in a stratified, rotating system may be written

$$PE \equiv \rho g(z - z_r) \quad (1.1)$$

where g is the effective gravitational acceleration and $(z - z_r)$ the vertical distance from a reference level z_r . It should be pointed out that all particles have the common reference level z_r . Imagine now a state where the surfaces of constant density are level, which could be reached by redistributing the whole mass adiabatically. Then it is obvious that the potential energy at this particular state can not be converted into kinetic energy internally.

This led Lorenz (1955) to introduce the concept of available potential energy (APE) and to derive an analytic expression of the APE from the primitive definition by making use of the property of the potential temperature

conservation. The exact formula of the APE defined on the potential temperature-coordinate system is not practical and an approximate form of the formula has been used extensively in the estimate of the energetics in the atmosphere, notably by Oort (1964). For clarity, Lorenz's (1955) conceptual definition is quoted here, "The available potential energy of the atmosphere may be defined as the difference between the total potential energy and the minimum total potential energy which could result from any adiabatic redistribution of mass. It vanishes if the density stratification is horizontal and statically stable everywhere, and is positive otherwise."

A definition close to the concept of the APE has been used by Fofonoff (1962a), which is called the anomaly of potential energy χ ,

$$\chi(P) \equiv \frac{1}{g} \int_0^P P \delta dP \quad (1.2)$$

where P is pressure and δ the anomaly of specific volume. The anomaly δ is defined conventionally as

$$\delta \equiv \alpha(S, T, P) - \alpha_0(35 \text{ } ^\circ/\text{ } ^\circ, 0^\circ \text{ C}, P)$$

where α is a specific volume, equal to $1/\rho$, at salinity S , temperature T and pressure P and α_0 is a reference value. Table 1 shows examples of χ calculated from the data taken at an ocean station known as site D on three occasions. It

Table 1. Anomaly of potential energy χ .Unit is 10^8 ergs/cm².

Pressure	18-VI-67	9-VIII-67	3-X-67
1	.000	.000	.000
50	.201	.226	.301
100	.722	.799	.930
150	1.527	1.616	1.689
200	2.617	2.661	2.623
300	5.311	5.158	4.800
400	8.398	7.864	7.148
500	11.618	10.663	9.695
600	14.856	13.650	12.267
700	18.233	16.926	15.243
800	21.840	20.533	18.572
900	25.787	24.504	22.294
1000	30.162	28.902	26.430
1200	40.189	38.978	36.052
1400	51.971	50.885	47.694
1600	65.399	64.804	61.095
1200	80.402	80.478	76.386
2000	97.226	97.720	93.334
2200		116.713	111.737
2400		137.529	131.463

is noticed immediately that the anomaly χ increases monotonically with depth. Over the depth, most part of χ does not change in time and the amplitude of its fluctuating part also increases with depth. This tendency contradicts our anticipation of the APE distribution.

Suppose that the r.m.s. vertical excursion of a fluid particle is roughly uniform, vertically. Then we expect that the APE should be largest in the thermocline and decreases downward because the stratification does. The APE defined in the present study indeed reveals the expected vertical distribution and it is smaller than the fluctuating part of χ by an order of magnitude for all depth.

The exact formula of the APE in the ocean should be derived from the primitive definition utilizing the conservation laws of salinity and entropy in principle. However, the empirical equation of state of sea water is nonlinear with respect to thermodynamic variables (Fofonoff, 1962b) and there is no one-to-one correspondence among the density and salinity and entropy, because thermodynamic coefficients are again functions of state. Therefore the procedure which was taken by Lorenz (1955) in defining the exact formula in the atmosphere does not hold at all in the ocean. Nevertheless it is possible to derive an approximate expression of the APE in the ocean in terms of the potential density, which is equivalent to its counterpart in the atmosphere in terms of the potential temperature.

To summarize, below the APE will be formally separated into two parts, mean APE and eddy APE, and two energy equations are derived for them. The definitions vary with the type of data available (for instance, a time-series at a point or an instantaneous spatial map), and our notion of eddy and mean APE also depends on the constraints put on the fluid motion: the definitions are process-dependent. Locally the energies are changed by advection, transfer between the mean APE and the eddy APE and buoyancy fields. Available data will be used to estimate the eddy APE. The eddy APE per unit volume averaged over the MODE area ranges from 100 ergs/cm^3 at 300 m to 20 ergs/cm^3 at 2000 m, which are comparable with the kinetic energy density. The comparison of the eddy APE levels in the MODE area and at the Panulirus station shows a geographical difference below the main thermocline, which has not been seen before.

II. DEFINITION OF AVAILABLE POTENTIAL ENERGY

Potential energy is part of total energy of a fluid parcel and here we want to relate the available potential energy (APE) to kinetic energy (KE) without going into detailed discussions regarding the total energy and its variation. An energy equation can be written in the form of

$$\left[\frac{\partial}{\partial t} + \underline{u} \cdot \nabla \right] (KE + APE) = -\underline{u} \cdot \nabla p + \text{source terms},$$

where \underline{u} is a velocity vector. In an ocean which is isolated energetically (in such a time-scale that source terms are not important), the total energy of the system is conserved so that internal conversion and redistribution of energies are very important. Now the scalar product of \underline{u} and the Boussinesq momentum equation (Veronis, 1973) gives

$$\left[\frac{\partial}{\partial t} + \underline{u} \cdot \nabla \right] (KE) = -\nabla \cdot (P \underline{u}) + g \hat{\rho} w$$

where $\hat{\rho}$ is the local deviation of the potential density and w a vertical component of \underline{u} . The conversion from the APE is $g \hat{\rho} w$, as we shall see later.

Following a fluid particle in sea water, the potential density ρ_θ is conserved approximately as discussed by Veronis (1973), who has shown the dynamical significance of the potential density and the limitations to its use as well. It should be pointed out that the potential density is

referred to a reference pressure at one atmosphere, which is conventional but dynamically important because it represents density after all the pressure effects are removed. In terms of the exact equation of state it is debatable whether the potential density is really conserved or not, but for present purposes, where we follow water parcels for times of order one year, and depth excursion of order 100 m, the approximation should suffice. Therefore, neglecting diffusion and source,

$$\left(\frac{\partial}{\partial t} + \underline{u} \cdot \nabla\right) \rho_{\theta} = 0. \quad (2.1)$$

First, suppose that the potential density is separated into three parts:

$$\rho_{\theta}(x, y, z, t) = \bar{\rho}(z) + \tilde{\rho}(x, y, z, t) + \rho'(x, y, z, t) \quad (2.2)$$

where

$$\bar{\rho} \equiv \{\rho_{\theta}\}$$

$$\tilde{\rho} \equiv \langle \rho_{\theta} \rangle - \{\rho_{\theta}\}$$

$$\rho' \equiv \rho_{\theta} - \langle \rho_{\theta} \rangle .$$

Here the bracket $\langle q \rangle$ denotes an average of q over some suitable horizontal area (a few hundred kilometers squared) and $\{q\}$ an average over the entire horizontal space. Hence an instantaneous density field is represented by the reference

stratification $\bar{\rho}$, slowly varying mean field $\tilde{\rho}$ and δ' a deviation from $(\bar{\rho} + \tilde{\rho})$. This separation is appropriate to a data set of spatial maps of the density field, covering at least a few hundred kilometers squared. The idea is to make a two-scale separation in which the basin-wide APE appears in $\tilde{\rho}$, while the APE in energy-containing eddies appears in ρ' .

Substituting for ρ_θ in eq. (2.1) yields

$$\left(\frac{\partial}{\partial t} + \underline{u} \cdot \nabla\right) \tilde{\rho} + \left(\frac{\partial}{\partial t} + \underline{u} \cdot \nabla\right) \rho' = -w \frac{d\bar{\rho}}{dz} \quad (2.3)$$

Multiply eq. (2.3) by $\tilde{\rho}$ and take an average with $\langle \rangle$, it is possible to obtain after some manipulation:

$$\begin{aligned} \left(\frac{\partial}{\partial t} + \underline{u} \cdot \nabla\right) \left(\frac{1}{2} \tilde{\rho}^2\right) &= \nabla \cdot [\tilde{\rho} \langle \rho' \underline{u}' \rangle] \\ &+ \langle \rho' \underline{u}' \rangle \cdot \nabla \tilde{\rho} - \tilde{\rho} \tilde{w} \bar{\rho}_z \end{aligned} \quad (2.4)$$

where $\bar{\rho}_z = \frac{d\bar{\rho}}{dz}$.

Here, it is assumed approximately that

$$\frac{\partial}{\partial t} \langle \tilde{\rho} \rho' \rangle = \langle \underline{u}' \cdot \nabla \left(\frac{1}{2} \tilde{\rho}^2\right) \rangle = \langle \tilde{\rho} \underline{u}' \cdot \nabla \rho' \rangle = 0$$

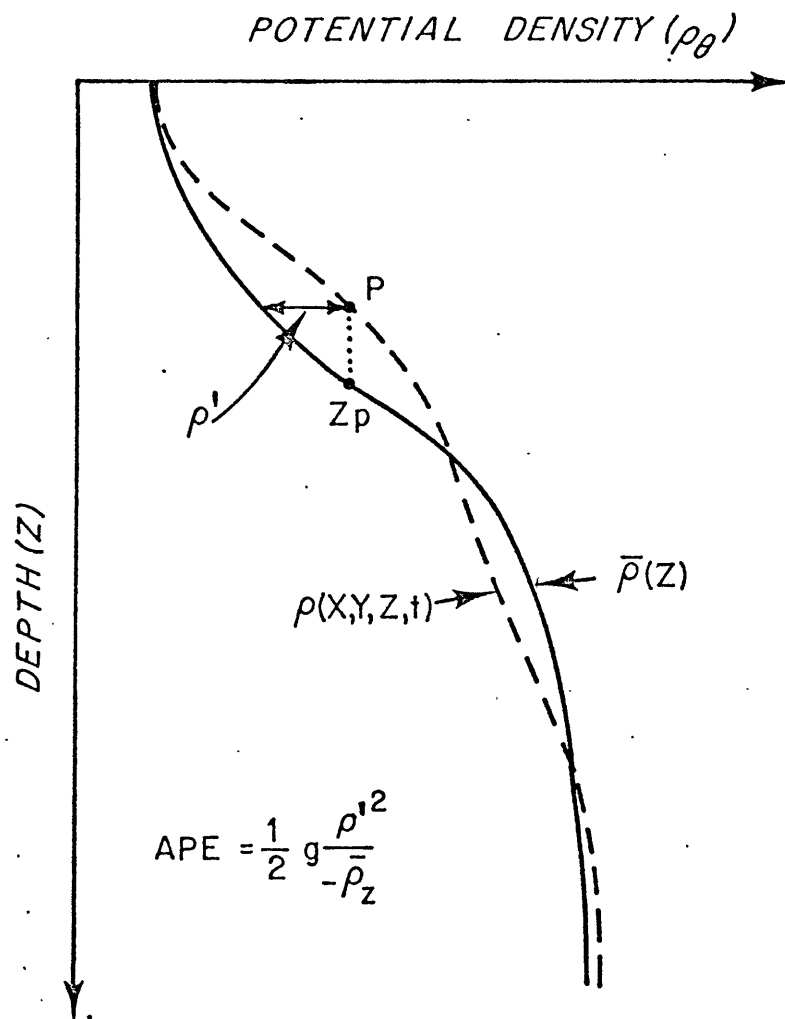
and $\nabla \cdot \underline{u} = 0$ by Boussinesq approximation. Multiplying eq. (2.3) by ρ' and taking an average $\langle \rangle$ again we obtain

$$\left(\frac{\partial}{\partial t} + \underline{u} \cdot \nabla\right) \left(\frac{1}{2} \langle \rho'^2 \rangle\right) = -\langle \rho' \underline{u}' \rangle \cdot \nabla \tilde{\rho} - \langle \rho' w' \rangle \bar{\rho}_z \quad (2.5)$$

with $\langle \underline{u}' \cdot \nabla \left(\frac{1}{2} \rho'^2\right) \rangle = 0$ approximately.

CTD and STD station data in a circle of 200 km in radius in the MODE area, the value of r varies from 1.8×10 to 10^4 in c.g.s. units. The last ratio $\textcircled{J}/\textcircled{I}$ is found to be as large as 0.22 at 500 m depth at the Chain station 9 (see Table 2a and Fig. 3.5a), but it is typically less than 0.1 for the depth from 300 m to 2000 m if it is assumed that $|\tilde{w}| \leq |w'|$. Similarly $\textcircled{E}/\textcircled{D}$ will be of the same order as $\textcircled{J}/\textcircled{I}$ if $\tilde{\rho}$ is the same order of magnitude as ρ' . If we estimate $\tilde{\rho}$ and ρ' by $\bar{\rho}_z h$ where h is a maximum vertical excursion of a fluid particle from the reference state, then $(\textcircled{E}/\textcircled{D}, \textcircled{J}/\textcircled{I}) \sim h/H$ where H is the height scale of a thermocline. A typical estimate of h/H may be 0.2 if $h = 200$ m and $H = 1000$ m. Based upon the direct estimate from data and the typical order of magnitude estimate we may neglect the terms \textcircled{E} and \textcircled{J} in eqs. (2.6) and (2.7).

The definitions of the APE are apparent in \textcircled{A} in eq. (2.6) and \textcircled{C} in eq. (2.7) and the physical meaning of the APE can be best illustrated by an example. Suppose a reference stratification shown as a solid line and an instantaneous state as a broken line in Fig. 2.1. The APE of a particle P is given by the formula in eq. (2.9) later, which can be rewritten as $\frac{1}{2}g\rho'(z - z_p)$ by approximating $\rho' \approx -\bar{\rho}_z(z - z_p)$ locally where z_p is the reference position of the particle P . Now the APE can be interpreted as the work done by a local mean buoyancy force $\frac{1}{2}g\rho'$ for a displacement of $z - z_p$. Accordingly each fluid particle has



DEFINITION OF AVAILABLE POTENTIAL ENERGY

- Fig. 2.1 An available potential energy (APE) is defined as work done by a local mean buoyancy force $\frac{1}{2}g\rho'$ for a displacement of $z - z_p$, where ρ' is approximated by $-\bar{\rho}_z(z-z_p)$. Note that the APE is positive definite. Accordingly each fluid particle has its own reference level in the definition of the APE.

its own reference level in the definition of the APE and the APE measures the amount of work required to move a particle away from its individual reference level. This definition of potential energy is familiar in the study of internal waves (Fofonoff, 1969; Garrett and Munk, 1972).

Why should we be denied an "exact" potential energy? The answer lies in the need to relate the local density anomaly (relative to the time-mean at the same level, say) to the amount of work done, equal to $-\int (\text{buoyancy}) \cdot dz$, in raising the fluid from its 'rest' level. This can be done exactly if $\bar{\rho}_z$ is linear, but curvature in the mean profile makes the work done depend on the history of the particle trajectory as well as its local value of ρ' . (Of course, in a layered model the definition of the APE again becomes exact, for the dependence on history disappears.)

Definition: The available potential energies per unit volume are defined as:

$$A_M = \frac{1}{2g} \frac{\tilde{\rho}^2}{-\bar{\rho}_z} \quad (2.8)$$

$$A_E = \frac{1}{2g} \frac{\rho'^2}{-\bar{\rho}_z} \quad (2.9)$$

where A_M will be called the mean available potential energy and A_E the eddy available potential energy. The mean and eddy APE represent part of the APE associated with $\tilde{\rho}$ and ρ' , respectively.

A second definition is appropriate to an ocean without basin-wide variations (i.e., the potential density field is statistically homogeneous). Then we divide the potential density into two parts, $\bar{\rho}(z)$ and ρ^* , and the available potential energy will be defined as

$$A = \frac{1}{2g} \frac{\overline{\rho^{*2}}}{-\bar{\rho}_z} \quad (2.10)$$

and the energy equation corresponding to this definition will be

$$\left(\frac{\partial}{\partial t} + \underline{u} \cdot \nabla \right) \left(\frac{1}{2g} \frac{\rho^{*2}}{-\bar{\rho}_z} \right) = g\rho^*w[1 + O\left(\frac{h}{H}\right)]. \quad (2.11)$$

While this situation may not exist in practice, it is an idealization that permits useful analysis of hydrographic time series at a single geographical point.

With the definitions of the mean APE and the eddy APE in eqs. (2.8) and (2.9) the meaning of the terms in eqs. (2.6) and (2.7) become clear. In eq. (2.6) \textcircled{B} represents the redistribution of A_M by the eddy field, \textcircled{C} the conversion between A_M and A_E , \textcircled{D} the conversion between A_M and the mean kinetic energy, $\frac{1}{2}\rho\tilde{u} \cdot \tilde{u}$. Also in eq. (2.7) \textcircled{H} represents the conversion, equal to $-\textcircled{C}$, and \textcircled{I} the conversion between A_E and the eddy kinetic energy $\frac{1}{2}\rho\underline{u}' \cdot \underline{u}'$. It should be remembered that not A_E , but the horizontal average of A_E by $\langle \rangle$ is involved in eq. (2.7).

The definitions of A_M and A_E are equivalent to Lorenz's (1955) expressions of the APE in the atmosphere in terms of the potential temperature, which can be easily transformed into the expressions in the potential density. However sea water is a multi-component solution for which it is best to define available potential energies directly in terms of the potential density. It should be pointed out that the APE in the atmosphere includes both the potential and internal energy (Lorenz, 1955), but it represents only the potential energy in the ocean since sea water is assumed to be incompressible in the Boussinesq approximation. Also it should be mentioned that the definitions of the APE are compatible with the conservation of potential vorticity as Charney and Stern (1962) have shown in a perturbation theory of a quasi-geostrophic current.

The APE defined in eqs. (2.8) and (2.9) are positive definite and vanish only when $\tilde{\rho} = \rho' = 0$. In other words the reference state is the state of the minimum potential energy and any deviation from the reference state will cause an increase in the APE.

The anomaly of potential energy χ defined by Fofonoff (1962a) bears some consideration to make clear how close it is to the concept of the APE in comparison with the definitions in eqs. (2.8) and (2.9). Approximating $P \approx -\rho_m g z$ in eq. (1.2), where ρ_m is a mean density, it follows

$$\begin{aligned}
\chi &\approx \frac{1}{g} \int_0^P (-\rho_m g z) (\alpha - \alpha_0) \rho g dz \\
&= -\frac{\rho_m}{\rho_0} \int_z^0 (\rho_0 - \rho) g z dz \\
&\approx \int_z^0 (\rho - \rho_0) g z dz .
\end{aligned}$$

The anomaly per unit volume is $(\rho - \rho_0)gz$. It is very clear that the individual reference level, which is a key concept in the APE, is not accounted for at all in this anomaly and the density term $(\rho - \rho_0)$ does not represent a dynamically important density deviation but a simple departure from an arbitrarily chosen value ρ_0 .

III. APPLICATION OF THE AVAILABLE POTENTIAL ENERGY

In order to demonstrate the dynamical significance of the concept of the APE the definitions are applied in the MODE-I and Panulirus data. The data base is not sufficient to separate the APE into the mean and the eddy and the application is limited in the eddy APE.

III-1 Available Potential Energy in the MODE area

In applying the definitions of the APE it is most important to define the reference stratification and the slowly varying mean density field properly. This requires good density data over a very large horizontal area and the question is whether the spatial coverage of the MODE-I density data is sufficiently wide to resolve the slow variation of the mean density field $\langle \rho \rangle$. Regarding the reference stratification, the exact definition of $\{\rho_\theta\}$ cannot be kept as is, because it requires data over the entire ocean. Instead $\{\rho_\theta\}$ is substituted by a potential density field obtained by averaging 19-station data.

The streamline maps constructed by Freeland and Gould (1976) show that a single synoptic eddy observed during the MODE-I field experiment is typically as large as the size of the entire MODE area, particularly in the upper ocean. This indicates that the averaging to obtain $\langle \rho_\theta \rangle$ should be

taken over the entire MODE area if the estimate of the APE associated with MODE eddies is of interest. Keeping in mind the scales involved, let us examine what data are available. During a four-month period 708 CTD and STD stations were occupied in a circle of approximately 200 km radius centered at (28° N, 69° 40' W). According to the density program there were 37 grid points in the area of 100 km in radius, the mean spacing between stations being 33 km, and 40 grid points in the outer region, spaced every 50 km approximately. Now there are 587 station data available within 200 km in radius. Each grid point was occupied 8.3 times within 100 km in radius (except 41 stations at the central grid point) and 6.5 times in the outer region. However, the horizontal coverage becomes somewhat poorer after 176 stations are abandoned, 136 of them having no salinity or bad salinity values and no data being available for 40 stations. The problem caused by the loss of 176 stations is more serious than expected as far as the estimate of the APE is concerned. Because the MODE area was divided according to ships and most of the bad data were taken from particular ships, the loss results in very poor sampling locally and the coverage of good stations is extremely variable in time. Fortunately, it is found that at the beginning and the end of the field experiment stations were occupied regularly in space over the entire

area. Therefore it is decided the following is the best procedure in using the MODE-I density data.

(1) The mean density field $\langle \rho_\theta \rangle$ is determined by averaging 19 station data. It should be pointed out that the horizontal variation of $\langle \rho_\theta \rangle$ cannot be resolved from the available data.

(2) The eddy available potential energy A_E is calculated every 50 decibars from 300 to 2700 decibars for each station.

III-1-1 Mean density field

Tables 2a and 2b show the list of stations used for the calculation of the A_E . For convenience the two periods will be referred to as March and June, although some stations were not occupied in these months. The source data are the final form of the MODE-I density data available in computer format (Scarlet, 1974).

Because there is no information about intercomparison of data taken from different ships, a simple test is carried out to find out whether they can be mixed in the analysis. Five Chain stations and five Researcher stations in March located on the circle of 200 km in radius are picked for the test. The Chain stations were occupied about one month ahead of the Researcher stations and this separation in time should not be neglected, considering an apparent

Table 2a. List of Stations in March

<u>Ship</u>	<u>Station Number</u>	<u>Date</u>	<u>Position</u>	
Chain	C2	March 11	28° 01.9'N	69° 40.7'W
	C4	March 12	29° 00.6'N	68° 14.0'W
	C5	March 13	27° 21.2'N	68° 02.4'W
	C6	March 14	26° 26.8'N	69° 23.0'W
	C7	March 14	27° 01.7'N	71° 02.1'W
	C8	March 15	28° 33.8'N	71° 19.0'W
	C9	March 16	29° 38.7'N	69° 59.5'W
	C10	March 31	28. 39.5'N	70° 17.3'W
	C11	April 1	27° 09.0'N	69° 57.1'W
	C12	April 2	28° 19.7'N	69° 03.9'W
	C17	April 12	28° 36.2'N	69° 18.5'W
	C36	April 22	27° 59.3'N	68° 37.5'W
Discovery	D25	April 11	27° 59.1'N	70° 25.1'W
	D45	April 17	29° 21.8'N	70° 41.8'W
Researcher	R62	April 15	26° 38.9'N	68° 06.9'W
	R66	April 16	28° 16.5'N	67° 29.9'W
	R71	April 17	29° 21.9'N	69° 07.9'W
	R76	April 18	27° 41.2'N	71° 42.1'W
	R78	April 19	26° 12.0'N	70° 10.0'W

Table 2b. List of Stations in June

<u>Ship</u>	<u>Station Number</u>	<u>Date</u>	<u>Position</u>	
Chain	C136	June 26	28° 09.0'N	68° 38.5'W
	C140	June 28	27° 19.9'N	69° 02.3'W
	C141	June 29	27° 08.6'N	70° 01.3'W
	C142	July 1	29° 36.2'N	69° 58.8'W
	C143	July 1	28° 33.1'N	71° 23.0'W
	C144	July 2	26° 56.2'N	71° 04.0'W
	C148	July 4	28° 00.9'N	69° 35.7'W
Researcher	R170	June 1	27° 40.0'N	70° 47.2'W
	R173	June 2	27° 41.5'N	71° 41.4'W
	R179	June 3	28° 51.6'N	70° 03.8'W
	R190	June 6	28° 13.9'N	67° 30.3'W
	R215	June 13	29° 22.3'N	70° 42.4'W
	R218	June 14	29° 22.1'N	69° 09.0'W
	R220	June 14	28° 55.5'N	69° 06.8'W
	R223	June 15	28° 55.7'N	68° 06.5'W
	R226	June 16	27° 32.8'N	68° 07.1'W
	R228	June 16	26° 37.8'N	68° 06.9'W
	R231	June 17	26° 10.5'N	69° 40.4'W
	R233	June 18	26° 38.5'N	70° 11.1'W

westward propagation of temperature with the speed of 2.1 km/day or 2.6 km/day depending on the depth (Davis, 1975). Figure 3.1 shows the difference in the mean of the potential density, salinity, and temperature with the standard deviation of each data set.

The standard deviations of salinity and temperature from the Researcher data are approximately twice of those from the Chain data for most of the depth, indicating that the Researcher data are noisier than the Chain data. From 300 decibars to 1500 decibars both salinity and temperature from the Researcher data are lower than from the Chain data. However, these differences will not show any irregularity in the potential temperature-salinity (θ -S) space, since the discrepancies are not inconsistent with the historical θ -S curve. A t-test shows that the difference in the potential density at 300, 900, and 2100 decibars are not significant for a 95% confidence interval and the same is true for salinity and temperature. Therefore it will be assumed that there is no systematic bias in the data.

III-1-2 Eddy available potential energy in the MODE area

Figure 3.2 shows some of the vertical profiles of A_E in March. It is immediately noticed that the energy level changes very significantly in space, vertically and

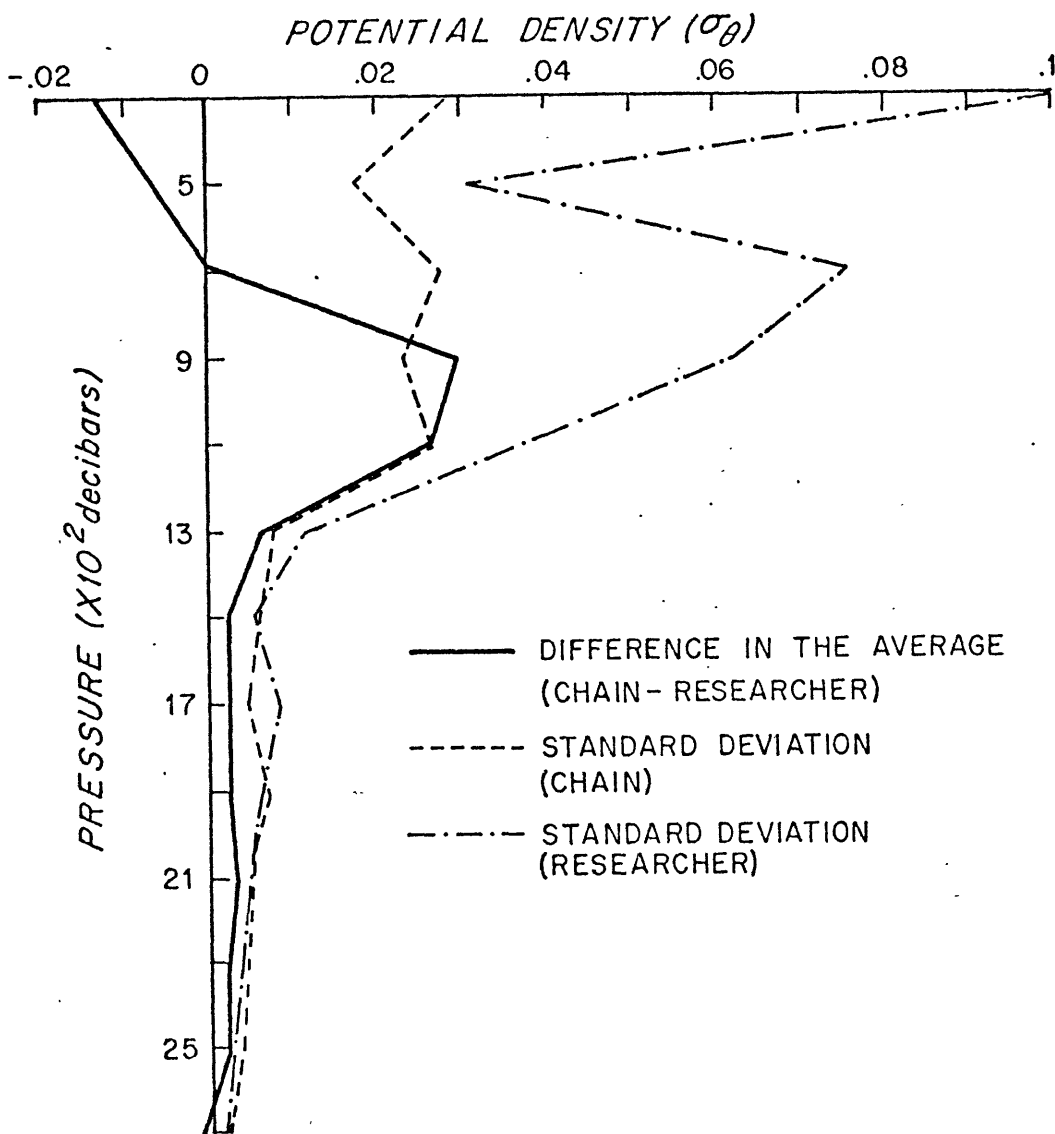


Fig. 3.1a Comparison of 5 Chain station data with 5 Researcher station data on the circle of 200 km in radius in March, 1973. Statistical test shows that the difference in the average potential density is not significant for a 95% confidence interval.

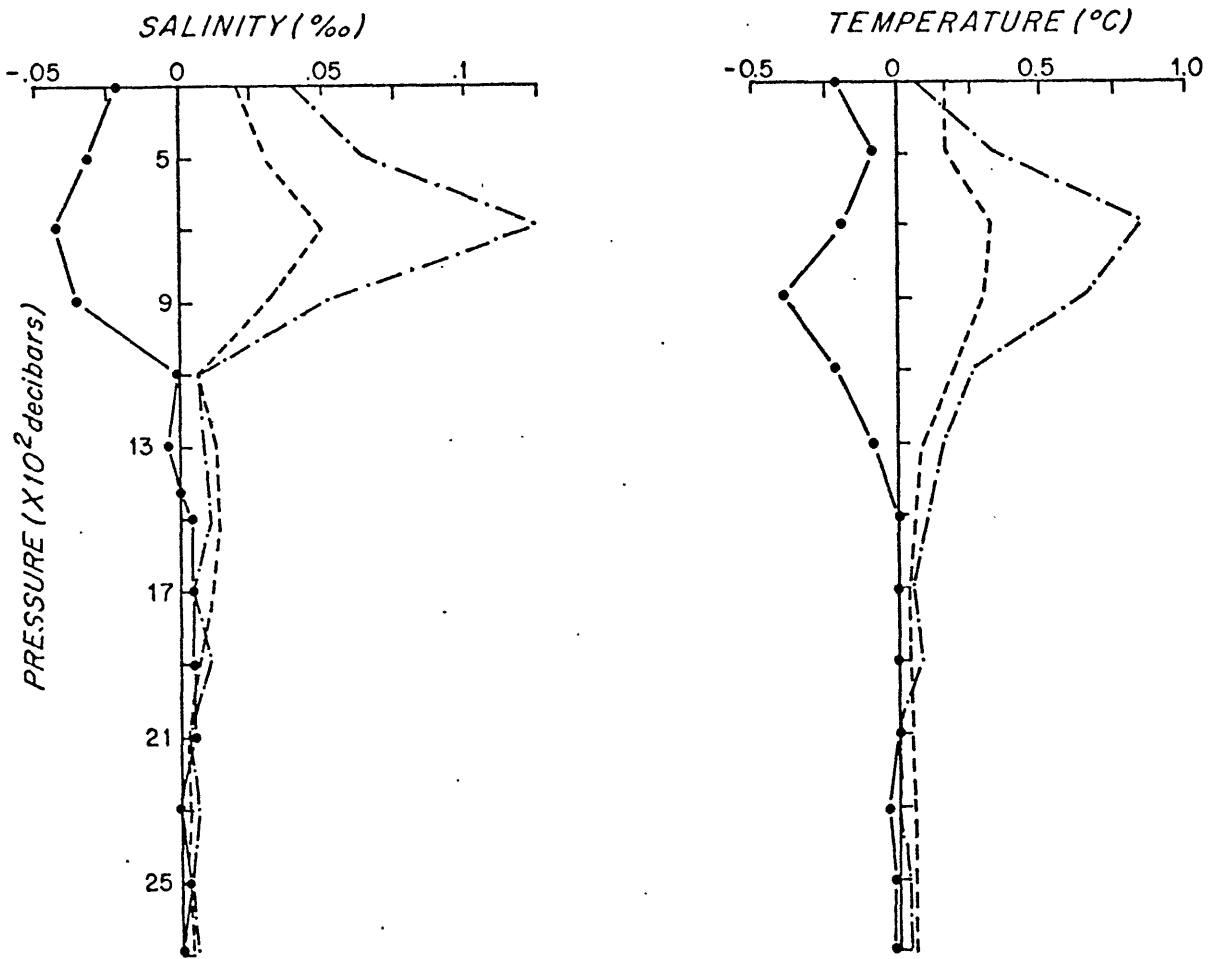


Fig. 3.1b Same as Fig. 3.1a, except that salinity and temperature are intercompared. The results of statistical tests are the same as that for the potential density.

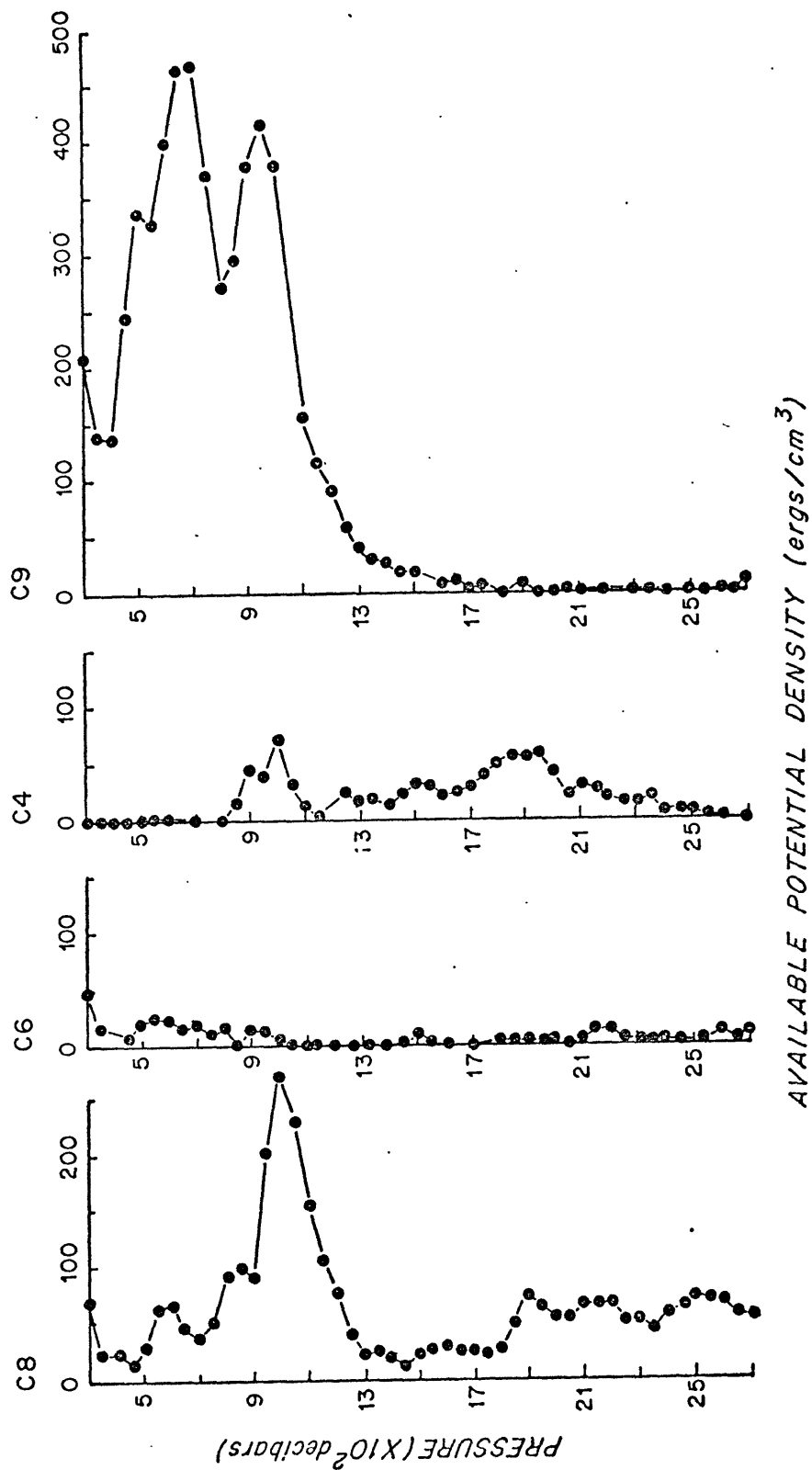


Fig. 3.2 The APE varies very significantly in space, horizontally as well as vertically.

horizontally as well. The average A_E over 19 station is shown in Fig. 3.3, whose profile resembles the profile of the gradient of the reference stratification. It is interesting to observe in Fig. 3.4 the estimate of vertical excursion corresponding to the mean A_E . The extrema in the average A_E do not appear any more and the r.m.s. excursion is rather uniform except the increase around the depth of 1500 decibars. Also Fig. 3.5 shows the horizontal distribution of the A_E for a column of water obtained by integrating the A_E over the depth of consideration.

The strong horizontal gradient in A_E implied in Fig. 3.2 and shown directly in Fig. 3.3 suggests that the process involving A_E is highly nonlinear and the advection term in eq. (2.7) may be very important in the local balance of A_E . However, once A_E is averaged, the profile is much simpler and probably interpretable. Table 3 shows the average A_E at three different depths in comparison with the average kinetic energy density estimated from Huppert and Rhines (1975, see Fig. 4.3b). Although the estimate of the average A_E is not as confident as that of the kinetic energy, it can be seen that the energies are very nearly equal within a factor of two. This is not inconsistent with the predicted properties of the geostrophic turbulence by Charney (1971). It is interesting that some features of Charney's (loc. cit) theory appear in the ocean even though the theory

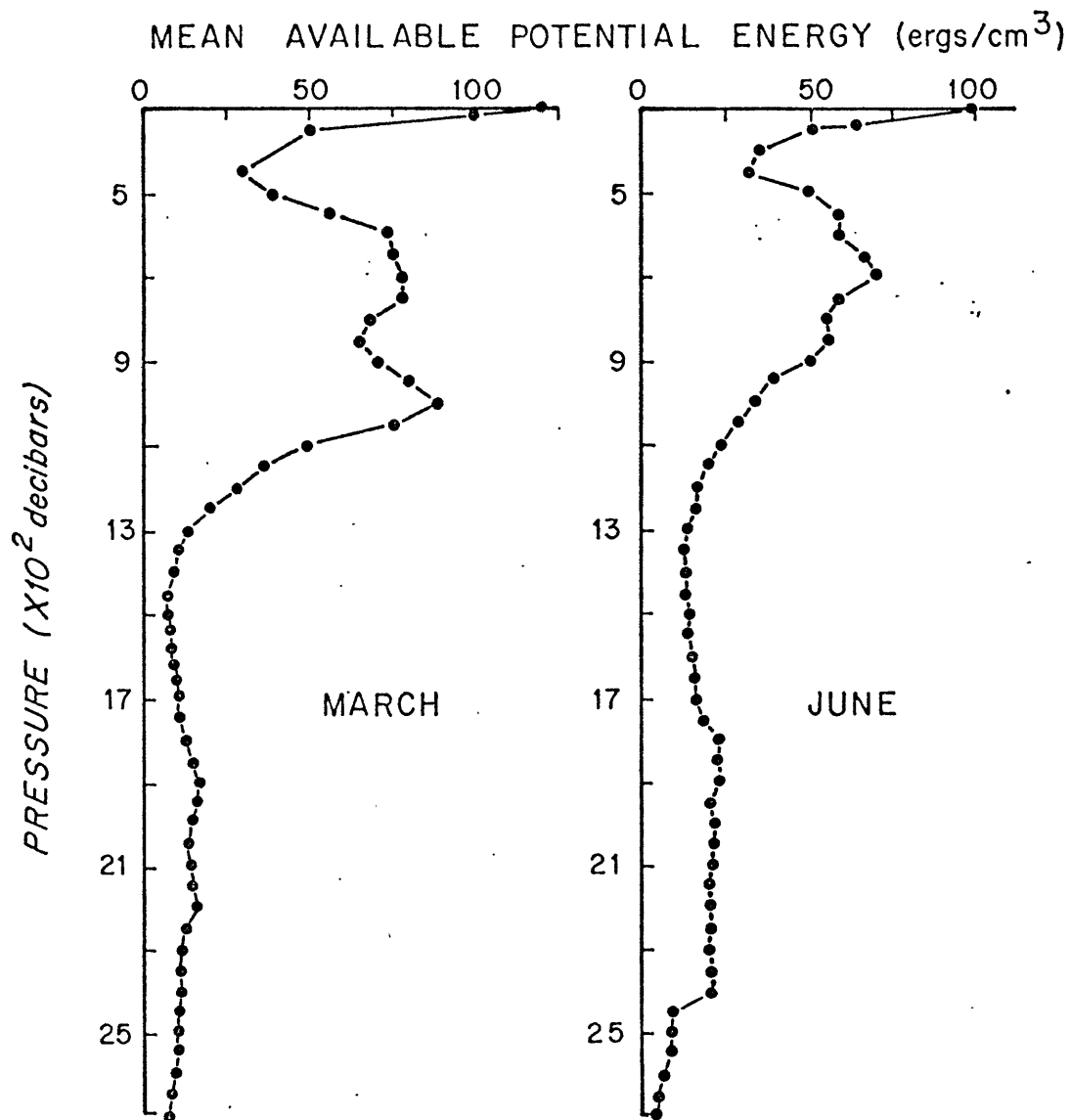


Fig. 3.3 Profile of an average APE in space from 19 stations shows remarkably simple vertical structure, which resembles the profile of vertical gradient of the reference stratification. This energy level is very similar to the average kinetic energy density at 500 m, 1500 m and 3000 m depth.

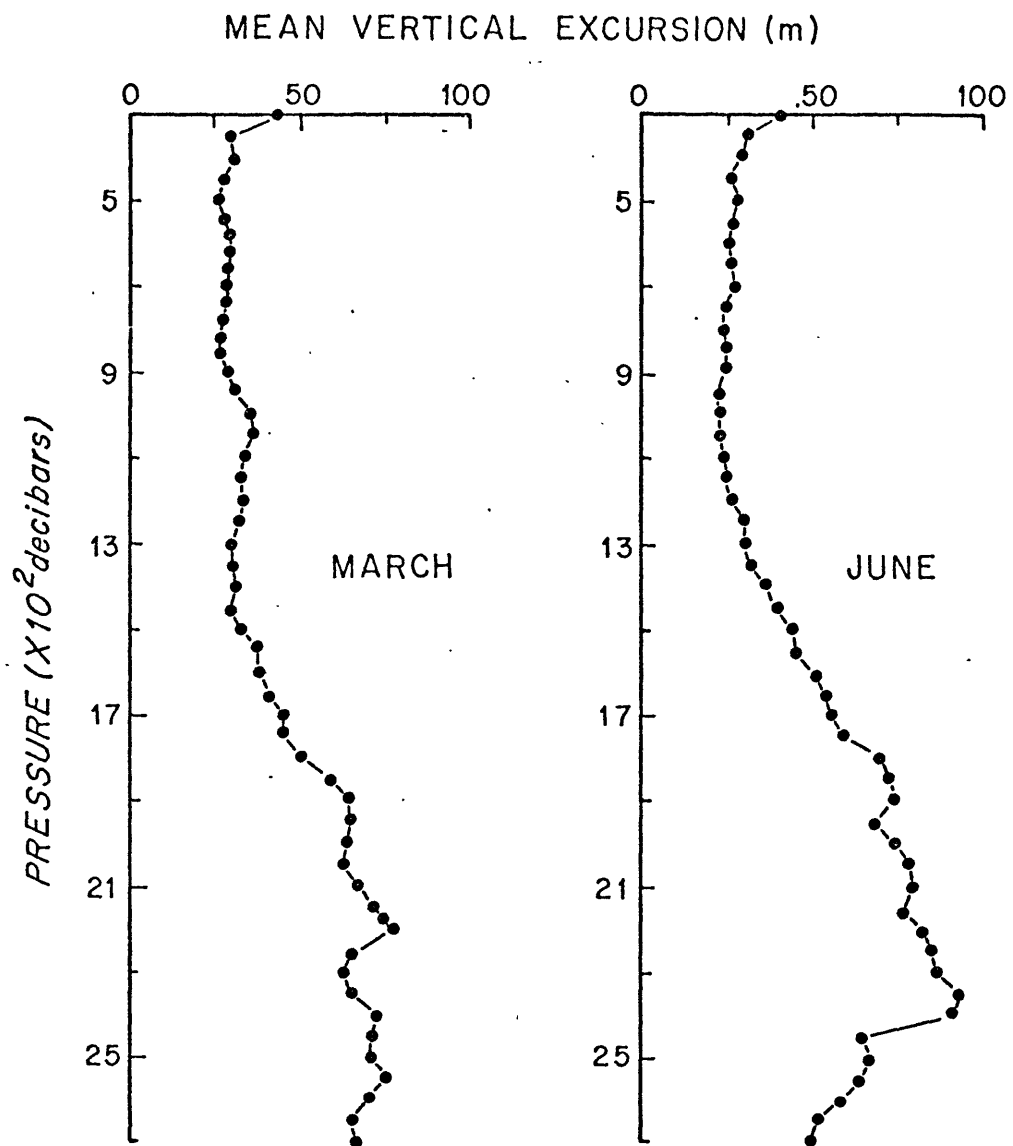
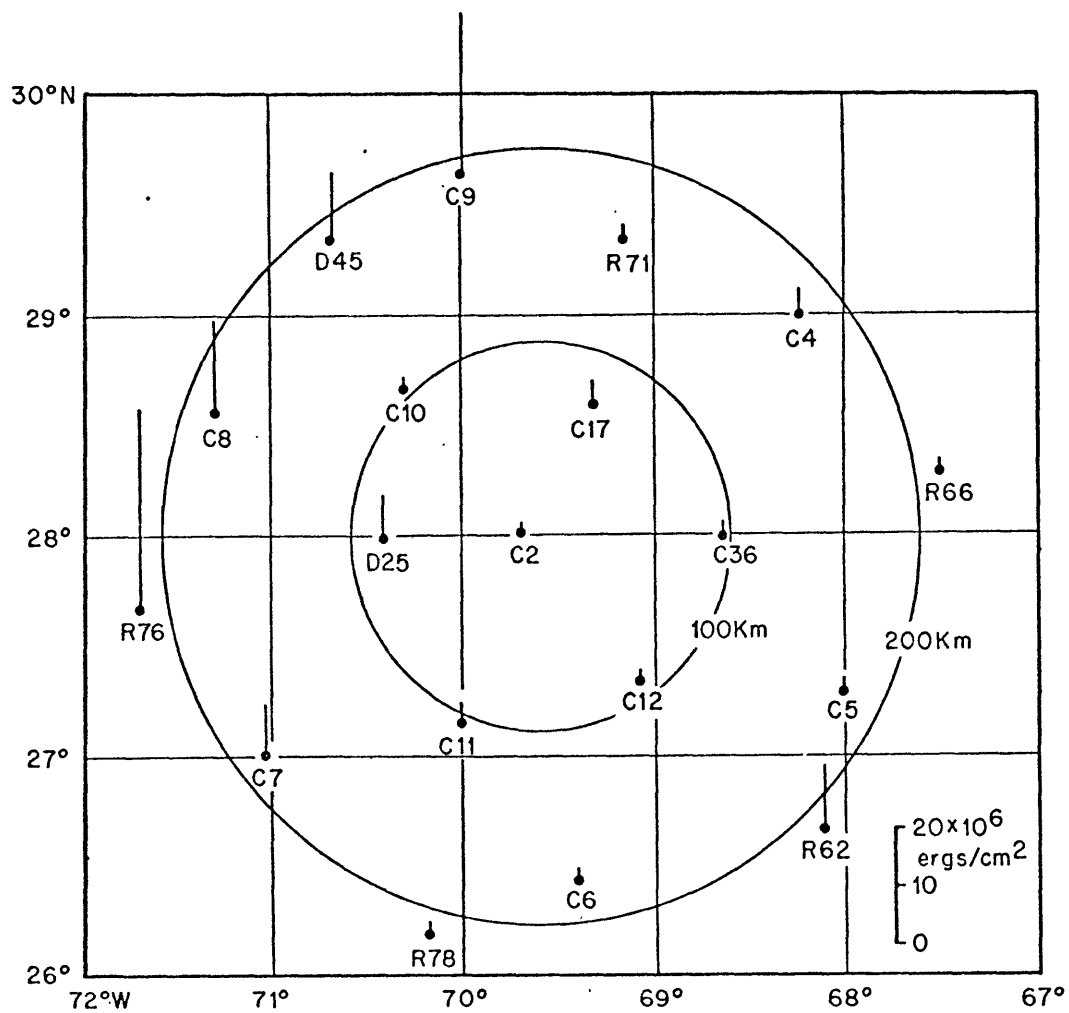
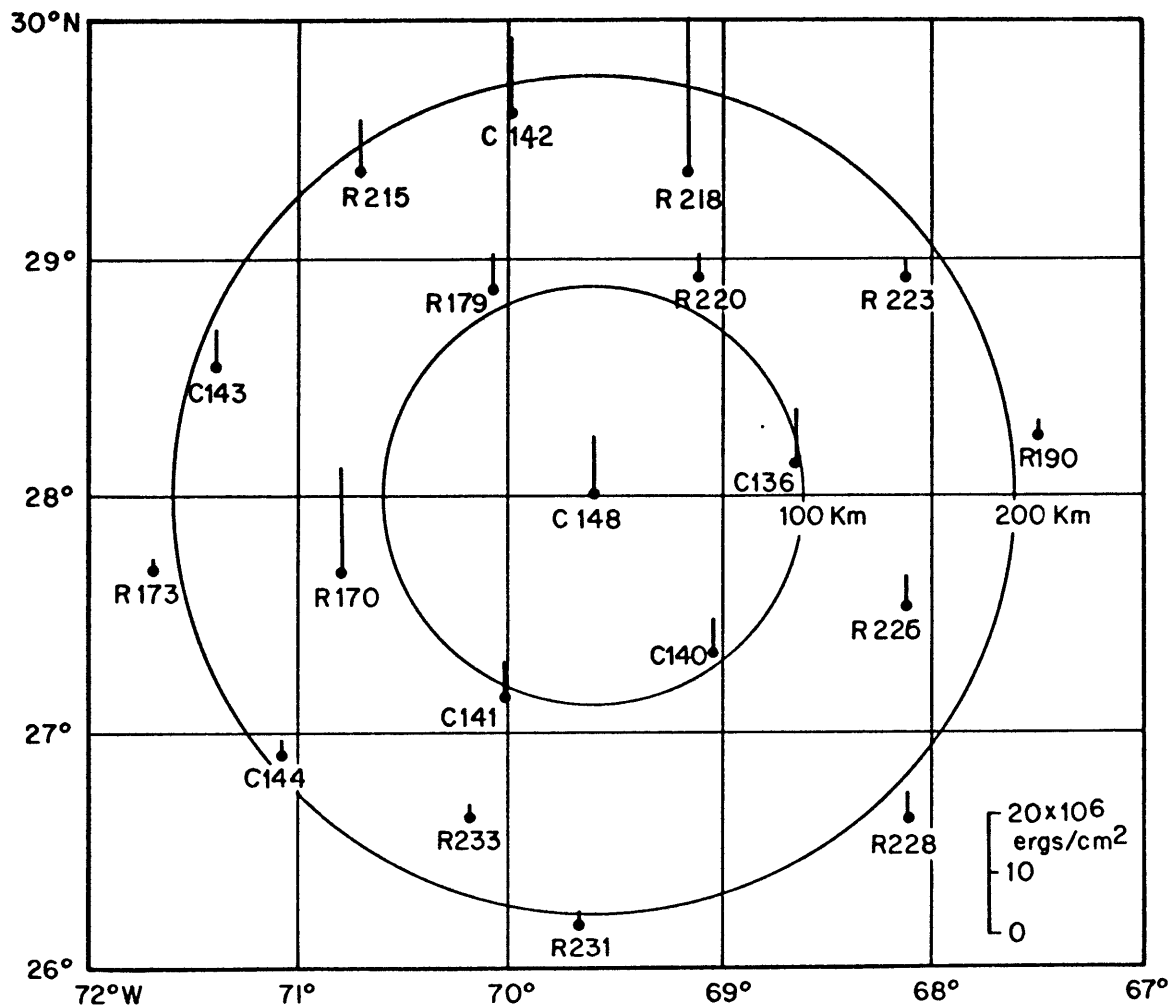


Fig. 3.4 Estimates of r.m.s. vertical excursion reveal large vertical movements below the thermocline, suggesting a strong baroclinicity, which seems to contradict the simplified picture sometimes given, that the deep water is dominated by the barotropic mode.



HORIZONTAL DISTRIBUTION OF AVAILABLE POTENTIAL ENERGY
 IN A COLUMN BETWEEN 300 AND 2700 db.
 MARCH, 1973

Fig. 3.5a Variation of the APE over a scale of 100 km suggests that an advection of the APE could be very important in a local energetics.



HORIZONTAL DISTRIBUTION OF AVAILABLE POTENTIAL ENERGY
IN A COLUMN BETWEEN 300 AND 2700 db.

JUNE, 1973

Fig. 3.5b Same as Fig. 3.5a, but in June.

Table 3. Comparison of the available potential energy(APE) with the kinetic energy(KE)** in the MODE area.

Unit: ergs/cm³

<u>Norminal Depth</u>	<u>APE</u>		<u>KE</u>
	March	June	
500 m	39.4	51.0	63.0
1500 m	8.3	14.8	7.1
2700 m	8.5	5.1	
3000 m			8.0

** Grand average of the kinetic energy density estimated from Figure 4.3b of Huppert and Rhines(1975).

was derived for small-scale turbulence which does not feel boundaries. The apparent equipartition of energies in the deep water seem to contradict the simplified picture sometimes given, that the deep water is dominated by the barotropic mode.

III-2 Available Potential Energy from the Panulirus Data

The Panulirus hydrographic stations have been occupied about 20 km southeast of Bermuda approximately twice per month since June 1954. In early stages, stations were not occupied regularly and often did not reach the deep water. Therefore only the data taken from March 8, 1960 to June 27, 1967 are analyzed here. We will adopt the second partition of the potential density given earlier, $\rho_{\theta} = \bar{\rho} + \rho^*$, based in time averaging. If the ocean were statistically homogeneous in the horizontal space, the resulting APE would be identical to the APE based on total spatial integration. But the utility of doing this in an inhomogeneous ocean is clear, because of the dominance of the energy-containing eddies at the radius of deformation.

Schroeder and Strommel (1969) showed a strong seasonal variation near the surface and a significant monthly mean variation in the steric level referred to 2000 decibars. Because an internal variation is of primary interest in this work, the apparent seasonal response is not considered

here. The monthly mean variation is taken into account in the following analysis. The water column is divided into two layers - layer I from 400 to 1160 decibars and layer II from 1160 to 2040 decibars. For a quantitative comparison potential energy is calculated in terms of χ in eq. (1.2) and A_E in eq. (2.9).

III-2-1 Anomaly of potential energy χ

Variation of χ with a period longer than a year is assumed to be negligible and χ is divided into three parts in each layer.

$$\chi = \bar{\bar{\chi}} + \bar{\chi} + \chi'$$

where $\bar{\bar{\chi}}$ is the average of χ over the entire record, which is therefore constant in time, $\bar{\chi}$ the deviation of an average when the anomalies are grouped by the month from $\bar{\bar{\chi}}$. For example $\bar{\chi}$ for January is the average of all the values of χ in January over the duration of the record minus $\bar{\bar{\chi}}$. And χ' is the deviation of χ from $(\bar{\bar{\chi}} + \bar{\chi})$. In the actual calculation of χ the computer program at the Woods Hole Oceanographic Institution is used. The average $\bar{\bar{\chi}}$ and its standard deviation is:

$$\bar{\bar{\chi}}(\text{I}) = (63.60 \pm 3.98) \times 10^8 \text{ ergs/cm}^2,$$

$$\bar{\bar{\chi}}(\text{II}) = (67.84 \pm 7.89) \times 10^8 \text{ ergs/cm}^2,$$

Where I and II in the bracket () denote the layers for which χ is calculated. Figure 3.6 shows the monthly variation of $\bar{\chi}$; a significant seasonal variation exists in layer II and the variation in layer I is obscured by a minimum in April which is a reflection of the monthly variation of mean density field. This relation is evident in the definition of χ , which is rewritten here for convenience.

$$\chi = \frac{1}{g} \int_0^P \rho \delta \, dP.$$

Pressure P is constant in time and the temporal variation of χ is due to the variation of δ or the variation of density in situ equivalently. In Fig. 3.8 in Section III-2-2 there is an indication of seasonal variation below 1151 m, but the variation between 398 and 1151 m is dominated by three peaks. It can be seen that the variation of $\bar{\chi}(I)$ is almost a mirror image of the monthly variation of the potential density at 775 m.

From a times series of χ' in Fig. 3.7, the following may be concluded:

(1) $\chi'(I)$ and $\chi'(II)$ change in phase, suggesting a strong coupling between the two layers.

(2) In part of the series a regular pattern with a period of 4-6 months exists, as can be seen in 1963-1964.

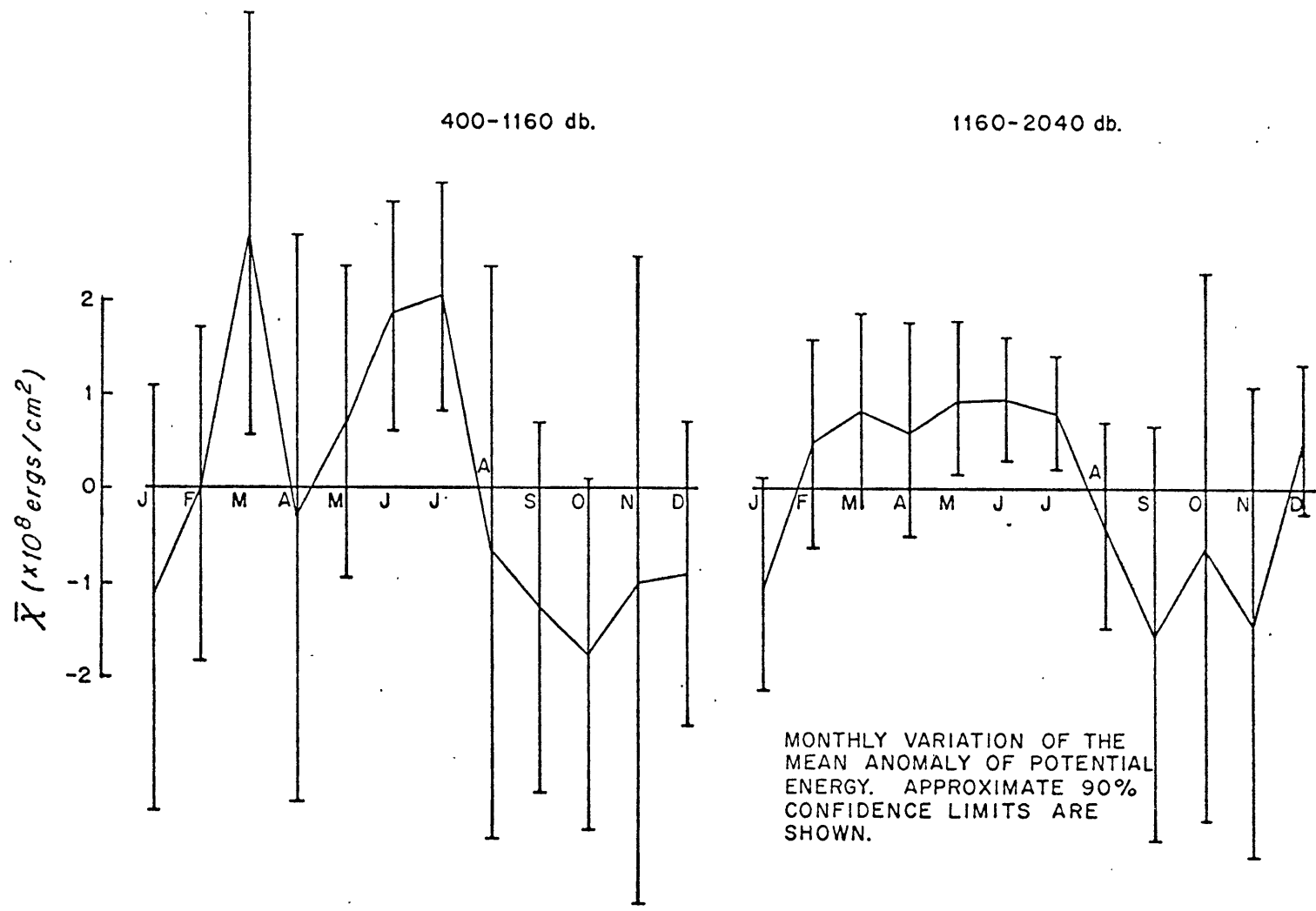
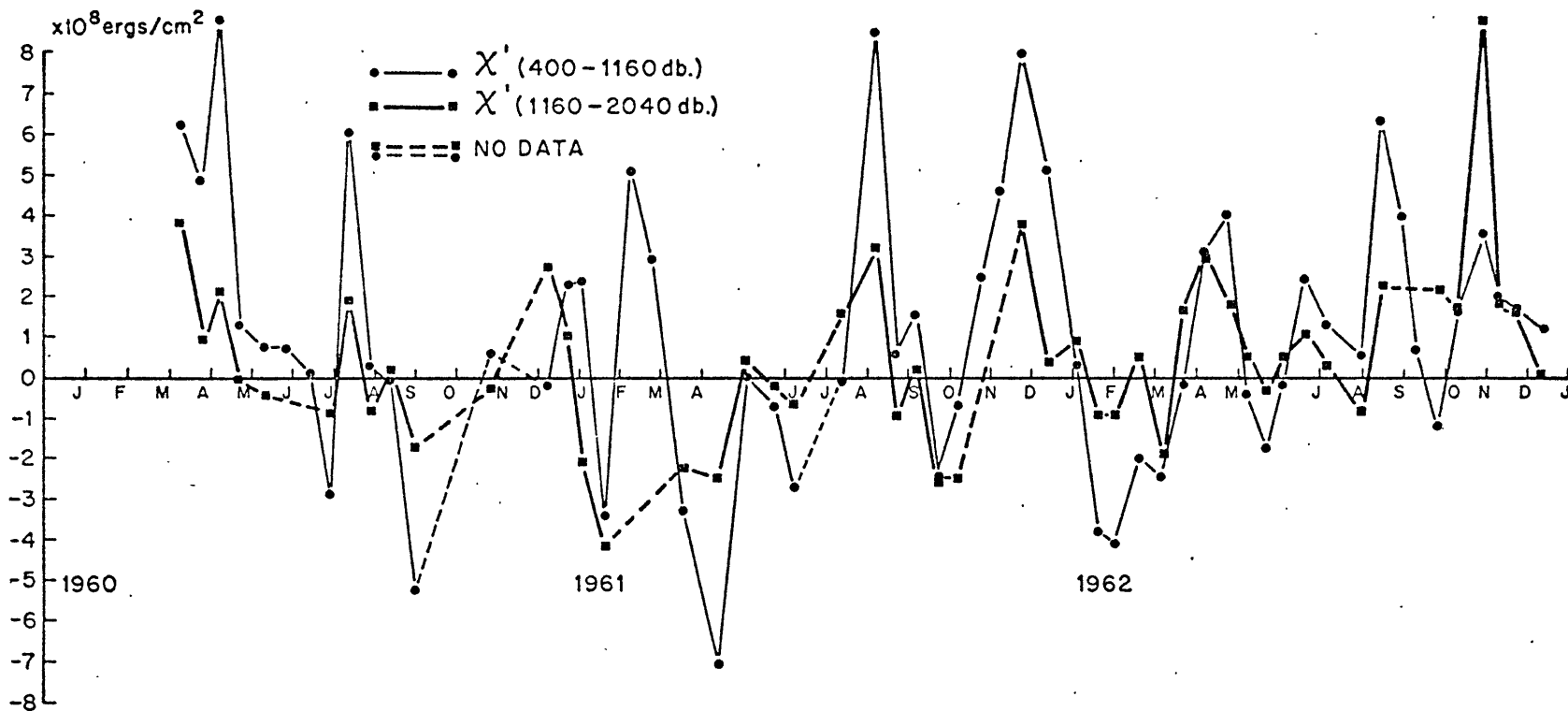
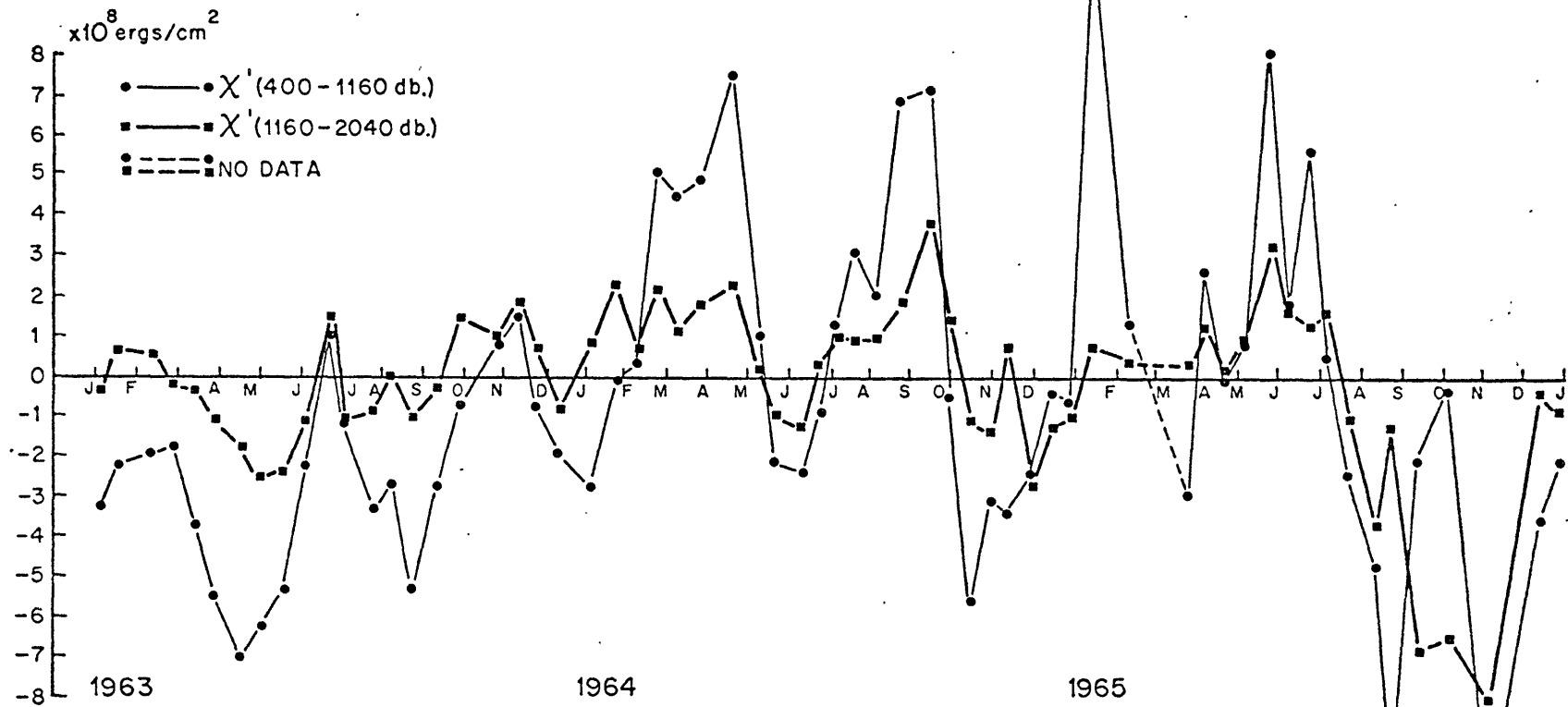


Fig. 3.6 Monthly variation of the mean anomaly of potential energy.



FLUCTUATING PART OF THE ANOMALY OF POTENTIAL ENERGY (χ')

Fig. 3.7 Time-series of fluctuating part(χ') of the anomaly of potential energy. The fluctuations are strongly coupled between the two layers. Over all the lower layer has a smaller amplitude of variation than the upper layer, yet they are of the same order of 10^8 ergs/cm^2 .



FLUCTUATING PART OF THE ANOMALY OF POTENTIAL ENERGY (X)

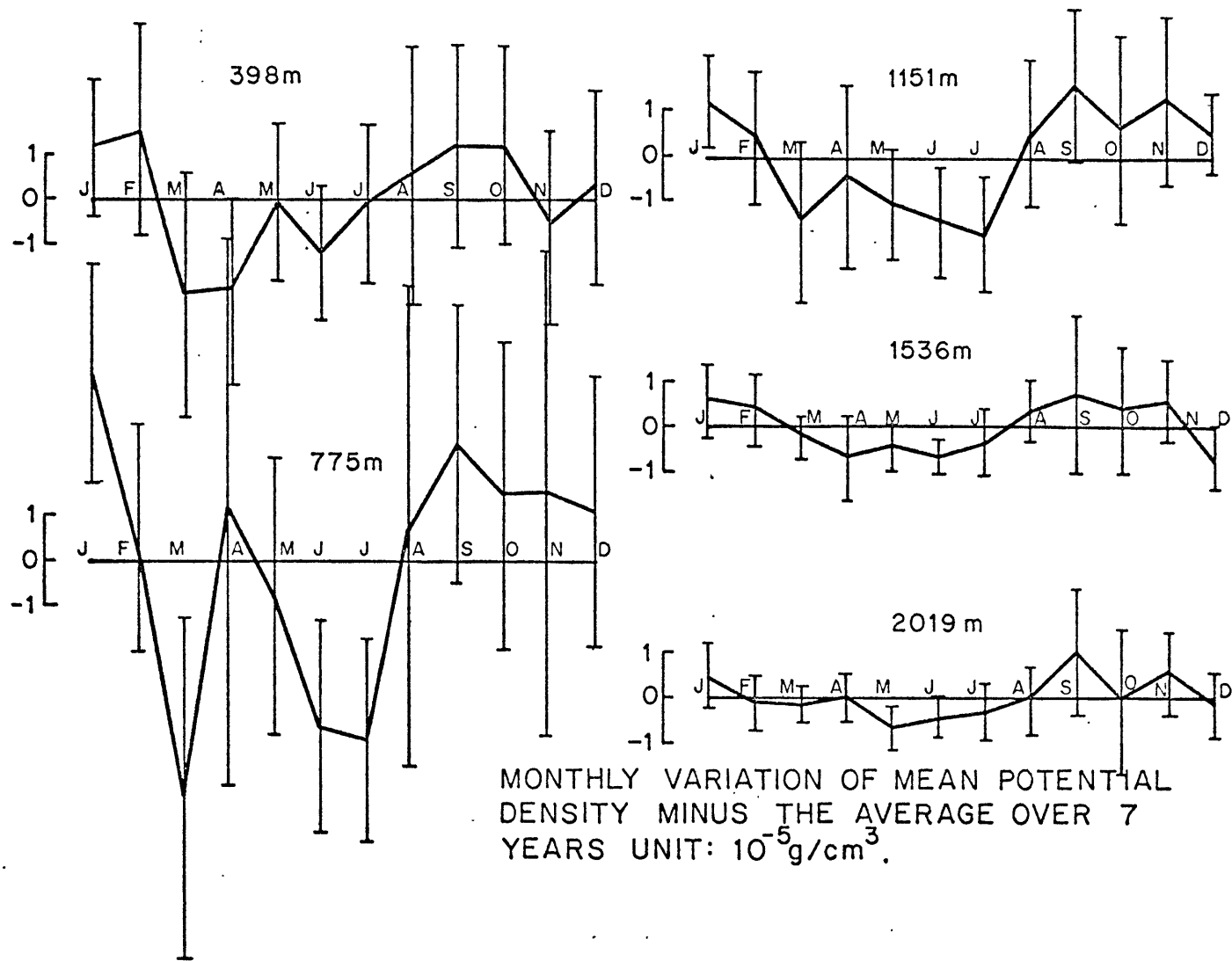


Fig. 3.8 Monthly variation of the mean potential density minus the average over 7 years.

(3) There is a significant variation in a peak-to-peak amplitude from one year to another. For example, 1962 and 1963 are relatively quiet years compared with 1964 and 1965.

(4) Over all layer II has a smaller amplitude of variation than layer I, yet they are of the same order of 10^8 ergs/cm². It should be pointed out that this magnitude is greater than the APE estimated from the MODE data by a factor of ten at least.

In both layers the fluctuating part of χ is remarkably smaller than its mean $\bar{\chi}$ by an order of magnitude.

III-2-2 Eddy available potential energy

In applying the definition of the A_E in the Panulirus data the following approximations are adopted:

(1) The reference stratification is substituted by the 7-year average potential density.

(2) The monthly variation of mean density field is taken into account by defining twelve mean potential density fields obtained by averaging the potential density after being grouped by the month. The deviation of the twelve mean fields from the 7-year average is shown in Fig. 3.8 whose variations are barely significant over the year. The idea of applying the twelve mean fields instead of the 7-year average in defining ρ' is to distinguish the eddy APE from the mean APE as far as it is possible. By definition the

two energies are separable only in space and it is assumed here that the long-term variation is associated with large-scale variation. However, this assumption should be verified from the real data in the future.

Figure 3.9 shows the time series of A_E integrated over the depth of each layer defined in the previous section. The strong tendency that the variation of A_E (I) is coupled with A_E (II) is the same as found in the time series of χ' and it is clearer in A_E because the signal has been amplified by taking the variance of ρ' .

For most of the record the level of A_E (I) is relatively higher than that of A_E (II). However, because of occasional high peaks in A_E (II), the averages of A_E (I) and A_E (II) over the entire record are about the same. In the comparison it should be remembered that layer II is deeper than layer I by 115 meters and A_E (I) and A_E (II) are the integrated value.

$$\begin{aligned} \overline{A_E(I)}^t &= 4.35 \times 10^6 \text{ ergs/cm}^2 \\ \overline{A_E(II)}^t &= 4.25 \times 10^6 \text{ ergs/cm}^2 \\ &\quad (2.9 \times 10^6 \text{ ergs/cm}^2) \end{aligned}$$

where the superscript t denotes averaging in time. The value in the parenthesis is the average when the abnormally high A_E 's in October 1962 and September, October, and November in 1965 are excluded from the averaging, because

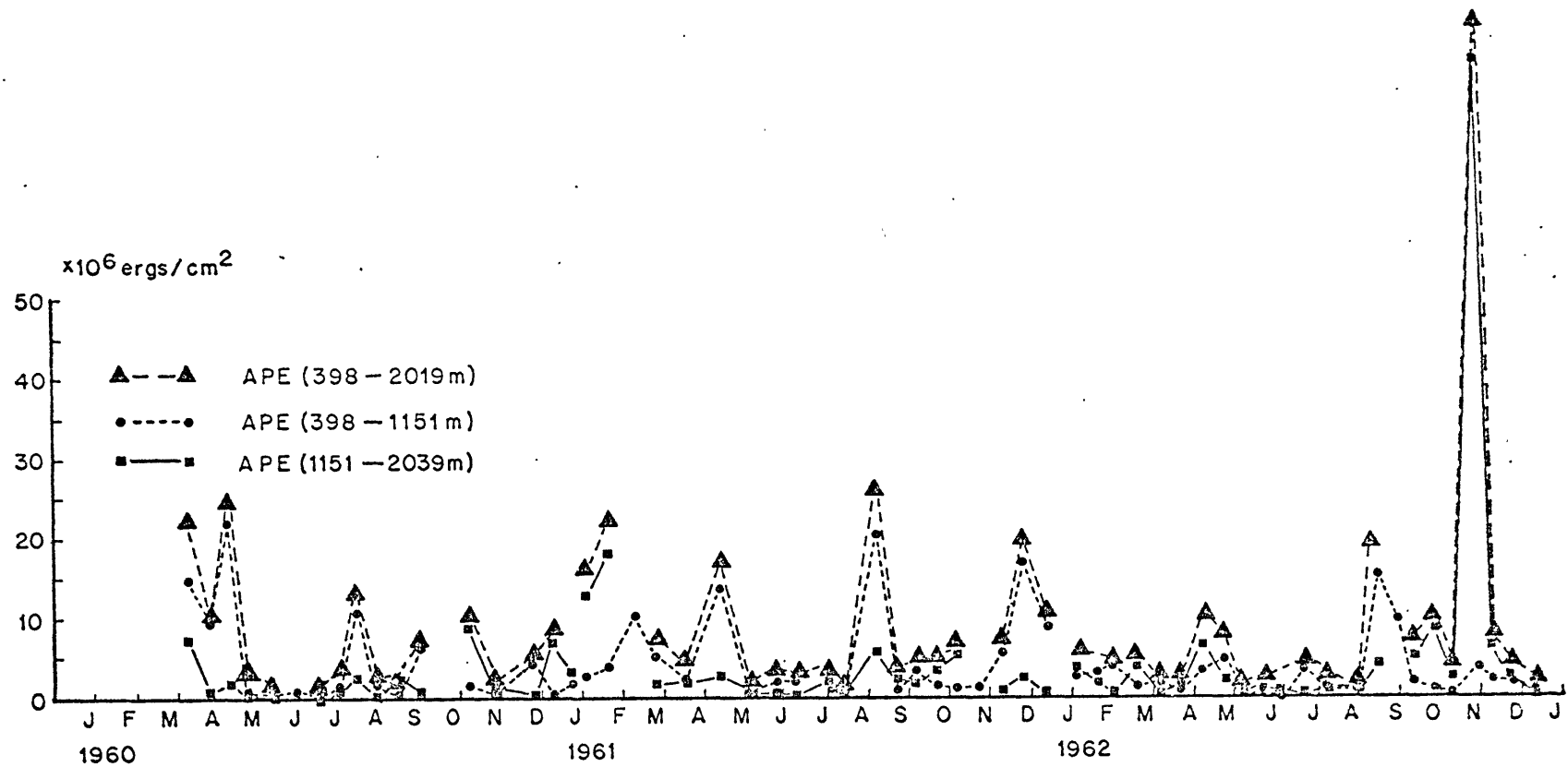
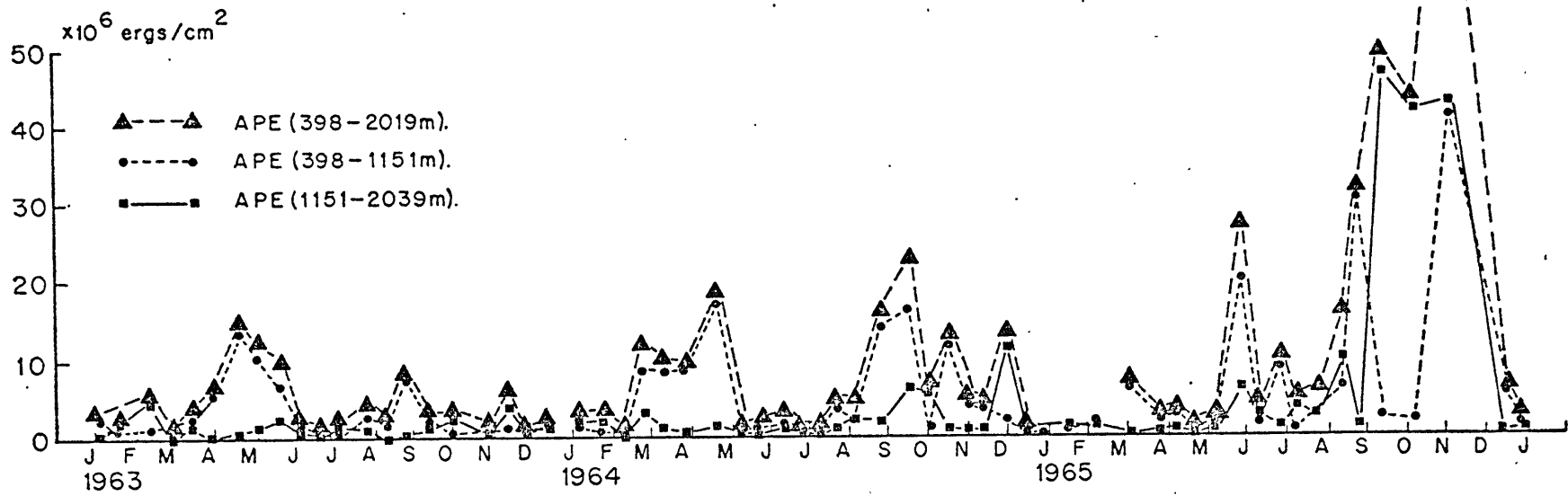


Fig. 3.9 Time-series of the APE shows again the coupling between the water in and below the thermocline. Note that a typical magnitude of the APE is smaller than that of the fluctuation in Fig. 3.7 by an order of magnitude at least.



salinity values are bad. It is very important to note the remarkable difference in their magnitudes between χ' and A_E . Instantaneously A_E is less than one-tenth of χ' in both layers as expected from the definitions themselves. It is also interesting to compare the average A_E with A_E from MODE-I averaged in space for the same depth range.

$$\text{March (MODE-I): } \overline{A_E(I)}^s = 4.89$$

$$\overline{A_E(II)}^s = 1.29$$

$$\text{June (MODE-I): } \overline{A_E(I)}^s = 3.58$$

$$\overline{A_E(II)}^s = 1.63$$

where unit is 10^6 ergs/cm² and the superscript s denotes averaging in space. The energy levels at the two locations are close to each other in the upper layer, but notably different in the lower layer. It appears that geographical location does not matter for eddies in the main thermocline, but it does in the deep water. The comparison of the reference stratifications at the two locations shows no difference in the deep water and it is possible that the difference in the energy level may be a manifestation of some island effect which has not been found before. Further discussion will be carried out later at the end of this section.

It may be worth mentioning that the eddy APE calculated with respect to the 7-year average potential density does

not show any significant departure from the previous values of A_E with the twelve mean potential densities, because ρ' in either case is much larger than the amplitude of the monthly variation of the twelve mean potential densities shown in Fig. 3.6.

In the time series of A_E it is most remarkable that a burst of high energy occurs irregularly. Figure 3.10 shows the frequency distribution of stations with respect to the total A_E integrated over the depth from 400 to 2040 decibars. The mean over the entire record is 8.6×10^6 ergs/cm² and the median is 4.8×10^6 ergs/cm², which is substantially smaller than the mean. Out of 151 stations the total A_E is less than the mean for 71% of them and higher for 29%. The oceanic state suggested by this distribution may be described by two classes of eddies, one representing most of the eddies of a relatively low energy level and the other standing above the first class with a prominent peak. Here it is implicitly assumed that the variation of A_E is due to horizontal advection of some eddy field as suggested by Wunsch (1972a).

In relation to this implied spatial variation it would be appropriate to discuss the island effect further. Wunsch (1972b) showed a steep deepening of isotherms of the main thermocline in the immediate vicinity of Bermuda where a strong jet passed the island temporarily. The 14° C

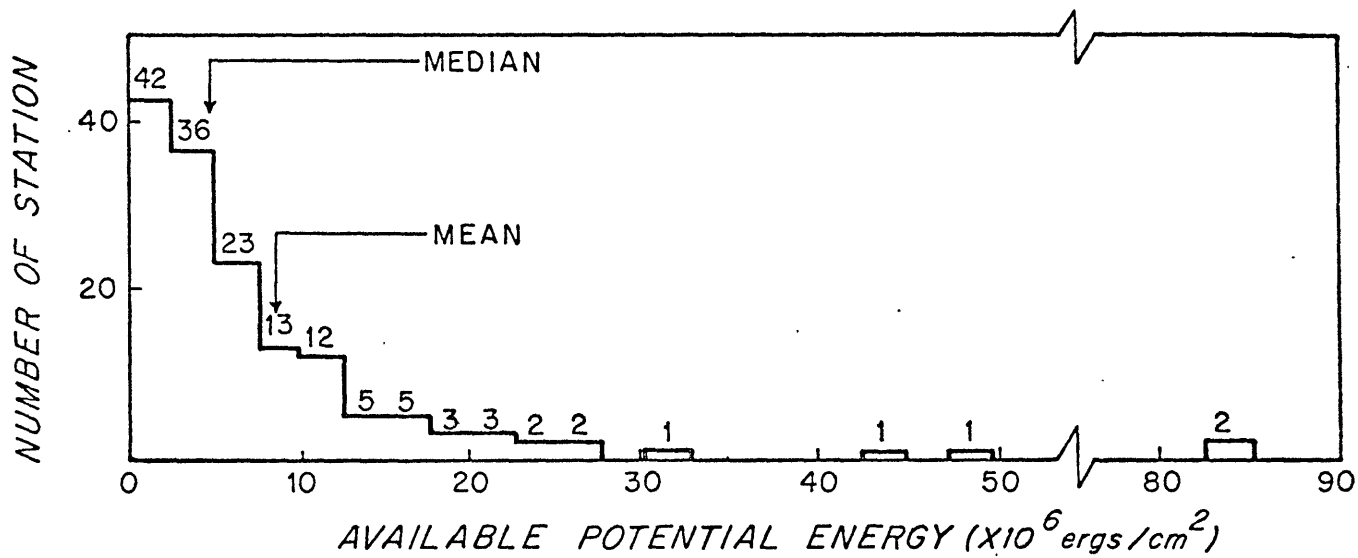


Fig. 3.10 Out of 151 stations the APE is less than the mean for 71% of them and higher for 29%. Irregular burst of high energy contributes the 29%.

isotherm goes from 525 m to 600 m in a distance of about 45 km and the 10° C isotherm changes in depth from 675 m to 800 m in the same distance at the northern side where the jet passes, but there is no significant change of isotherm depth at all at the southern side. The distance between the Panulirus station and Bermuda is about 20 km, which is approximately equal to one-half of the size of the island if the bottom contour of 100 m is considered as a measure, and a portion of the characteristic scale of an eddy in mid-ocean. Therefore it is reasonable to expect some island effect at the Panulirus station when mid-ocean eddies approach Bermuda. An estimate of peak-to-peak vertical excursion during 1964 is 190 m at the depth of 398 m, 90 m at 775 m, 130 m at 1101 m, 200 m at 1536 m and 500 m at 2019 m. The range of excursion increases both upward and downward from the center of the main thermocline. The excursion below 1151 m is larger than that at the MODE area in Fig. 3.4 by a factor of two at least. Probably it is necessary to qualify what phenomena is meant by an island effect. Hogg (1972) presented a theoretical model of a steady current interacting with an island. The eddy APE is associated with ρ' , which is a fluctuating part in the potential density after the mean $\langle \rho_\theta \rangle$ is subtracted from ρ_θ , and here the island effect refers to a large variance of ρ' , not a permanent effect in the density structure due to the presence of Bermuda.

IV. DISCUSSION AND CONCLUSIONS

Definition of the Available Potential Energy

The available potential energy (APE) in the ocean is defined in terms of the potential density. This definition is exact if sea water were single-component fluid like the air and the reference stratification were linear. In the upper 3000 m it is believed that this definition adequately represents the dynamically important part in the primitive potential energy $\rho g(Z-Z_r)$, but some modification may be necessary in the very deep water because of the thermodynamic nonlinear effect in the density as discussed by Veronis (1972). The effect of a curvature in the reference density profile is locally neglected in the definition (it can be included exactly if the APE is defined in an integral form, which is not practical), accepting an error of the order of h/H , where h is a maximum vertical excursion and H a scale height of the thermocline.

It should be mentioned that this definition is equivalent to its counterpart in the atmosphere defined in terms of the potential temperature by Lorenz (1955). Essentially the APE is equal to work done to move a fluid particle from a reference state of the minimum total potential energy in which isopycnal surface is level. Therefore the concept of the APE involves the whole system, the atmosphere of the

ocean, as pointed out by Lorenz (1955), because the reference state is conceptually reached by redistributing the whole mass of the system. However, once the reference state is defined the APE can be considered for individual fluid particles.

Recognizing the two-scale nature of the density variation in the ocean, the density is separated into the grand mean, regional, and the eddy part. It should be remarked that this separation is to isolate the APE of a certain scale process, for example MODE-I eddies, from the APE with larger scales and it is not necessarily assumed that there are only two scales in the ocean. In fact it is possible to separate the APE into three or more scales as it is done for kinetic energy in the turbulence (Mollo-Christensen, 1971).

The conversion between the mean APE and the eddy APE is a product of separating the APE into two parts, which would not appear otherwise. To compute this conversion term in the energy equations it is necessary to know not only $\tilde{\rho}$, but also its gradient which can be resolved only from data over an extended area. For example an area of 400 km in radius should be covered in order to evaluate the conversion in a circle of 200 km in radius equivalent to the size of the MODE area. There are other processes in the local balance of the APE, advection, redistribution,

and conversion to kinetic energy. Thermal forcing and topographic effect are not considered in the energy equations.

Application of the Definition

The horizontal variation of the mean potential density field $\langle \rho_\theta \rangle$ cannot be resolved from the MODE-I data because of the reason mentioned earlier. Some error is expected in the estimate of ρ' away from the center of the MODE area. The eddy APE is calculated at 19 stations and its instantaneous vertical profile shows an extremely complex structure, which varies from one station to another. It is interesting to find that the average of the 19 vertical profiles is rather simple and resembles the profile of the gradient of the reference stratification. At 500 m and 2600 m depth the average eddy APE is larger than the average kinetic energy by a factor of 1.4 and 1.2 respectively. Because the equipartition of the energies is one of the properties of the geostrophic turbulence proposed by Charney (1971) it is speculated that the dynamic characteristics of MODE eddies may not be unrelated to the geostrophic turbulence.

For 71% of the 151 stations at the Panulirus station the APE of the column of water is below its mean over the entire record. The concentrated temperature variance between 40 to 200 days in the spectrum constructed by Wunsch

(1972a) may need qualified interpretation. The behavior of the APE shows that the burst of high energy occurs intermittently, not periodically. Further statistical test is under way to verify the intermittency.

Compared with the energy level in the MODE area, the mean APE at the Panulirus station is comparable in the main thermocline and substantially large below the thermocline. The cause of this geographical difference below the thermocline is not known and it is suggested from the consideration of the scales involved that some island effect should be responsible.

In summary, the quantitative examples of the APE show that the definition of the APE is valid and very meaningful. The anomaly of potential energy χ fluctuates with an amplitude greater than the APE by an order of magnitude at least.

Density data from large-scale experiments have been used primarily in recognizing a gross pattern of eddies, but it is demonstrated that their value lies not only in a simple pattern recognition, but in understanding the dynamics and the structures of geostrophic eddies.

The vertical profile of the average eddy APE shows substantial energy level below the main thermocline in contrast with a common notion that the deep current is dominated by a barotropic mode. In fact, an r.m.s. vertical excursion below the thermocline is estimated to be larger than that in the thermocline by a factor of two approximately, indicating

again a strong baroclinicity.

The study of the APE needs further investigation. However, it is shown clearly that local energetics in the ocean cannot be budgeted properly without the APE. Therefore it is very strongly recommended that any density program in future field experiments be designed with a specific object to estimate the APE and its variation. Any good estimate of either the kinetic energy or the APE alone will be simply insufficient and the understanding of eddy dynamics can be achieved only when both energies are known simultaneously. This point seems to be too familiar to be mentioned, but it is emphasized here because the conservation of energy is so fundamental.

BIBLIOGRAPHY

- Bernstein, R. L., and W. B. White, 1974
Time and length scales of baroclinic eddies in the Central North Pacific Ocean. *J. Phys. Oceano.*, 4, 613-624.
- Bretherton, F. P., 1966
Baroclinic instability and the short wavelength cut-off in terms of potential vorticity. *Quart. J. Roy. Met. Soc.*, 12, 335-45.
- Brown, J. A., Jr., 1969
A numerical investigation of hydrodynamic instability and energy conversions in the quasi-geostrophic atmosphere: Part I and II. *J. Atmos. Sci.*, 26, 352-375.
- Bryan, K., 1963
A numerical investigation of a nonlinear model of a wind driven ocean. *J. Atmos. Sci.*, 20, 594-606.
- Bryden, H., 1975
Momentum, mass, heat, and vorticity balances from oceanic measurements of current and temperature. Ph.D. Thesis, W.H.O.I.-M.I.T. Joint Program.
- Charney, J. G., 1955
The Gulf Stream as an inertial boundary layer. *Proc. Nat. Acad. Sci., Wash.*, 41, 731-740.
- Charney, J. G. and M. E. Stern, 1962
On the stability of internal baroclinic jets in a rotating atmosphere. *J. Atmos. Sci.*, 19, 159-172.
- Charney, J. G., 1971
Geostrophic turbulence. *J. Atmos. Sci.*, 28, 1087-1095.
- Crease, J., 1962
Velocity measurements in the deep water of the Western North Atlantic. *J. Geophys. Res.*, 67, 3173-3176.
- Davis, R., 1975
"Statistical Methods". In: Dynamics and the Analysis of MODE-I Report of the MODE-I Dynamics Group. March 1975, 250 p., (unpublished manuscript). (The MODE Executive Office, 54-1417, M.I.T., Cambridge MA 02139).

- Eady, E. T., 1949
Long waves and cyclone waves. *Tellus*, 1, 33-52.
- Fofonoff, N. P., 1962a
Dynamics of Ocean Currents. *The Sea Vol. 1, Sect. III*,
edited by M. N. Hill (General Editor) Interscience
Publishers.
- Fofonoff, N. P., 1962b
Physical properties of sea-water. *The Sea Vol. 1*,
Chapt. 1, edited by M. N. Hill (General Editor),
Interscience Publishers.
- Fofonoff, N. P., 1969
Spectral characteristics of internal waves in the
ocean. *Deep-Sea Res., Supplement to Vol. 16*, 59-71.
- Freeland, H. J., P. B. Rhines and T. Rossby, 1975
Statistical observations of the trajectories of
neutrally buoyant floats in the North Atlantic.
(in preparation).
- Freeland, H. J. and W. J. Gould, 1976
Objective analysis of mesoscale ocean circulation
features.(in preparation).
- Fuglister, F. C., 1960
Atlantic Ocean atlas of temperature and salinity
profiles and data from the International Geophysical
Year of 1957-1958. Woods Hole Oceanographic
Institution, Woods Hole, Massachusetts, 209 pp.
- Garrett, C. and W. Munk, 1972
Space-time scales of internal waves. *Geophys. Fluid
Dyn.*, 2, 225-264.
- Gent, P. R., 1974
Baroclinic instability of a slowly varying zonal flow.
J. Atmos. Sci., 31, 1983-94.
- Gill, A. E., J. S. A. Green and A. J. Simmons, 1974
Energy partition in the large-scale ocean circulation
and the production of mid-ocean eddies. *Deep-Sea Res.*,
21, 499-528.
- Gill, A. E., 1974
The stability of planetary waves on an infinite Beta-
plane. *Geophys. Fluid Dyn.*, 6, 29-47.

- Gould, W. J., W. J. Schmitz, Jr. and C. Wunsch, 1974
Preliminary field results for a Mid-Ocean Dynamics
Experiment (MODE-0). *Deep-Sea Res.*, 21, 911-931.
- Hart, J. E., 1974
On the mixed stability problem for quasi-geostrophic
ocean currents. *J. Phys. Ocean.*, 4, 349-356.
- Hogg, N. G., 1972
Steady flow past an island with application to Bermuda.
Geophys. Fluid Dyn., 4, 44-81.
- Holland, W. R. and L. B. Lin, 1975
On the generation of mesoscale eddies and their con-
tribution to the ocean's general circulation. I. A
preliminary numerical experiment. (in preparation).
- Huppert, H. and P. B. Rhines, 1975
"Topographic Dynamics". In: Dynamics and the Analysis
of MODE-I Report of the MODE-I Dynamics Group. March
1975. 250 p., (unpublished manuscript). (The MODE
Executive Office, 54-1417, M.I.T., Cambridge MA 02139).
- Katz, E. J., 1973
Profile of an isopycnal surface in the main thermocline
of the Sargasso Sea. *J. Phys. Ocean.*, 3, 448-457.
- Koshlyakov, M. N. and Y. M. Grachov, 1973
Meso-scale currents at a hydrophysical polygon in the
tropical Atlantic. *Deep-Sea Res.*, 20, 507-526.
- Kuo, H-L, 1949
Dynamic instability of two-dimensional non-divergent
flow in a barotropic atmosphere. *J. Meteorol.*, 6,
105-122.
- Lin, C. C., 1955
The Theory of Hydrodynamic Stability. Cambridge
University Press.
- Longuet-Higgins, 1965a
Some dynamical aspects of ocean currents. *Quart. J.
Roy. Met. Soc.*, 91, 425-451.

- Longuet-Higgins, 1965b
The response of a stratified ocean to stationary or moving wind-systems. *Deep-Sea Res.*, 12, 927-73.
- Lorenz, E. N., 1955
Available Potential Energy and the Maintenance of the General Circulation. *Tellus*, 7, 157-167.
- Lorenz, E. N., 1972
Barotropic instability of Rossby wave motion. *J. Atmos. Sci.*, 29, 259-69.
- McCartney, M. S., 1975
Inertial Taylor columns on a beta-plane. *J. Fluid Mech.*, 68, 71-95.
- McIntyre, M. E., 1970
On the non-separable parallel flow instability problem. *J. Fluid Mech.*, 40, part 2, 273-306.
- McWilliams, J. C. and G. R. Flierl, 1975
Optimal, quasi-geostrophic wave analyses of MODE array data. (in preparation).
- Mollo-Christensen, E, 1971
Physics of turbulent flow. 1970 Von Kármán lecture. *AIAA Journal*, 9, 1217-1228.
- Newton, J. L., K. Aagaard and L. K. Coachman, 1974
Baroclinic eddies in the Arctic Ocean. *Deep-Sea Res.*, 21, 707-719.
- Oort, A. H., 1964
On estimates of the atmospheric energy cycle. *Mon. Weather Ref.*, 92, 483-493.
- Parker, C. E., 1971
Gulf Stream rings in the Sargasso Sea. *Deep-Sea Res.*, 18, 981-993.
- Pedlosky, J., 1964a
The stability of currents in the atmosphere and the ocean, I. *J. Atmos. Sci.*, 21, 201-219.
- Pedlosky, J., 1964b
The stability of currents in the atmosphere and the ocean, II. *J. Atmos. Sci.*, 21, 342-353.

- Phillips, N. A., 1966
Large-scale eddy motion in the Western Atlantic. *J Geophys. Res.*, 71, 3883-3891.
- Rhines, P. B., 1970
Edge-, bottom-, and Rossby waves in a rotating stratified fluid. *Geophys. Flu. Dyn.*, 1, 273-302.
- Rhines, P. B., 1971
A comment on the Aries observations. *Phil Trans. Roy. Soc., A.*, 270, 461-463.
- Rhines, P. B., 1973
Observations of the energy-containing oceanic eddies, and theoretical models of waves and turbulence. *Boundary-Layer Met.*, 4, 345-60.
- Rhines, P. B., 1975a
The dynamics of unsteady currents. *The Sea*, Vol. VI, ed. by J. J. O'Brien. (submitted).
- Rhines, P. B., 1975b
Waves and turbulence on a beta-plane. *J. Fluid Mech.* (in press).
- Robinson, A. R. and J. C. McWilliams, 1974
The baroclinic instability of the open ocean. *J. Phys. Oceano.*, 4, 281-294.
- Sanford, T. B., 1975
Observations of the vertical structure of internal waves. (in press)
- Scarlet, R., 1974
"MODE-I Density Profiles". In: Instrument Description and Intercomparison Report of the MODE-I Intercomparison Group. December, 1974, 173 p., (unpublished manuscript). (The MODE Executive Office, 54-1417, M.I.T., Cambridge MA 02139).
- Schroeder, E. and H. Stommel, 1969
How representative is the series of PANULIRUS stations of monthly mean conditions off Bermuda? *Progress in Oceanogr.*, 5, 31-40
- Schulman, E. E., 1967
The baroclinic instability of a mid-ocean circulation. *Tellus*, 19, 292-305.

- Simmons, A. J., 1974
The meridional scale of baroclinic waves. J. Atmos. Sci., 31, 1515-1525.
- Song, R. T., 1971
A numerical study of the three-dimensional structure and energetics of unstable disturbances in zonal currents: Part I & II. J. Atmos. Sci., 28, 549-586.
- Stommel, H., 1966
The Gulf Stream 2nd Ed., University of California Press.
- Stone, P. H., 1969
The meridional structure of baroclinic waves. J. Atmos. Sci., 26, 376-389.
- Sverdrup, H. U., 1947
Wind-driven currents in a baroclinic ocean; with application to the equatorial currents of the Eastern Pacific. Proc. Nat. Acad. Sci., Washington, DC, 33, 318-326.
- Swallow, J. C., 1971
The Aries current measurements in the Western North Atlantic. Phil Trans. Roy. Soc., A., 270, 451-460.
- Veronis, G., 1972
On properties of seawater defined by temperature, salinity and pressure. J. Mar. Res., 30, 227-255.
- Veronis, G., 1973
Large scale ocean circulation. Advances in Appl. Mech., 13, 1-92.
- Veronis, G., and H. Stommel, 1956
The action of variable wind stresses on a stratified ocean. J. Mar. Res., 15, 43-45.
- Whittaker, E. T. and G. N. Watson, 1927
A course of modern analysis. Cambridge University Press.
- Wunsch, C., 1972a
The spectrum from two years to two minutes of temperature fluctuations in the main thermocline at Bermuda. Deep-Sea Res., 19, 577-593.
- Wunsch, C., 1972b
Temperature microstructure on the Bermuda slope with application to the mean flow. Tellus, 24, 350-367.

BIOGRAPHY

The author was born in Seoul, Korea on February 17, 1946 and married SooJung Yoon at M.I.T. Chapel on August 28, 1971. He received the degrees of S.B. and M.S. in physics, and was admitted in the Joint Program in Oceanography September, 1970.

Publication:

Kim, K., C. O. Lee and C. S. Kim(1970)
Electrohydrodynamic bulk instability of a slightly
conducting fluid between two coaxial cylinders with
a small temperature. J. Phys. Soc. Japan, 29, 1625-34.